1.0

1.1

1.25

4.5
5.0
5.6

2.8
3.2
3.6
4.0

2.5

2.2

2.0

1.8

1.4   1.6

MICROCOPY RESOLUTION TEST CHART
NATIONAL BUREAU OF STANDARDS-1963-A

LEVEL II

5 OCT RECD

AAE

AERONAUTICAL
AND ASTRONAUTICAL
ENGINEERING DEPARTMENT

D D C
RECEIVED
DEC 13 1979
D

ENGINEERING EXPERIMENT STATION, COLLEGE OF ENGINEERING, UNIVERSITY OF ILLINOIS, URBANA

79 12 10 033

LEVEL II

(12)

Aeronautical and Astronautical Engineering Department

University of Illinois at Urbana-Champaign

Urbana, Illinois

Technical Report AAE TR 79-5

UILU Eng 79-0505

AN EFFICIENT ROTATIONAL NONEQUILIBRIUM

MODEL OF A CW CHEMICAL LASER

Lee H. Sentman
University of Illinois

·   and

Warren Brandkamp
Bell Aerospace Textron

Prepared for

Air Force Office of Scientific Research
Bolling AFB, D.C. 20332

July 1979

Final Report AFOSR Grant 78-3669

DDC

RECEIVED
DEC 13 1979
D

176 005

JOB

REPORT DOCUMENTATION PAGE		READ INSTRUCTIONS BEFORE COMPLETING FORM
1. REPORT NUMBER AFOSR-TR- 79-1234	2. GOVT ACCESSION NO.	3. RECIPIENT'S CATALOG NUMBER
4. TITLE (and Subtitle) AN EFFICIENT ROTATIONAL NONEQUILIBRIUM MODEL OF A CW CHEMICAL LASER.		5. TYPE OF REPORT & PERIOD COVERED FINAL REPORT 15 May 1978-14 May 1979
		6. PERFORMING ORG. REPORT NUMBER
7. AUTHOR(s) Lee H. Sentman Warren Brandkamp		8. CONTRACT OR GRANT NUMBER(s) AFOSR-78-3669
9. PERFORMING ORGANIZATION NAME AND ADDRESS Aeronautical and Astronautical Eng. Dept. University of Illinois at Urbana-Champaign Urbana, IL 61801		10. PROGRAM ELEMENT, PROJECT, TASK AREA & WORK UNIT NUMBERS 61102F 2303/B1 B1
11. CONTROLLING OFFICE NAME AND ADDRESS AFOSR NC Bolling AFB, D.C. 20332		12. REPORT DATE July 1979
		13. NUMBER OF PAGES 110
14. MONITORING AGENCY NAME & ADDRESS(if different from Controlling Office) AAE-TR-79-5, UILU-ENG-79-0505		15. SECURITY CLASS. (of this report) UNCLASSIFIED
		15a. DECLASSIFICATION/DOWNGRADING SCHEDULE

16. DISTRIBUTION STATEMENT (of this Report)

Approved for public release;
distribution unlimited.

17. DISTRIBUTION STATEMENT (of the abstract entered in Block 20, if different from Report)

18. SUPPLEMENTARY NOTES

19. KEY WORDS (Continue on reverse side if necessary and identify by block number)

Chemical laser
Rotational Nonequilibrium
Power spectral distribution
Kinetics - Physical Optics

20. ABSTRACT (Continue on reverse side if necessary and identify by block number)

An efficient rotational nonequilibrium model of a cw chemical laser was developed. The essential elements of the model and their influence on laser performance were shown by detailed comparison with a model which contains boundary layer flow striations, F atom wall recombination and detailed, finite rate kinetics (typically 21 species and 143 reactions). Rotational equilibrium and nonequilibrium species profiles, saturated gains, intensity distributions and power spectral distributions were compared for several cases. The

DD FORM 1473
1 JAN 73

176 005

ACKNOWLEDGMENT

TABLE OF CONTENTS

I. INTRODUCTION

This study is concerned with understanding the nonlinear coupling which occurs between the fluid dynamics, kinetics and the optical resonator of a cw chemical laser. The motivation for this work is the necessity of predicting the power and power spectral performance of the laser. The significant effects of rotational nonequilibrium on the performance of chemical lasers have been described in the HF cw case by Sentman[1] and in the pulsed case by Hough and Kerber[2]. The DF cw case has been treated by Hall[3] and the HF single line amplifier by Skifstad[4]. The agreement between these calculations and the experimental data showed that, when rotational nonequilibrium is included in the model, several J transitions within a given vibrational band lase simultaneously, most of the power is contained in those J transitions which are preferentially populated by the pumping reaction, and the power is decreased by 20-30% from the rotational equilibrium value. All of these studies employed a Fabry-Perot model for the optical cavity, whereas practical lasers usually extract power with an unstable resonator. The effect of the optical model on cw laser performance was examined by Sentman[5]. Calculations were performed for both rotational equilibrium and nonequilibrium cases for a confocal unstable resonator with 50% geometric outcoupling. For the rotational equilibrium case, the solution resulted in most of the power being contained in one line. For the rotational nonequilibrium case, the power is distributed over eleven lines, and the Fabry-Perot and unstable resonator power spectral distributions are almost identical, the major difference being that all lines whose saturated gain region does not extend into the central portion of the unstable resonator are cut off. For the rotational nonequilibrium case, fluctuations in cw power were shown to occur on lines whose saturated gain zone does not fill the unstable resonator. The

amplitude of the fluctuation was determined by the fraction of the resonator filled by the saturated gain zone of the oscillating line, and the frequency of the fluctuation was determined by the location of the intensity peak of the oscillating line.

These studies have demonstrated that:

1. Rotational nonequilibrium plays a major role in determining the power spectral performance of the laser. This phenomenon must be included in any model, Fabry-Perot or unstable resonator, which is to predict the power spectral performance of the laser.

2. Rotational equilibrium models over predict the total power and maximum intensity.

3. For rotational nonequilibrium, the Fabry-Perot and unstable resonator power spectral distributions are identical.

4. Rotational nonequilibrium is the mechanism responsible for a non-linear coupling which may occur between the saturated gain and the resonator geometry resulting in large amplitude fluctuations on a given line.

Since the computation time for a computer model of a chemical laser depends upon N^2, where N is the number of dependent variables, the necessity of including rotational nonequilibrium in the model will result in a significant increase in run time because the number of dependent variables will increase from about 30 to 80 or more. Since most of the preceding studies were carried out using very simplified kinetic, fluid dynamic models, these results are qualitative rather than quantitative. Thus, the main thrust of the present work was to modify the qualitative, but computationally efficient, rotational nonequilibrium cw chemical laser model developed by Sentman[1,5] so that it would give quantitative predictions of the power spectral performance of the laser.

Since coupled kinetic-physical optics calculations are iterative in nature and computationally expensive (~ 300 sec/iteration on the CYBER 175 with Sentman's model[5] with convergence occurring in about 15 iterations), a two pronged approach was employed. First, the modification of the kinetic-fluid dynamic model was carried out using a Fabry-Perot model[1] for the resonator (a typical case with Sentman's model[1] takes 30 sec on the CYBER 175). Simultaneously, a physical optics model supplied by AFWL was coupled to Sentman's rotational nonequilibrium model[1] and several of the previous cases run to verify those results. The AFWL optics model was then coupled to the new kinetics-fluid dynamic model which has been developed. In Section II, the kinetic-fluid dynamic model which has evolved is described; the comparison with the results from a sophisticated chemical laser model, the Bell Aerospace Textron Blaze II model[6], for two different cases is given in Section III. In Section IV, the comparison of the AFWL physical optics model with the original physical optics model[5] are presented and the status of the coupled AFWL physical optics and the new kinetics is described. Several conclusions and recommendations for future studies are discussed in Section V.

II. KINETICS-FLUID DYNAMICS MODEL

The main thrust of this work was to modify the qualitative, but com-
putationally efficient, rotational nonequilibrium cw chemical laser model
developed by Sentman[1,5] so that it would give quantitative predictions of
the power spectral performance of the laser. For computational efficiency,
the number of dependent variables must be kept to a minimum. Based on ex-
perience with that model, the approach used in this study was to include
the essential chemical kinetics - the pumping reactions, major deactivation
reactions and rotational relaxation reactions -, and to include the fluid
dynamic effects of mixing by inputing the pressure, temperature, velocity,
mass flow rate remaining in the primary, mass flow rate remaining in the
secondary and the length of the active media as functions of x which are ob-
tained from one of the available quasi-2D, 2D or 3D fluid dynamic, rota-
tional equilibrium, chemical kinetic laser models[6,7,8]. This approach was
motivated by the fact that changes in chemical kinetics, which significantly
affect the power spectral performance, in most cases, have only a minor
effect on the flow field in which the kinetics takes place. Thus, the fluid
dynamics provides the environment in which the kinetics occurs.

Since this model will reproduce the rotational equilibrium results when
it is run using a value of the rotational relaxation rate constant which is
10^5 times its measured value, the model has evolved from detailed compari-
sons with the Blaze II model[6] for two different cases: an Aerospace arc
driven HF power spectral experiment[9] and the Bell Aerospace Textron CL XI
(15,30) lasing lines experiment. These two cases were chosen because, in
addition to providing power spectral data, and in the CL XI case, intensity
distributions on each line, they represent two extremes of fluid dynamic
mixing; the Aerospace case is a slow mixer whereas the CL XI is a relatively
fast mixing nozzle. This should ensure that the polynomial fits used for

the fluid variables should be capable of handling any profiles likely to be encountered.

2.1 THE RADIATION FIELD

For purposes of developing the kinetic-fluid dynamic model, the optical cavity was modeled as a Fabry-Perot resonator. The physical optics model for an unstable resonator is described in Chapter IV.

When rotational nonequilibrium is included in the model, several J transitions within each vibrational band lase simultaneously with the dominant ones being determined by the J dependence of the pumping reaction, Ref. 1. Because of this, the treatment of rotational nonequilibrium effects is facilitated by using a more exact treatment of the radiation field than that afforded by the constant gain approximation. The description of the radiation field employed is that developed by Sentman, Ref. 1 and summarized below.

The geometry is shown in Fig. 1, where plane parallel mirrors form a Fabry-Perot cavity. The gas between the active medium and the mirrors is assumed to be nonabsorbing and hence the mirror boundary conditions can be applied at $Z = 0$ and L. The radiative transfer equations are

$$\frac{dI_\nu^+}{dZ} = \alpha_\nu(I_\nu^+ + S_\nu) \qquad (2.1\text{-}1)$$

$$\frac{dI_\nu^-}{dZ} = -\alpha_\nu(I_\nu^- + S_\nu) \qquad (2.1\text{-}2)$$

where α_ν is the gain coefficient and S_ν is the spontaneous emission term given by

$$S_\nu = 2h^2\nu^4 N_A \rho B_{LU} n_U \eta_{UL} g_L / c^2 g_U \alpha_\nu \qquad (2.1\text{-}3)$$

n_U and n_L are the number of moles in the upper and lower states per gram
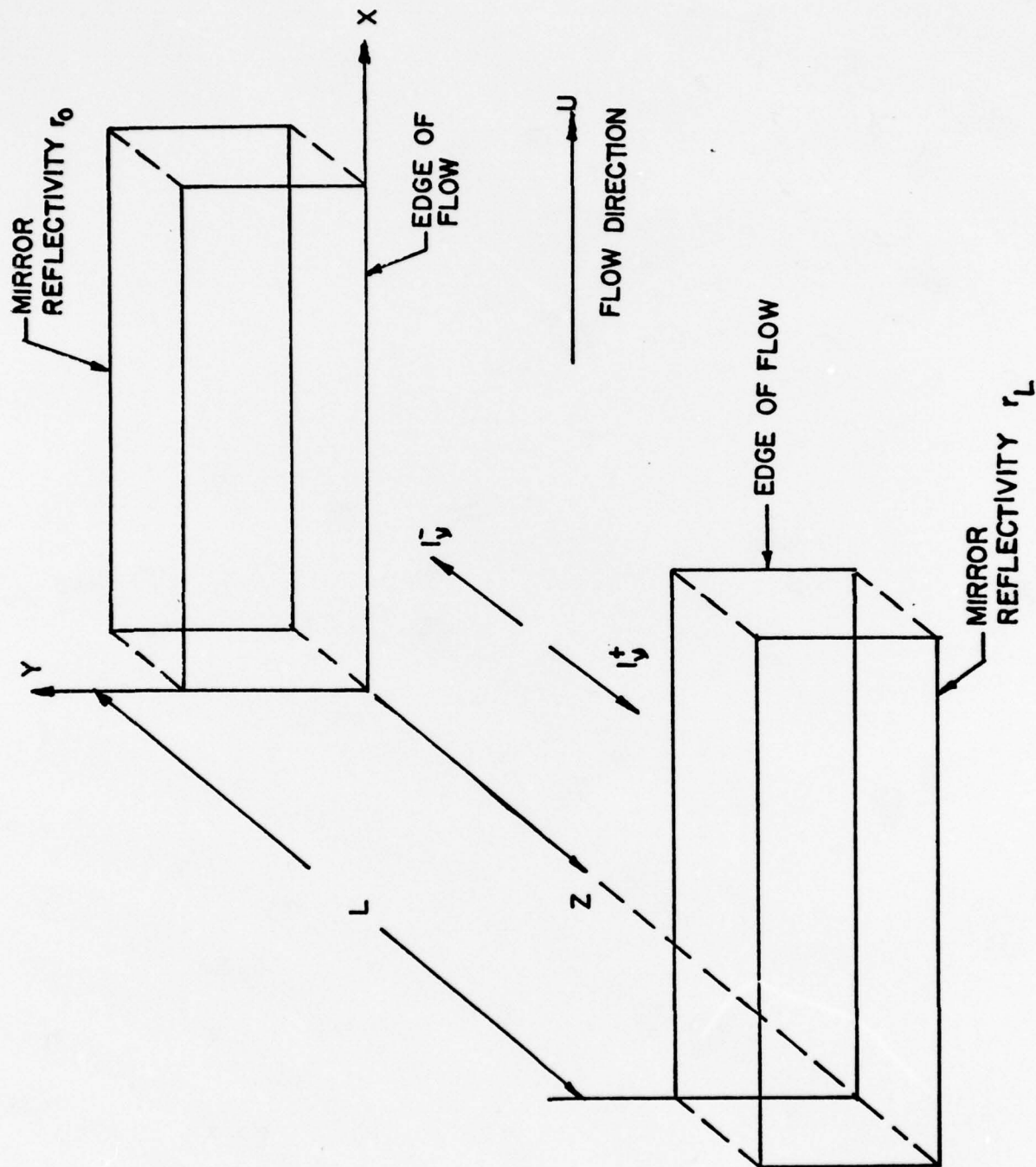
Figure 1. Flow and Optical Geometry.

of fluid, ρ is the density of the fluid, η_{UL} is a line shape function that is normalized according to

$$\int_0^\infty \eta_{UL}\, d\nu = 1 \tag{2.1-4}$$

B_{LU} is the Einstein coefficient, g_i is the statistical weight of state i, N_A is Avogadro's number and h is Planck's constant. The general solution of Eqs. (2.1-1) and (2.1-2) averaged over the narrow spike at $\nu_0 \overset{\sim}{\sim} \nu_{UL}$ is

$$I^+(Z) = I^+(0)\, \exp(\alpha_{\nu_{UL}} Z) + \overline{K}\,[\exp(\alpha_{\nu_{UL}} Z) - 1] \tag{2.1-5}$$

$$I^-(Z) = I^-(L)\, \exp[\alpha_{\nu_{UL}}(L-Z)] + \overline{K}\,[\exp(\alpha_{\nu_{UL}}[L-Z]) - 1] \tag{2.1-6}$$

where the average of S_ν over ν is approximated by, Ref. 1,

$$\overline{K} = \int S_\nu d\nu \leq \left| \int S_{\nu_{eq}} d\nu \right| = \frac{\sigma' T^4}{\pi} \tag{2.1-7}$$

and

$$\alpha_{\nu_{UL}} = hN_A \rho \nu_{UL} \phi(\nu_{UL}) B_{LU} [(g_L/g_U)\, n_U - n_L] \tag{2.1-8}$$

σ' is the Stefan-Boltzmann constant, $g_i = 2J_i + 1$ and the flow and chemistry are assumed independent of Z.

The quantities $I^+(0)$ and $I^-(L)$, which are determined by requiring Eqs. (2.1-5) and (2.1-6) to satisfy the mirror boundary conditions $I^+(0) = r_0 I^-(0)$ and $I^-(L) = r_L I^+(L)$, are

$$I^+(0) = r_0 \overline{K}[r_L \exp(2\alpha L) + (1-r_L)\exp(\alpha L) - 1]/[1-r_0 r_L \exp(2\alpha L)] \tag{2.1-9}$$

$$I^-(L) = r_L \overline{K}[r_0 \exp(2\alpha L) + (1-r_0)\exp(\alpha L) - 1]/[1-r_0 r_L \exp(2\alpha L)] \tag{2.1-10}$$

where the subscript ν_{UL} has been suppressed. With Eqs. (2.1-9) and

(2.1-10), the intensity averaged over Z is given by

$$I = \overline{I}^+ + \overline{I}^- = \overline{K}[(r_o + r_L - 2r_o r_L[1-\alpha L])\exp(2\alpha L)$$

$$+ 2(1 + r_o r_L - r_o - r_L)\exp(\alpha L) - 2(1 + \alpha L)$$

$$+ r_o + r_L]/\{\alpha L[1 - r_o r_L \exp(2\alpha L)]\} \qquad (2.1-11)$$

With this expression for I, the χ_{rad} term in the species equations for n_U and n_L is given by

$$\chi_{rad_{UL}} = \alpha_{\nu_{UL}} I_{\nu_{UL}}/hN_A \nu_{UL} \qquad (2.1-12)$$

The power contained in the transition UL is obtained by integrating

$$\frac{d\overline{P}}{dx} = hN_A \nu_{UL} Ly\chi_{rad_{UL}} \qquad (2.1-13)$$

where y is the height of the mirrors or active medium, whichever is smaller.

The retention of the spontaneous emission term, S_ν, in the radiative transfer equations has resulted in an explicit expression for the intensity in terms of the fluid variables. With this result, the χ_{rad} terms are simply nonlinear terms on the right hand sides of the species equations. Thresholds and cut offs are obtained as part of the solution of the differential equations for the flow variables.

The lengthy integration times associated with rotational nonequilibrium models are a direct consequence of the number of dependent variables and the stiffness of the differential equations. While the number of dependent variables is determined by the number of levels populated by the pumping reaction, the stiffness of the differential equations is

determined by the expression for I. The nonlinear cascade process which leads to saturation of a transition is primarily controlled by the $1-r_o r_L \exp(2\alpha L_e)$ term in the denominator of Eq. (2.1-11). At saturation, the denominator goes to zero to 8 or 9 significant figures; the resulting gain curves vs. x have sharp corners at saturation.

A reduction factor of about two in integration time can be realized by using the approximate expression for I, which was derived for the case $\alpha L_e \ll 1$, Ref. 1,

$$I = \frac{4 \bar{K} r_o r_L \alpha L_e}{1-r_o r_L - 2 r_o r_L \alpha L_e} \tag{2.1-14}$$

The reduction in run time occurs because the denominator in (2.1-14) goes to zero linearly rather than exponentially. The error in total power with this approximation is less than 0.6%. The only problem with this approximation is that it does not give the correct α_{sat} if αL_e is not much less than 1, which is the case for many high power chemical lasers. This difficulty can be overcome by defining an effective $r_o r_L$ which, when used in the approximate expression for I, gives the correct α_{sat}. This is accomplished as follows. The correct α_{sat} is given by

$$\alpha_{sat_e} = -\frac{1}{2L_e} \ln r_o r_L \tag{2.1-15}$$

From the linearized equation (2.1-14) for I, the approximate α_{sat_A} is

$$\alpha_{sat_A} = \frac{1-r_o r_L}{2 r_o r_L L_e} \tag{2.1-16}$$

By setting α_{sat_A} equal to α_{sat_e}, the required effective $r_o r_L$ can be solved for from Eq. (2.1-16)

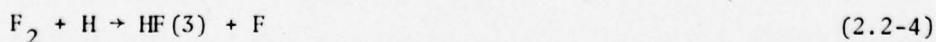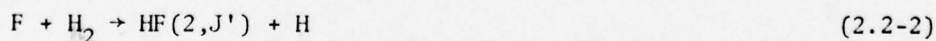$$(r_o r_L)_{eff} = \frac{1}{1+2L_e \alpha_{sat_e}} \tag{2.1-17}$$

When this expression for $(r_o r_L)_{eff}$ is used in the approximate equation for I, Eq. (2.1-14), the correct α_{sat_e} will be obtained from the approximate I. Thus, the present model employs the approximate equation for I with the $(r_o r_L)_{eff}$ defined by Eq. (2.1-17).

The stiffness of the differential equations can be controlled by the factor $\overline{K}$ which is the frequency average of the spontaneous emission term. Increasing $\overline{K}$ decreases the stiffness of the system while decreasing $\overline{K}$ increases the stiffness of the system. When the corners of the gain vs. x curves begin to round off, $\overline{K}$ is too large. The factor $\overline{K}$ is chosen to ensure that the corners of the gain vs. α curves are square. Typically, $\overline{K} = (10^{-2}$ to $10)\sigma'T^4/\pi$ is used.
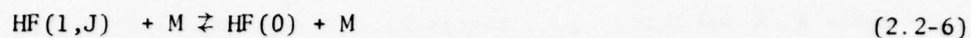
2.2 KINETICS MODEL

The original rotational nonequilibrium model[1] was a two level, premixed model in which the pumping reaction did not conserve mass and deactivation was included by collision with a generic species. To obtain quantitative predictions, the correct pumping and collisional deactivation reactions involving the primary deactivators HF, F, H and H_2 have been included. The model as it has developed to date comprises the following reaction set:

Pumping Reactions

$$F + H_2 \rightarrow HF(1,J) + H \tag{2.2-1}$$

$$F + H_2 \rightarrow HF(2,J') + H \tag{2.2-2}$$

$$F + H_2 \rightarrow HF(3) + H \tag{2.2-3}$$

$$F_2 + H \rightarrow HF(3) + F \tag{2.2-4}$$

Collisional Deactivation Reactions

$$HF(2,J') + M \rightleftarrows HF(1,J) + M \qquad (2.2\text{-}5)$$
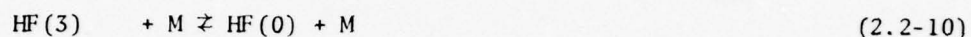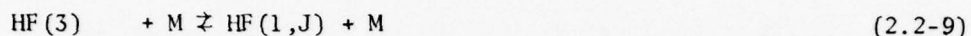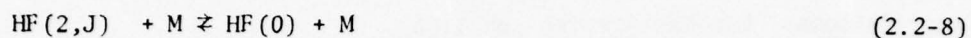
$$HF(1,J) + M \rightleftarrows HF(0) + M \qquad (2.2\text{-}6)$$

$$HF(3) + M \rightleftarrows HF(2,J') + M \qquad (2.2\text{-}7)$$

where M = HF, F, H and H_2.

$$HF(2,J) + M \rightleftarrows HF(0) + M \qquad (2.2\text{-}8)$$

$$HF(3) + M \rightleftarrows HF(1,J) + M \qquad (2.2\text{-}9)$$

$$HF(3) + M \rightleftarrows HF(0) + M \qquad (2.2\text{-}10)$$
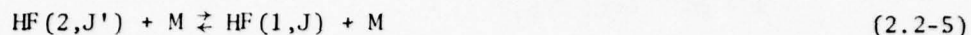
where M = HF, F and H.

Rotational Relaxation Reactions

$$HF(2,J') + M \rightleftarrows HF(2,J) + M \qquad (2.2\text{-}11)$$

$$HF(1,J) + M \rightleftarrows HF(1,J'') + M \qquad (2.2\text{-}12)$$
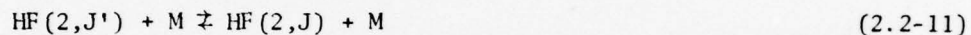
where M = HF, F, H, H_2, F_2, He, Ar.

The species denoted by Ar is included to take account of any other combus-
tion or dissociation products that may be present in the mixture and which
would contribute to the rotational relaxation but not to the collisional
deactivation of the lasing species.

While the above model is more extensive than originally anticipated,
it is quite concise compared to the kinetic models employed in codes such
as Blaze II[6] or Lamp[7]. To duplicate the species profiles calculated by
Blaze II, it was necessary to add the reactions (2.2-3), (2.2-4), (2.2-6),
and (2.2-7) to the model. The addition of the multiquantum deactivation
reactions (2.2-8) to (2.2-10) has a significant effect on the power and
the length of the lasing zone, see Chapter III.

The rate constants are input in the usual way as

$$k = AT^{-N} \exp(-B/RT) \qquad (2.2\text{-}13)$$

where A, N and B are input constants. The values used are those agreed upon by AFWL and Bell Aerospace Textron in June, 1977. For the J-dependent reactions, the rate constants are now J-dependent and are obtained as follows. For the pumping reactions,

$$k_{pvJ} = k_p^v \ f^v(J) \qquad (2.2\text{-}14)$$

where k_p^v are the global forward reaction rates which have been determined experimentally as a function of temperature and which are used in the rotational equilibrium models; $f^v(J)$ is the normalized distribution over the rotational states of each v level $(\sum_J f^v(J) = 1)$ which is obtained from experiment. For HF and DF, the data of Polanyi and Woodall[10] is used for $f^v(J)$. The pumping reactions are assumed to be one way reactions.

For the collisional deactivation reaction (2.2-5), the rate of change of HF(2,J') and HF(1,J) are expressed in terms of the deactivation rate constants as

$$
\begin{aligned}
\chi_{ch\ 1,J} = \rho^2 \sum_M n_M \Bigg\{ & \sum_{J'=0}^{J} n_{HF}(2,J') k_{2,J;1,J'}^M G_{J'}^J \\
& + \sum_{J'=J+1}^{J_M} n_{HF}(2,J') \ k_{2,J';1,J}^M \\
& - n_{HF}(1,J) \ \exp(-hc\omega_{21}/kT) \Bigg[\sum_{J'=0}^{J} k_{2,J;1,J'}^M \\
& + \sum_{J'=J+1}^{J_M} k_{2,J';1,J}^M \ G_J^{J'} \Bigg] \Bigg\}
\end{aligned}
\qquad (2.2\text{-}15)
$$

$$\chi_{ch\ 2,J'} = -\rho^2 \sum_M n_M \left\{ n_{HF}(2,J') \left[\sum_{\underline{J}=0}^{J'} k^M_{2,J';1,J} \right. \right.$$

$$+ \sum_{J=J'+1}^{J_M} k^M_{2,J;1,J'}\ G^J_{J'} \Bigg]$$

$$- \exp(-hc\omega_{21}/kT) \left[\sum_{\underline{J}=0}^{J'} n_{HF}(1,J)k^M_{2,J';1,J}\ G^{J'}_J \right.$$

$$+ \left. \left. \sum_{J=J'+1}^{J_M} n_{HF}(1,J)k^M_{2,J;1,J'} \Bigg] \right\} \qquad (2.2\text{-}16)$$

where n_i is the mole mass ratio of species i. Since M does not change during the reaction, there is no χ_{ch} term for the M in these reactions.

$$G^{J'}_J = (g_{J'}/g_J)\ \exp[-(E_{J'} - E_J)/kT] \qquad (2.2\text{-}17)$$

$$g_{J'} = 2J' + 1,\ g_J = 2J + 1 \qquad (2.2\text{-}18)$$

$$E_J = hc B_e J(J + 1) \qquad (2.2\text{-}19)$$

$$k^M_{2,J';1,J} = ZC_1 T^{-(N+1)}\exp[-C_2 hc\omega_{21}/kT] \qquad (2.2\text{-}20)$$

$$\times\ \exp[-C_2(E_{J'} - E_J)/kT] \qquad (2.2\text{-}21)$$

$$Z = \sigma^2 \left(\frac{8\pi kT}{\mu}\right)^{1/2} N_A \qquad (2.2\text{-}22)$$

$$\sigma = \frac{\sigma_M + \sigma_{HF}}{2} \qquad (2.2\text{-}23)$$

$$\mu = m_H M_{HF} M_M / (M_{HF} + M_M) \qquad (2.2\text{-}24)$$

C_1 and C_2 are input constants determined by requiring that the following relation be satisfied

$$k^M_{2,1} = \sum_J \sum_{J'} F(J')k^M_{2,J';1,J} \qquad (2.2\text{-}25)$$

where the global rate constant, which is determined experimentally, is expressed as

$$k_{2,1}^{M} = AT^{-N}\exp(-B/RT) \tag{2.2-26}$$

and $F(J')$ is the Boltzmann rotational distribution function. When M is the lasing species, n_M is

$$n_M = \sum_v \sum_J n_{HF}(v,J). \tag{2.2-27}$$

For reaction (2.2-6), the χ_{ch} terms are

$$\chi_{ch_{1,J}} = -\rho^2 \left[n_{HF}(1,J) - \exp(-hc\omega_{10}/kT)F(J)n_{HF}(0) \right]$$

$$\times \sum_M n_M k_{2,1}^{M} \tag{2.2-28}$$

$$\chi_{ch_0} = \rho^2 \left[n_{HF}(1) - \exp(-hc\omega_{10}/kT)n_{HF}(0) \right] \sum_M n_M k_{1,0}^{M} \tag{2.2-29}$$

where the detailed rate constants are given by

$$k_{1,J;0}^{M} = k_{1,0}^{M} \tag{2.2-30}$$

$$k_{0;1,J}^{M} = k_{0,1}^{M} F(J) \tag{2.2-31}$$

where $F(J)$ is the Boltzmann rotational distribution function

$$F(J) = \frac{(2J+1)}{Q_{rot}} \exp[-E_J/kT] \tag{2.2-32}$$

$$Q_{rot} = T/\sigma\theta_r \tag{2.2-33}$$

and σ is 1 for a heteronuclear molecule and 2 for a homonuclear molecule. The relations (2.2-30) and (2.2-31) between the detailed and the global rate constants result from the requirement that when Eq. (2.2-28) is

summed over J, the rotational equilibrium form of χ_{ch_1} is obtained. When M is the lasing species, n_M is given by Eq. (2.2-27).

For reaction (2.2-7) the χ_{ch} terms are given by

$$\chi_{ch_{2,J'}} = \rho^2 \left[n_{HF}(3)F(J') - n_{HF}(2,J')\exp(-hc\omega_{32}/kT) \right]$$

$$x \sum_M n_M k^M_{3,2} \tag{2.2-34}$$

$$\chi_{ch_3} = -\rho^2 \left[n_{HF}(3) - n_{HF}(2)\exp(-hc\omega_{32}/kT) \right] \sum_M n_M k^M_{3,2} \tag{2.2-35}$$

where the detailed rate constants are related to the global rate constants by

$$k^M_{3;2,J'} = k^M_{3,2}F(J') \tag{2.2-36}$$

$$k^M_{2,J';3} = k^M_{2,3} = \exp(-hc\omega_{32}/kT) \; k^M_{3,2} \tag{2.2-37}$$

where $F(J')$ is the Boltzmann rotational distribution function.

The χ_{ch} terms for the multiquantum deactivation reactions (2.2-8) to (2.2-10) are

$$\chi_{ch_{2,J'}} = -\rho^2 n_M k^M_{20} \left[n_{HF}(2,J') - n_{HF}(0)\exp(-hc\omega_{20}/kT) \right] \tag{2.2-38}$$

$$\chi_{ch_3} = -\rho^2 n_M \left\{ k^M_{30}[n_{HF}(3) - n_{HF}(0)\exp(-hc\omega_{30}/kT)] \right.$$

$$\left. + k^M_{31}[n_{HF}(3) - \exp(-hc\omega_{31}/kT)n_{HF}(1)] \right\} \tag{2.2-39a}$$

$$\chi_{ch_0} = \rho^2 n_M \left\{ k^M_{30}[n_{HF}(3) - \exp(-hc\omega_{30}/kT)n_{HF}(0)] \right.$$

$$\left. + k^M_{20}[n_{HF}(2) - n_{HF}(0)\exp(-hc\omega_{20}/kT)] \right\} \tag{2.2-39b}$$

$$\chi_{ch_{1,J}} = \rho^2 n_M k^M_{31}[F(J)n_{HF}(3) - \exp(-hc\omega_{31}/kT)n_{HF}(1,J)] \tag{2.2-40}$$

where n_M is given by Eq. (2.2-27) when M = HF and the detailed rate constants

are related to the global rate constants by

$$k^M_{2,J';0} = k^M_{20} \tag{2.2-41a}$$

$$k^M_{0;2,J'} = F(J')k^M_{20} \exp(-hc\omega_{20}/kT) \tag{2.2-41b}$$

$$k^M_{3;1,J} = k^M_{31}F(J) \tag{2.2-42a}$$

$$k^M_{1,J;3} = k^M_{13} = k^M_{31} \exp(-hc\omega_{31}/kT) \tag{2.2-42b}$$

Since ω_{20}/T, ω_{31}/T and ω_{30}/T are greater than 10 for the temperature range of interest for most chemical lasers, the backward reaction for the multi-quantum deactivations can be neglected. With this approximation, the χ_{ch} terms become

$$\chi_{ch_{2,J'}} \overset{\sim}{\sim} -\rho^2 n_{HF}(2,J') \sum_M n_M k^M_{20} \tag{2.2-43}$$

$$\chi_{ch_3} \overset{\sim}{\sim} -\rho^2 n_{HF}(3) \sum_M n_M [k^M_{30} + k^M_{31}] \tag{2.2-44a}$$

$$\chi_{ch_o} \overset{\sim}{\sim} \rho^2 [n_{HF}(3) \sum_M n_M k^M_{30} + n_{HF}(2) \sum_M n_M k^M_{20}] \tag{2.2-44b}$$

$$\chi_{ch_{1,J}} \overset{\sim}{\sim} \rho^2 n_{HF}(3)F(J) \sum_M n_M k^M_{31} \tag{2.2-45}$$

where $F(J)$ is the Boltzmann rotational distribution function.

For the rotational relaxation reactions (2.2-11) and (2.2-12), the χ_{ch} are expressed in terms of the deactivation rate constants as

$$\chi^1_{ch_r} = -\rho^2 Z^{HF}_r (n_{HF} + \sum_M n_M E_{Mr}) \left[n_{HF}(1,J) \left\{ \sum_{J''=0}^{J-1} P^J_{J''} \right. \right.$$

$$\left. + \sum_{J''=J+1}^{J_M} P^{J''}_J G^{J''}_J \right\} - \sum_{J''=0}^{J-1} P^J_{J''} G^J_{J''} n_{HF}(1,J'')$$

$$\left. - \sum_{J''=J+1}^{J_M} P^{J''}_J n_{HF}(1,J'') \right] \tag{2.2-46}$$

$$\chi^2_{ch_r} = -\rho^2 z_r^{HF}(n_{HF} + \sum_M n_M E_{Mr})\left[n_{HF}(2,J')\left(\sum_{J=0}^{J'-1} P_J^{J'}\right.\right.$$

$$\left.+ \sum_{J=J'+1}^{J_M} P_{J'}^{J} G_{J'}^{J}\right) - \sum_{J=0}^{J'-1} P_J^{J'} G_J^{J'} n_{HF}(2,J)$$

$$\left. - \sum_{J=J'+1}^{J_M} P_{J'}^{J} n_{HF}(2,J)\right] \qquad (2.2\text{-}47)$$

where $n_{HF} = \sum_v \sum_J n_{HF}(v,J)$, G_L^U is given by Eq. (2.2-17), the rotational transition probability[11] P_L^U is given by

$$P_L^U = C_1 \exp[-C_2(E_U - E_L)/kT] \qquad (2.2\text{-}48)$$

z_r^{HF} is given by (2.2-22) with $M = HF$. C_1 and C_2 are input constants determined from experiment[12,13]. E_M is the rotational relaxation efficiency of species M compared to HF.

2.3 FLUID MECHANICS MODEL

To keep the number of dependent variables to a minimum, $P(x)$, $T(x)$, $u(x)$, the mass flow rate remaining in the primary, $\dot{m}_p(x)$, the mass flow rate remaining in the secondary, $\dot{m}_s(x)$, and the ratio of the thickness of the mixed stream to the geometric thickness of the flow, Le/Lg, are input as functions of x from a detailed rotational equilibrium model such as Blaze II. These functions are input as polynomials in x where the coefficients are determined by a least squares fit to the Blaze II profiles. Experience has shown that the following polynomials give the best fits to these variables:

$$P = C_{p9}x^9 + C_{p8}x^8 + C_{p7}x^7 + C_{p6}x^6 + C_{p5}x^5 + C_{p4}x^4 \qquad (2.3\text{-}1)$$

$$+ C_{p3}x^3 + C_{p2}x^2 + C_{p1}x + C_{p0}$$

$$T = C_{T9}x^9 + C_{T8}x^8 + C_{T7}x^7 + C_{T6}x^6 + C_{T5}x^5 + C_{T4}x^4$$
$$+ C_{T3}x^3 + C_{T2}x^2 + C_{T1}x + C_{T0} \qquad (2.3\text{-}2)$$

$$u = C_{u9}x^9 + C_{u8}x^8 + C_{u7}x^7 + C_{u6}x^6 + C_{u5}x^5 + C_{u4}x^4$$
$$+ C_{u3}x^3 + C_{u2}x^2 + C_{u1}x + C_{u0} \qquad (2.3\text{-}3)$$

$$\dot{m}_p = G_{p1}x + G_{p2}x^{1/2} + \dot{m}_{p0} \qquad (2.3\text{-}4)$$

$$\dot{m}_s = G_{s1}x + G_{s2}x^{1/2} + \dot{m}_{s0} \qquad (2.3\text{-}5)$$

$$L_e/L_g = A_M x^{3/4} + B_M x^{1/2} + C_M x \qquad (2.3\text{-}6)$$

The coefficients of these polynomials are input data. For the ninth order polynomials, the coefficient must be input to nine significant figures.

A schematic of a typical mixing region is shown in Fig. 2. From Ref. 6, the mixing term which appears in the species equation is given by

$$M_{ni} = \frac{1}{\dot{m}}\left[(n_i - n_{iso})\frac{d\dot{m}_s}{dx} + (n_i - n_{ipo})\frac{d\dot{m}_p}{dx}\right] \qquad (2.3\text{-}7)$$

where $\dot{m}$ is the flow rate of the mixed stream, n_i is the mole mass ratio of species i, n_{iso} is the value of the mole mass ratio of species i in the secondary stream, n_{ipo} is the value of the mole mass ratio of species i in the primary stream. For the products of reaction, $n_{iso} = n_{ipo} = 0$; for reactants from the primary stream, $n_{iso} = 0$; for reactants from the secondary stream, $n_{ipo} = 0$. The mass flow rate of the mixed stream is given by

$$\dot{m} = \dot{m}_{po} - \dot{m}_p + \dot{m}_{so} - \dot{m}_s \qquad (2.3\text{-}8)$$

where $\dot{m}_{po}$ is the initial primary flow rate, $\dot{m}_{so}$ is the initial secondary flow rate.
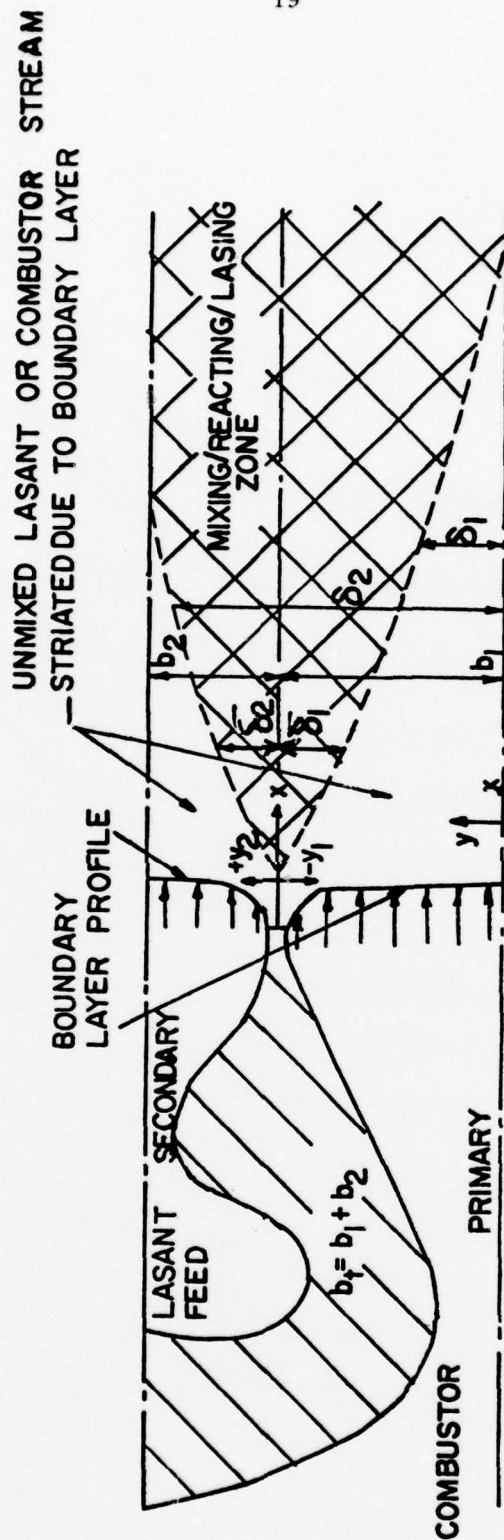
Figure 2. Schematic of the mixing region.

The resulting species equations are:

$$\frac{dn_{HF}(1,J)}{dx} = \frac{\rho}{u} \left\{ k_p^1 f^1(J) n_F n_{H_2} \right.$$

$$+ \sum_M \left\{ n_M z_c^M \left[\sum_{J'=0}^{J} n_{HF}(2,J') P_{2,J';1,J}^M G_{J'}^J \right. \right.$$

$$+ \sum_{J'=J+1}^{J_M} n_{HF}(2,J') P_{2,J';1,J}^M - \exp(-hc\omega_{21}/kT) \left(\sum_{J'=0}^{J} P_{2,J;1,J'}^M \right.$$

$$\left. + \sum_{J'=J+1}^{J_M} P_{2,J';1,J}^M G_J^{J'} \right) n_{HF}(1,J) \right] \right\}$$

$$- z_r^{HF} (n_{HF} + \sum_M n_M E_{Mr}) \left[n_{HF}(1,J) \left(\sum_{J''=0}^{J-1} P_{J''}^J + \sum_{J''=J+1}^{J_M} P_J^{J''} G_J^{J''} \right) \right.$$

$$\left. - \sum_{J''=0}^{J-1} P_{J''}^J G_{J''}^J n_{HF}(1,J'') - \sum_{J''=J+1}^{J_M} P_J^{J''} n_{HF}(1,J'') \right]$$

$$- [n_{HF}(1,J) - \exp(-hc\omega_{10}/kT) F(J) n_{HF}(0)] \sum_M n_M k_{10}^M$$

$$\left. + n_{HF}(3) F(J) \sum_M n_M k_{31}^M \right\}$$

$$+ \frac{1}{\rho u} [\chi(1,J,-1) + \chi(1,J,1)] + \frac{1}{\dot{m}} \left[\frac{d\dot{m}_p}{dx} + \frac{d\dot{m}_s}{dx} \right] n_{HF}(1,J)$$

$$(2.3-9)$$

$$\frac{dn_{HF}(2,J')}{dx} = \frac{\rho}{u} \left\{ k_p^2 f^2(J') n_F n_{H_2} - \sum_M \left[n_M Z_c^M \left[n_{HF}(2,J') \left\{ \sum_{J=0}^{J'} P_{2,J';1,J}^M \right. \right. \right. \right.$$

$$\left. + \sum_{J=J'+1}^{J_M} P_{2,J;1,J'}^M G_{J'}^J \right\} - \exp(-hc\omega_{21}/kT) \left\{ \sum_{J=0}^{J'} n_{HF}(1,J) P_{2,J';1,J}^M G_J^{J'} \right.$$

$$\left. \left. \left. + \sum_{J=J'+1}^{J_M} n_{HF}(1,J) P_{2,J;1,J'}^M \right\} \right] \right] \right\}$$

$$- Z_r^{HF} \left(n_{HF} + \sum_M n_M E_{Mr} \right) \left[n_{HF}(2,J') \left\{ \sum_{J=0}^{J'-1} P_J^{J'} + \sum_{J=J'+1}^{J_M} P_J^J G_{J'}^J \right\} \right.$$

$$\left. - \sum_{J=0}^{J'-1} P_J^{J'} G_J^{J'} n_{HF}(2,J) - \sum_{J=J'+1}^{J_M} P_{J'}^J n_{HF}(2,J) \right] - n_{HF}(2,J') \sum_M n_M k_{20}^M$$

$$+ [n_{HF}(3) F(J) - n_{HF}(2,J) \exp(-hc\omega_{32}/kT)] \sum_M n_M k_{32}^M \right\}$$

$$- \frac{1}{\rho u} [\chi(1,J'+1,-1) + \chi(1,J'-1,1)] + \frac{1}{\dot{m}} \left[\frac{d\dot{m}_p}{dx} + \frac{d\dot{m}_s}{dx} \right] n_{HF}(2,J')$$

$$\text{(2.3-10)}$$

$$\frac{dn_F}{dx} = -\frac{\rho}{u} \left\{ k_{PT} n_F n_{H_2} - k_{PHT} n_H n_{F_2} \right\}$$

$$+ \frac{1}{\dot{m}} \left[n_F \frac{d\dot{m}_s}{dx} + (n_F - n_{F0}) \frac{d\dot{m}_p}{dx} \right] \qquad \text{(2.3-11)}$$

$$\frac{dn_{H_2}}{dx} = -\frac{\rho}{u} k_{PT} n_F n_{H_2} + \frac{1}{\dot{m}}\left[(n_{H_2} - n_{H_{2_0}})\frac{d\dot{m}_s}{dx} + n_{H_2}\frac{d\dot{m}_p}{dx}\right] \qquad (2.3\text{-}12)$$

$$\frac{dn_H}{dx} = \frac{\rho}{u}\left[k_{PT} n_F n_{H_2} - k_{PHT} n_H n_{F_2}\right] + \frac{1}{\dot{m}}\left[\frac{d\dot{m}_s}{dx} + \frac{d\dot{m}_p}{dx}\right]n_H \qquad (2.3\text{-}13)$$

$$\frac{dn_{He}}{dx} = \frac{1}{\dot{m}}\left[\left(n_{He} - n_{He_{so}}\right)\frac{d\dot{m}_s}{dx} + \left(n_{He} - n_{He_{po}}\right)\frac{d\dot{m}_p}{dx}\right] \qquad (2.3\text{-}14)$$

$$\frac{dn_{Ar}}{dx} = \frac{1}{\dot{m}}\left[\left(n_{Ar} - n_{Ar_{so}}\right)\frac{d\dot{m}_s}{dx} + \left(n_{Ar} - n_{Ar_{po}}\right)\frac{d\dot{m}_p}{dx}\right] \qquad (2.3\text{-}15)$$

$$\frac{dn_{F_2}}{dx} = -\frac{\rho}{u} k_{PHT} n_H n_{F_2} + \frac{1}{\dot{m}}\left[(n_{F_2} - n_{F_{2so}})\frac{d\dot{m}_s}{dx}\right.$$
$$\left. + (n_{F_2} - n_{F_{2po}})\frac{d\dot{m}_p}{dx}\right] \qquad (2.3\text{-}16)$$

$$\frac{dn_{HF}(0)}{dx} = \frac{\rho}{u}\left\{\left[n_{HF}(1) - \exp(-hc\omega_{10}/kT)n_{HF}(0)\right]\sum_M n_M k_{10}^M + n_{HF}(2)\sum_M n_M k_{20}^M\right.$$
$$\left. + n_{HF}(3)\sum_M n_M k_{30}^M\right\} + \frac{1}{\dot{m}}\left[\frac{d\dot{m}_s}{dx} + \frac{d\dot{m}_p}{dx}\right]n_{HF}(0) \qquad (2.3\text{-}17)$$

$$\frac{dn_{HF}(3)}{dx} = \frac{\rho}{u} \left\{ n_F n_{H_2} k_p^3 - [n_{HF}(3) - n_{HF}(2)\exp(-hc\omega_{32}/kT)]\Sigma n_M k_{32}^M \right.$$

$$\left. + n_H n_{F_2} k_{PH}^3 - n_{HF}(3)\Sigma_M n_M [k_{30}^M + k_{31}^M] \right\}$$

$$+ \frac{1}{\dot{m}} \left[\frac{d\dot{m}_s}{dx} + \frac{d\dot{m}_p}{dx} \right] n_{HF}(3) \tag{2.3-18}$$

where

$$k_{PT} = k_p^1 + k_p^2 + k_p^3 \tag{2.3-19}$$

$k_{PHT} = k_{PH}^3$ and k_{PH}^3 is the sum of k_{PH}^V over $v = 3$ to 6. With $J_M = 20$, there are 50 differential equations for the mole mass ratios of the various species in the mixture. The initial values of the mole mass ratios of the species are calculated from the initial flow rates of the species in the primary and secondary streams,

$$n_{ipo} = \frac{\dot{m}_{ipo}}{\dot{m}_{po} W_i} \tag{2.3-20}$$

$$n_{iso} = \frac{\dot{m}_{iso}}{\dot{m}_{so} W_i} \tag{2.3-21}$$

where $\dot{m}_{po}$ and $\dot{m}_{so}$ are the initial primary and secondary mass flow rates ($\dot{m}_{po} = \sum_i \dot{m}_{ipo}$ and $\dot{m}_{so} = \sum_i \dot{m}_{iso}$), and W_i is the molecular weight of species i.

In some cases, F atom recombination at the wall is important. This effect if included by varying the F atom concentration in the primary stream

from zero at the wall to its value in the core of the primary flow. This results in a variation of $n_{F_{po}}$, the value of n_F at the edge of the mixing layer which appears in the mixing terms, with x as shown in Fig. 3. The boundary layer profile is used to provide the variation of n_F from the wall to the core. The mole mass ratio is related to the species mass fraction by

$$n_{i_o}(y) = f_i/W_i \qquad (2.3\text{-}22)$$

where f_i is the mass fraction of species i and $n_{i_o}(y)$ is the initial value of the mole mass ratio of species i that should be used in the mixing terms. The value of y depends upon the value of x and the thickness of the mixing layer $y = \overline{\delta}_1(x)$ at that value of x. Thus,

$$n_{F_o} = n_{F_{wall}} + [n_{F_{core}} - n_{F_{wall}}] \left[\frac{\overline{\delta}_1(x)}{\delta_{BL}}\right]^{3/2} \qquad (2.3\text{-}23)$$

$$n_{F_{2_o}} = n_{F_{2wall}} + \left[n_{F_{2core}} - n_{F_{2wall}}\right]\left[\frac{\overline{\delta}_1(x)}{\delta_{BL}}\right]^{3/2} \qquad (2.3\text{-}24)$$

Since the number of F atoms must be conserved, $n_{F_{2wall}}$ is related to $n_{F_{wall}}$ by

$$n_{F_{2wall}} = \frac{1}{2} n_{F_{core}} + n_{F_{2core}} - \frac{1}{2} n_{F_{wall}} \qquad (2.3\text{-}25)$$

where the $\frac{1}{2}$ occurs because $W_{F2} = 2W_F$. The boundary layer profile is input from Blaze II as

$$\frac{\overline{\delta}_1(x)}{b_1} = ax^{3/4} + bx^{1/2} \qquad (2.3\text{-}26)$$

where $\delta_{BL} = BLT*b_1$ and BLT is the fraction of the primary nozzle that is
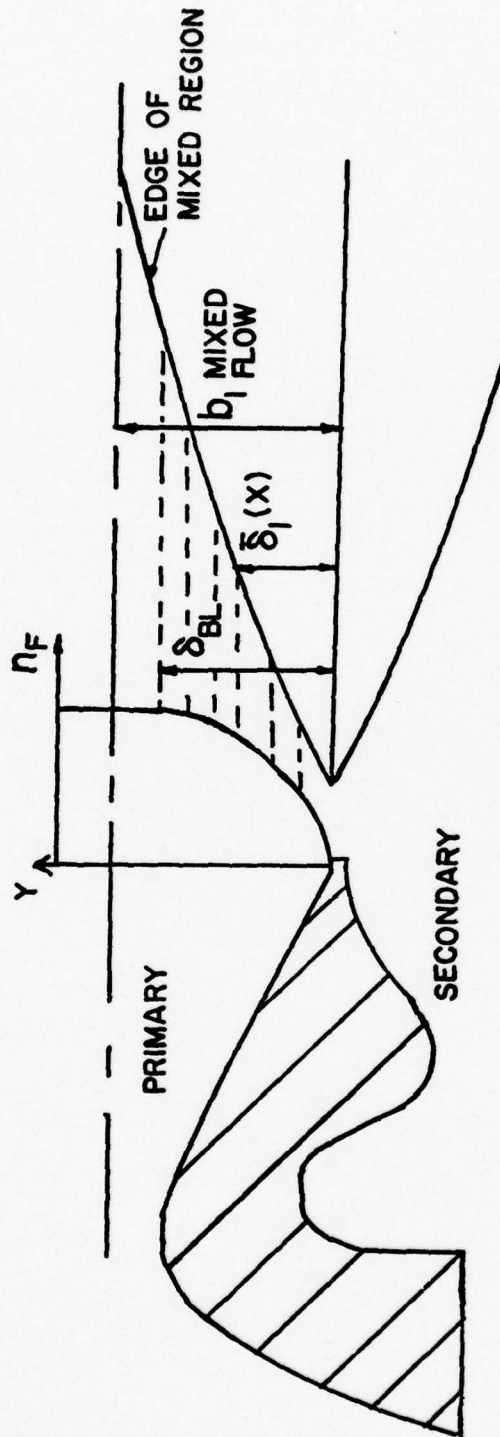
Figure 3. Schematic of the F atom profile in the primary stream due to wall recombination. The intersection of the F atom profile with the edge of the mixing region provides the value of $n_{F_{PO}}(x)$ which is used in the mixing term in the species equation.

filled by the boundary layer, b_1 is the half height of the primary nozzle exit plane, and a and b are curve fit constants determined by fitting (2.3-26) to the Blaze II data.

The final element of the model is the inclusion of the effect of lasing on the 1 to 0 band. This was necessary to obtain quantitative agreement with the Blaze II results. Since the present model is a two level model, the effect of lasing on the 1 to 0 band was included as a rate constant k_{rad}^{10} which was determined from the Blaze II value of $\chi_{rad}^{10}(x)$ by setting

$$\chi_{rad}^{10} = k_{rad}^{10} \; \rho^2 n_{HF} n_{HF}(1) \tag{2.3-27}$$

which simulates the depopulation of HF(1) by lasing as a collisional deactivation by HF. From Eq. (2.3-27), $k_{rad}^{10}(x)$ is obtained and input as a function of x in the program. The rate constant for the deactivation of HF(1) by HF is then written as

$$k_{10} = k_{10}^{HF} + k_{rad}^{10} \tag{2.3-28}$$

and the effect of lasing on the depopulation of HF(1) is taken into account in the collisional deactivation reaction.

Since the present model is a two level model as far as the calculation of laser power is concerned, the gain is given by

$$\alpha(v,J,m) = \rho h N_A \omega_{UL} \phi(\omega_{UL}) B_{LU}[(g_L/g_U)n_U - n_L] \tag{2.3-29}$$

where for a doppler profile

$$\omega_{UL}\phi_D = c\left(\frac{W_L}{2\pi R}\right)^{1/2} T^{-1/2} \tag{2.3-30}$$

W_L is the molecular weight of the lasing species,

$$B_{LU} = \frac{4\pi^3}{3h^2c} |M|^2 \left(\frac{2J+1+m}{2J+1}\right) \tag{2.3-31}$$

$$g_L = 2J + 1, \ g_U = 2J + 1 + 2m \tag{2.3-32}$$

and $m = -1$ for the P branch and $m = +1$ for the R branch. For a Voight profile,

$$\phi_{Voight} = \phi_D K(o,y) \tag{2.3-33}$$

where $K(o,y)$ is given in Ref. 6. The power in each transition is given by

$$P(x,v,J,m) = \frac{hN_A c\omega_{21}}{F_{JM}} \int_0^x A_{mT}\chi(v,J,m)dx \tag{2.3-34}$$

where $A_{mT} = \dot{m}/\rho u$, $\dot{m}$ is the total flow rate in the mixed flow and

$$F_{Jm} = \omega_{21}/\omega_{UL} = \{1 + [m(2J+1+m)\theta_r k/hc\omega_{21}]\}^{-1} \tag{2.3-35}$$

The density ρ is given by

$$\rho = PW/RT \tag{2.3-36}$$

where the molecular weight of the mixture is given by

$$W = (\sum_i n_i)^{-1} \tag{2.3-37}$$

and R is the universal gas constant per mole.

In the next chapter, the present model, which is denoted by the name MNORO, is compared to the Blaze II results for the arc driven laser as well as for the combustion driven CL XI case. From these comparisons, the essential elements of a quantitative model can be identified.
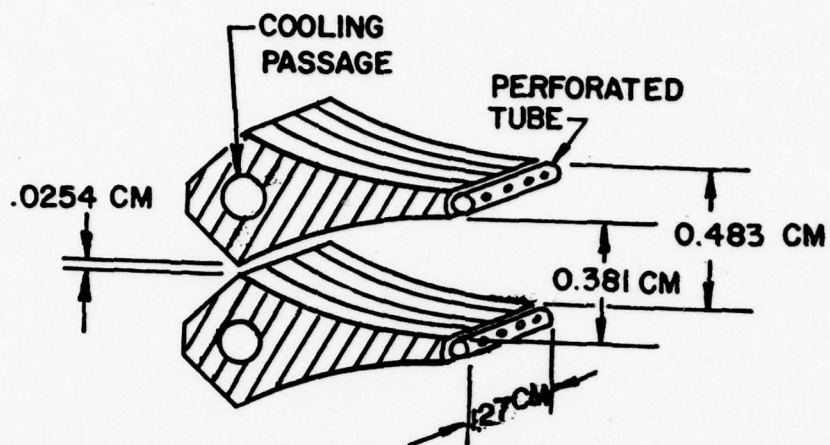
III. COMPARISON WITH THE BLAZE II MODEL

In attempting to develop a simplified cw chemical laser model that will give quantitative predictions, it is necessary to carry out as detailed comparisons with other models or experimental data as possible. In the present study, two diverse cases were selected for initial baselining of the model. One is an Aerospace[9] arc driven cw HF power spectral case and the other is the Bell Aerospace Textron CL XI lasing lines case[14].
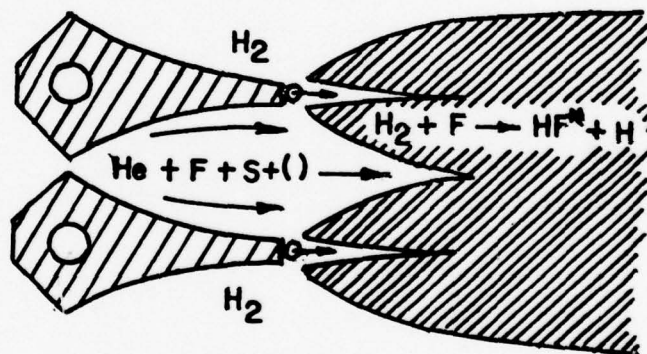
3.1 THE AEROSPACE ARC DRIVEN LASER

The Aerospace nozzle is shown in Fig. 4. The case chosen for baselining was the power spectral run[9], the flow conditions for which are given in Table I. The optical cavity was a Fabry-Perot resonator composed of two flats. The spectra was taken by hole outcoupling through one of the flat mirrors at 1.905 cm downstream from the nozzle exit plane. In both the Blaze II and the present model, the SF_6 was assumed completely dissociated; the sulfur and O_2 were treated as inert species which were represented by Argon in both models. The experimental power spectral distribution is shown in Fig. 5. Because of the uncertainties in the modeling of the spray bar mixing and in the percent dissociation of SF_6 in the arc, no real attempt to match the experimental data was made; rather, the elements in the present simplified model which are required to match the Blaze II results for the same initial conditions are identified through the comparison of the two models.

The Blaze II fluid dynamic profiles together with the resulting polynomial fits used in MNORO are shown in Figs. 6-10. As can be seen, the polynomials give an excellent representation of the fluid dynamic variables.

The Blaze II and MNORO H, F and H_2 profiles are compared in Fig. 11. As long as the production of HF(3) by the pumping reaction is included,

COOLING
PASSAGE

PERFORATED
TUBE

.0254 CM

0.483 CM

0.381 CM

.127CM

MULTIPLE NOZZLE

H_2

$H_2 + F \longrightarrow HF^* + H$

$He + F + S + ( ) \longrightarrow$

H_2

DIFFUSION MIXING

Figure 4.   Schematic of the Aerospace laser nozzle.

Species	$\dot{m}$ gm/s	L, cm	P torr
SF_6	0.5	17.78	1.4
He	2.06		
O_2	0.75	T_p °K	T_s °K
H_2	1.25	160	80

Table I. Aerospace CW HF Laser Power Spectral Run Conditions.

AEROSPACE CW HF LASER EXPERIMENTAL POWER SPECTRAL DISTRIBUTION
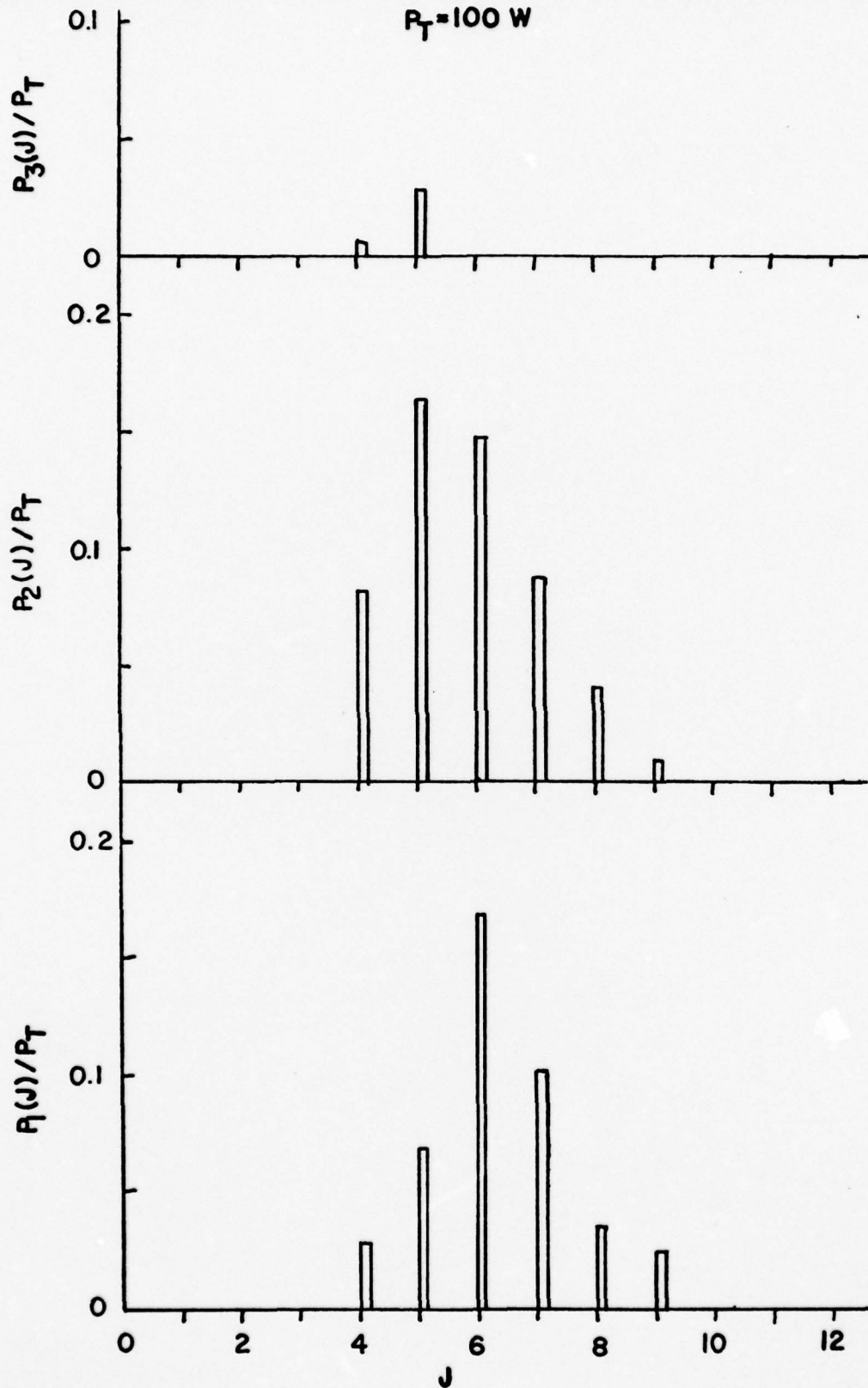$P_T = 100$ W

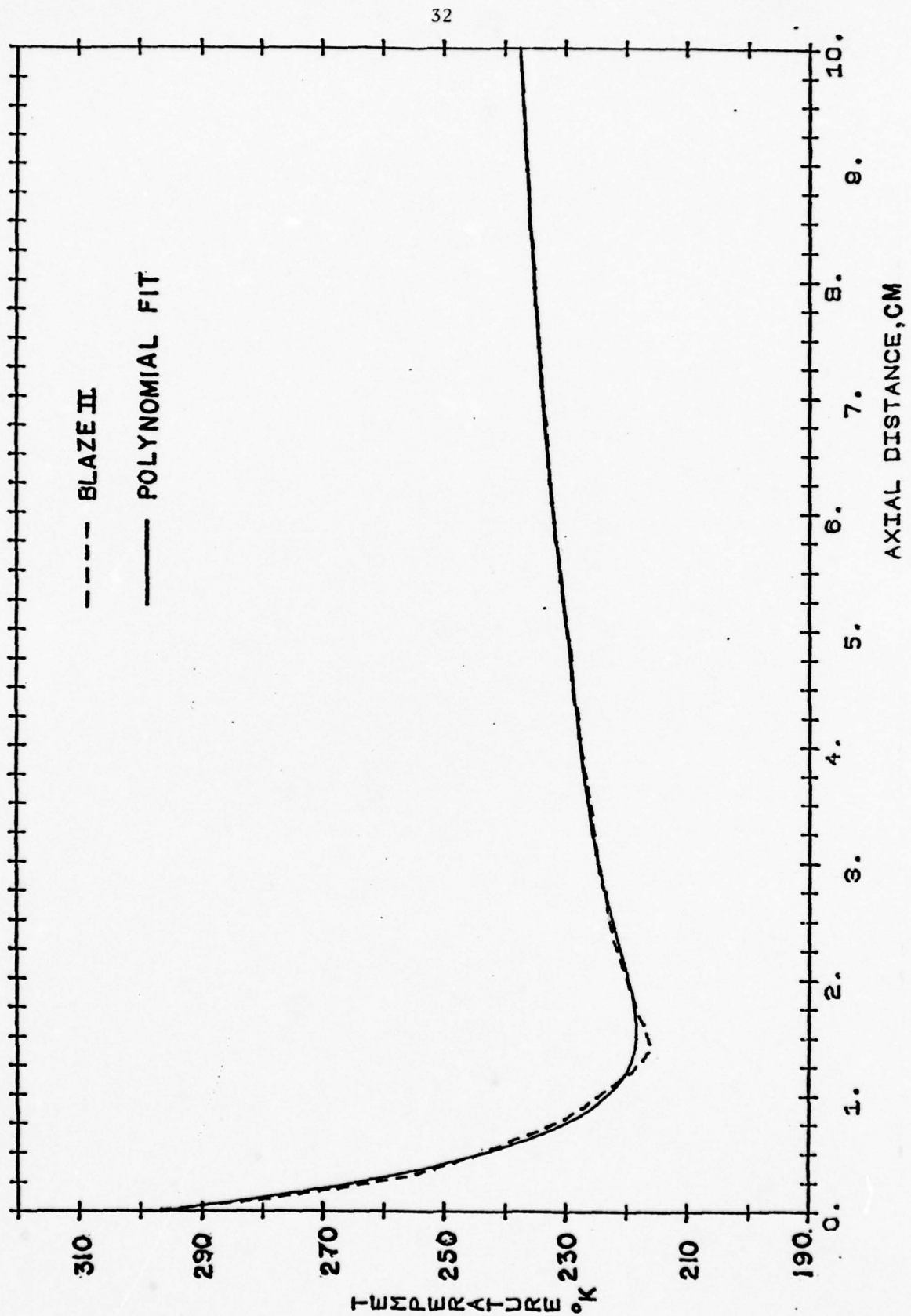Figure 5. Aerospace laser cw HF experimental power spectral distribution[9].

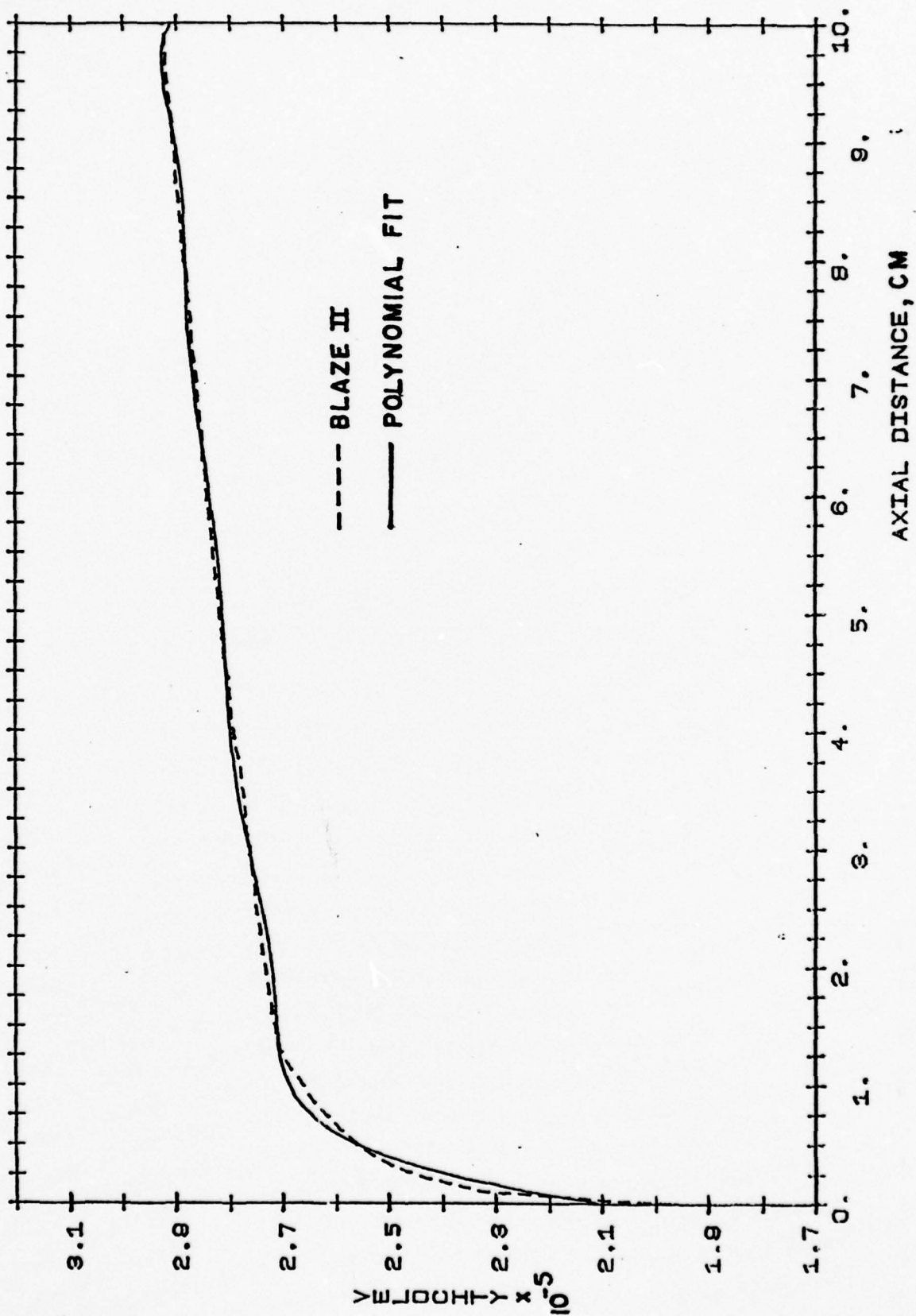Figure 6. Aerospace laser temperature profile.

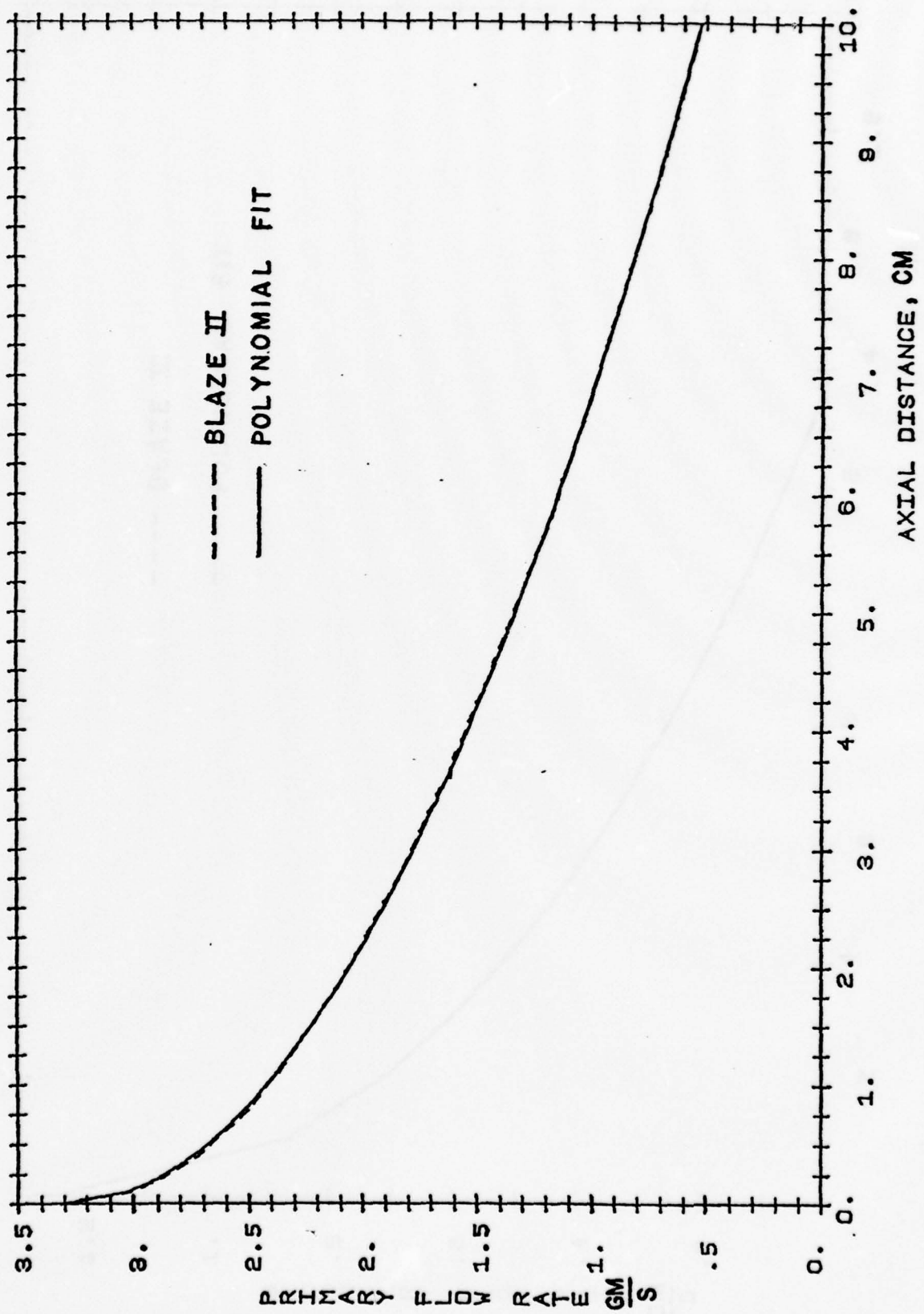Figure 7. Aerospace laser velocity profile.

Figure 8. Aerospace laser mass flow rate remaining in the primary stream ($\dot{m}_p$) profile.
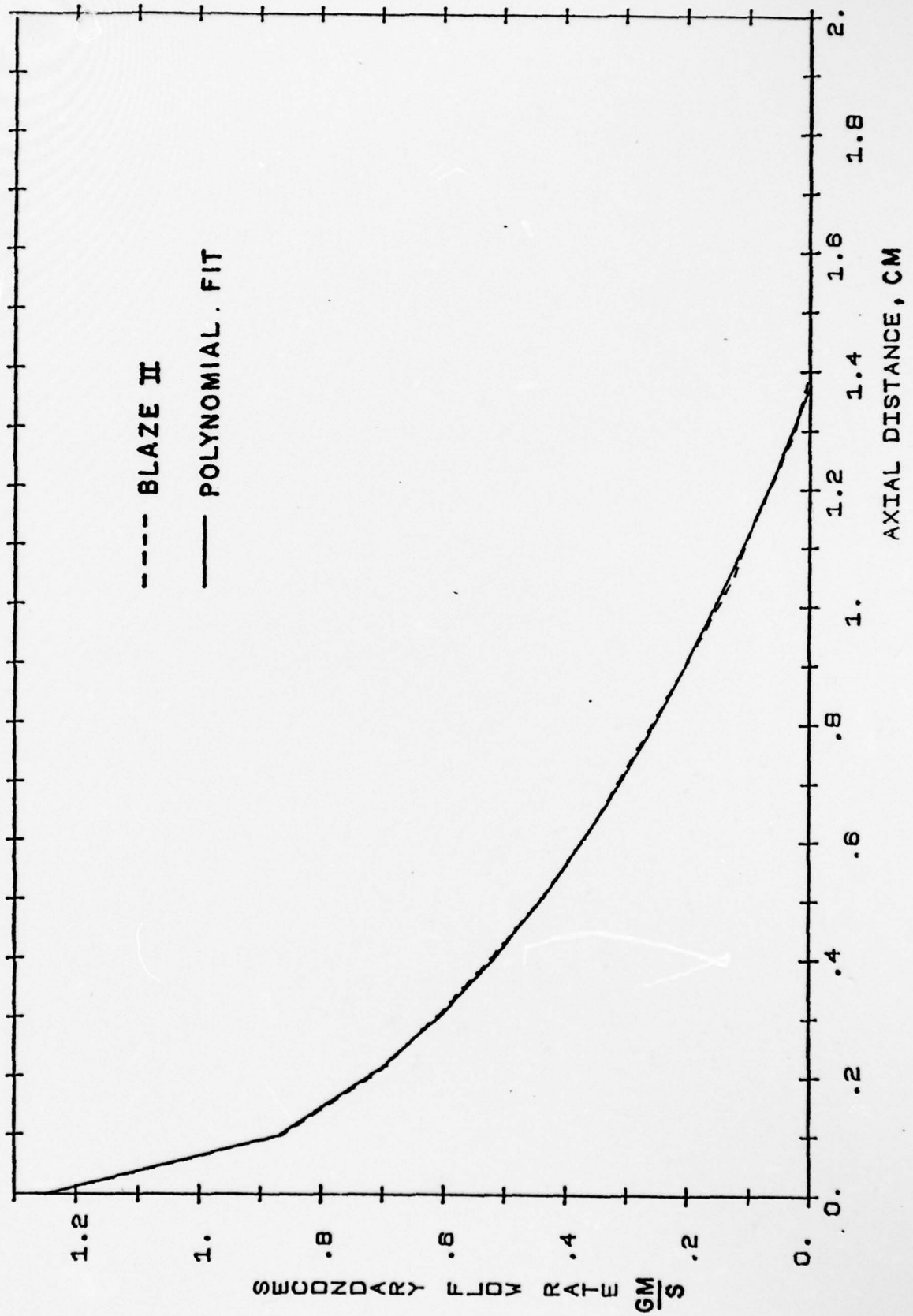
Figure 9. Aerospace laser mass flow rate remaining in the secondary stream ($\dot{m}_s$) profile.
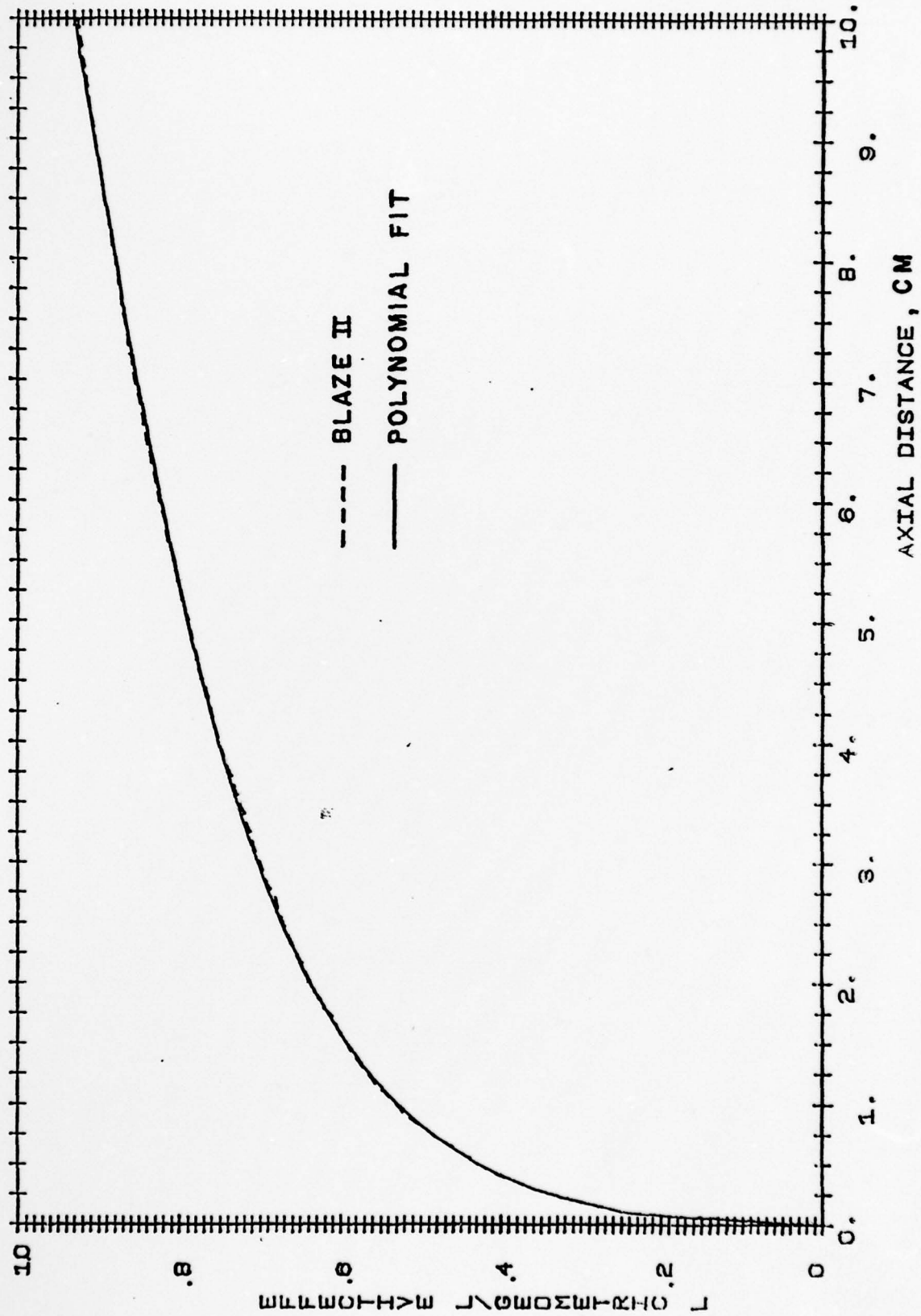
Figure 10. Aerospace laser effective length of the active media divided by the geometric length of the flow channel in the lasing direction as a function of x.
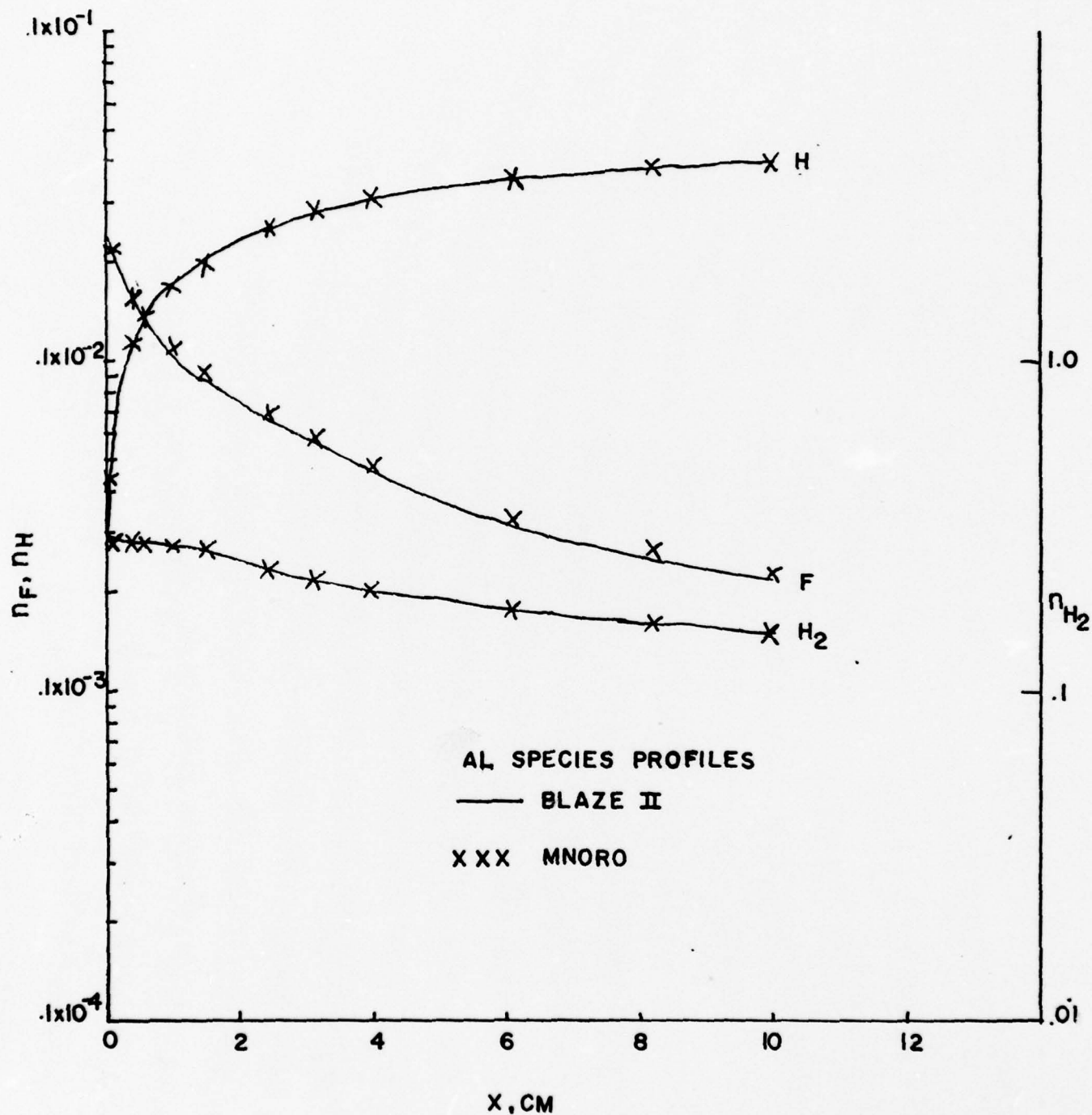
Figure 11. Comparison of the Blaze II and MNORO F, H, and H_2 profiles for the Aerospace laser (AL).

excellent agreement with the Blaze II H, F and H_2 profiles is obtained
regardless of whether lasing on $3 \rightarrow 2$ is simulated by setting $kp^2 = kp^2 + kp^3$
or whether HF(3) is pumped and allowed to collisionally deactivate. This
agreement is independent of whether the model is run in the rotational
equilibrium or the rotational nonequilibrium mode.

The Blaze II and MNORO HF(v) (v = 0, 1, 2, 3) profiles are shown for
the rotational equilibrium case in Fig. 12 and for the rotational nonequi-
librium case in Fig. 13. Since Blaze II has 14% of the total power in the
$3 \rightarrow 2$ band, we see that the best agreement with the HF(v) profiles occurs
when lasing on $3 \rightarrow 2$ is simulated by setting $kp^2 = kp^2 + kp^3$. When lasing on
$3 \rightarrow 2$ is not simulated, we see that multiquantum deactivation has a neg-
ligible effect on all the HF(v) profiles except for HF(3) which shows a
small effect. When lasing on $3 \rightarrow 2$ is not included, the rotational non-
equilibrium profiles tend to deviate more from the Blaze II profiles than
the equilibrium ones do. The fact that in the rotational nonequilibrium
case the lasing deactivation of HF(2) is slower than in the equilibrium
case results in more HF(2) and less HF(1). The significant effect of lasing
on $3 \rightarrow 2$ on the HF(3) profile is evident in Fig. 12 by comparing the Blaze
II, which includes lasing on $3 \rightarrow 2$, and the MNORO case for pumping HF(3) and
subsequent collisional deactivation.

The power spectral distributions are compared in the equilibrium, Fig. 14,
and the nonequilibrium, Fig. 15, cases. As can be seen, lasing on $3 \rightarrow 2$ and
the different types of collisional deactivation have only a small effect on
the $2 \rightarrow 1$ power spectral distribution.

From Table II, it is seen that when lasing on $3 \rightarrow 2$ is simulated in
MNORO, the power agrees very well with the Blaze II power. Thus, the MNORO
model gives very good agreement with the Blaze II species profiles, power
and power spectral distribution.

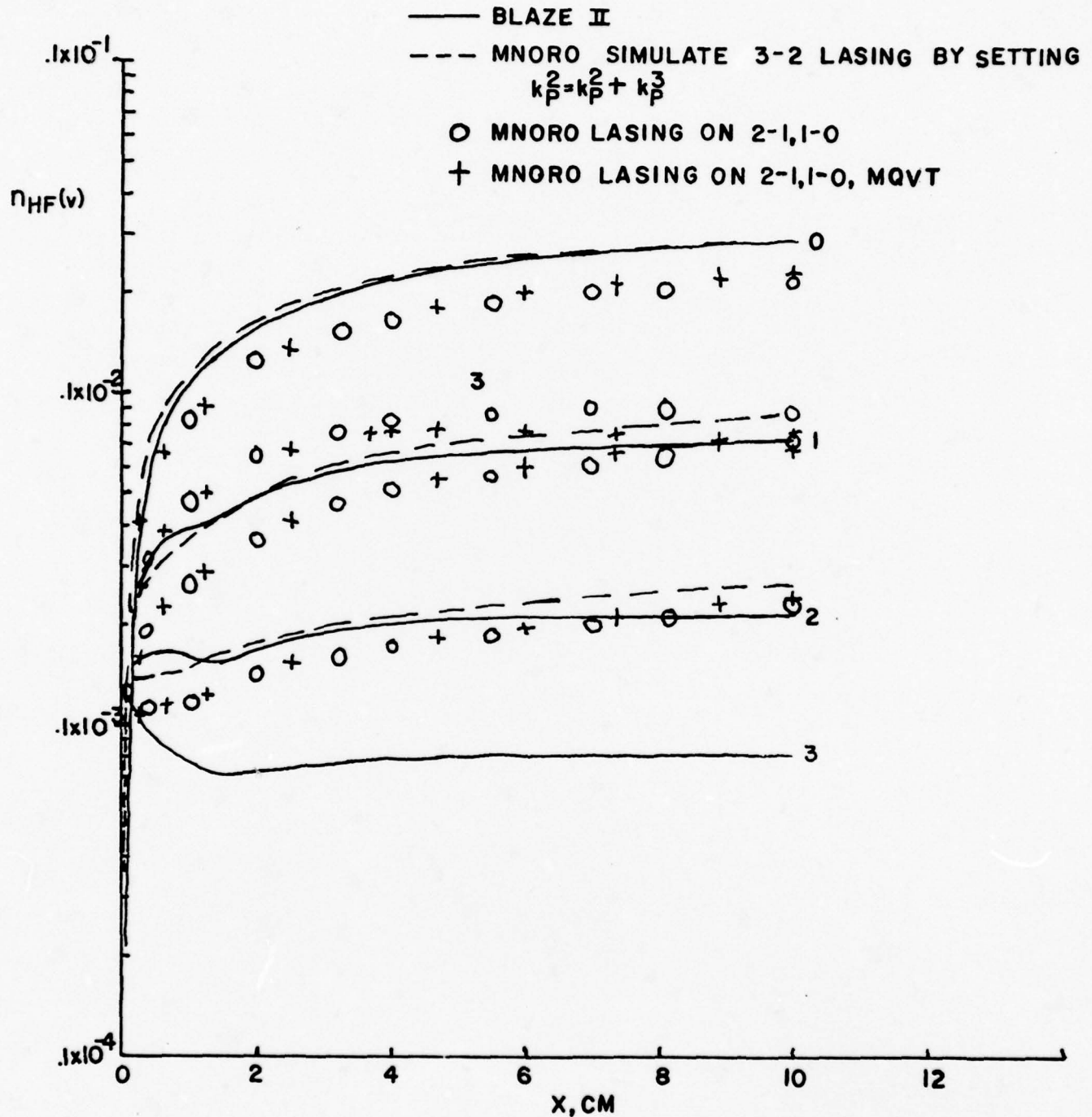Figure 12. Comparison of the Blaze II and MNORO HF(v) profiles for the Aerospace laser (AL).

AL SPECIES PROFILES

——— BLAZE II

×   MNORO SIMULATE 3-2 LASING BY SETTING
$k_P^2 = k_P^2 + k_P^3$

○   MNORO LASING ON 2-1,1-0

△   MNORO LASING ON 2-1,1-0,MQVT

MNORO CASES ARE ROTATIONAL NONEQUILIBRIUM
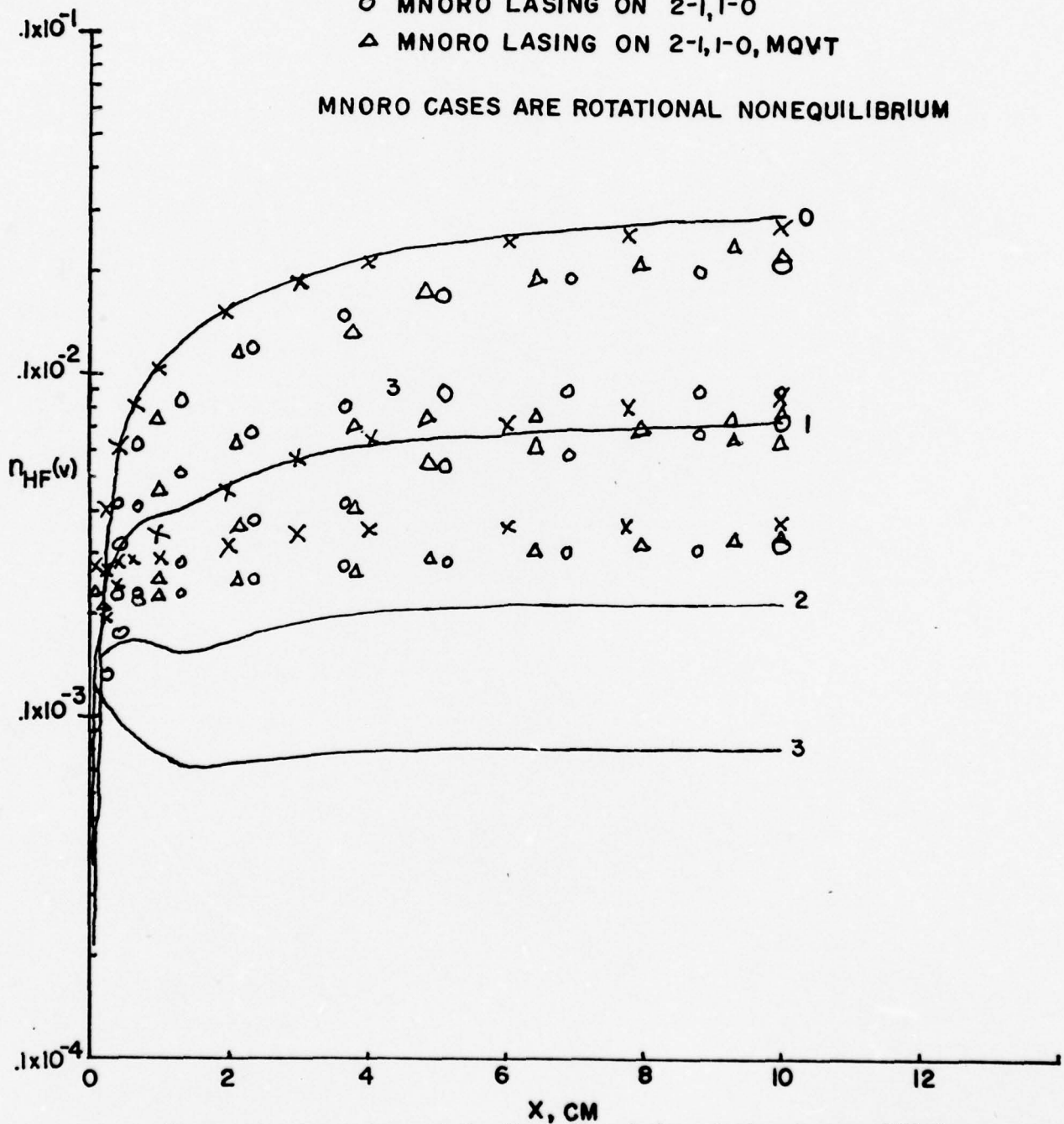
Figure 13.   Comparison of the Blaze II and the rotational nonequilibrium
MNORO HF(v) profiles for the Aerospace laser (AL).

AL POWER SPECTRAL DISTRIBUTION

ROTATIONAL EQUILIBRIUM

MNORO LASING ON 3-2 SIMULATED
BY $k_P^2 = k_P^2 + k_P^3$ $P_2 = 529$ W

MNORO LASING ON 2-1,1-0 $P_2 = 384$ W

MNORO LASING ON 2-1,1-0,MQVT $P_2 = 375$ W

BLAZE II LASING ON 3-2,2-1,1-0 $P_2 = 515$ W

41
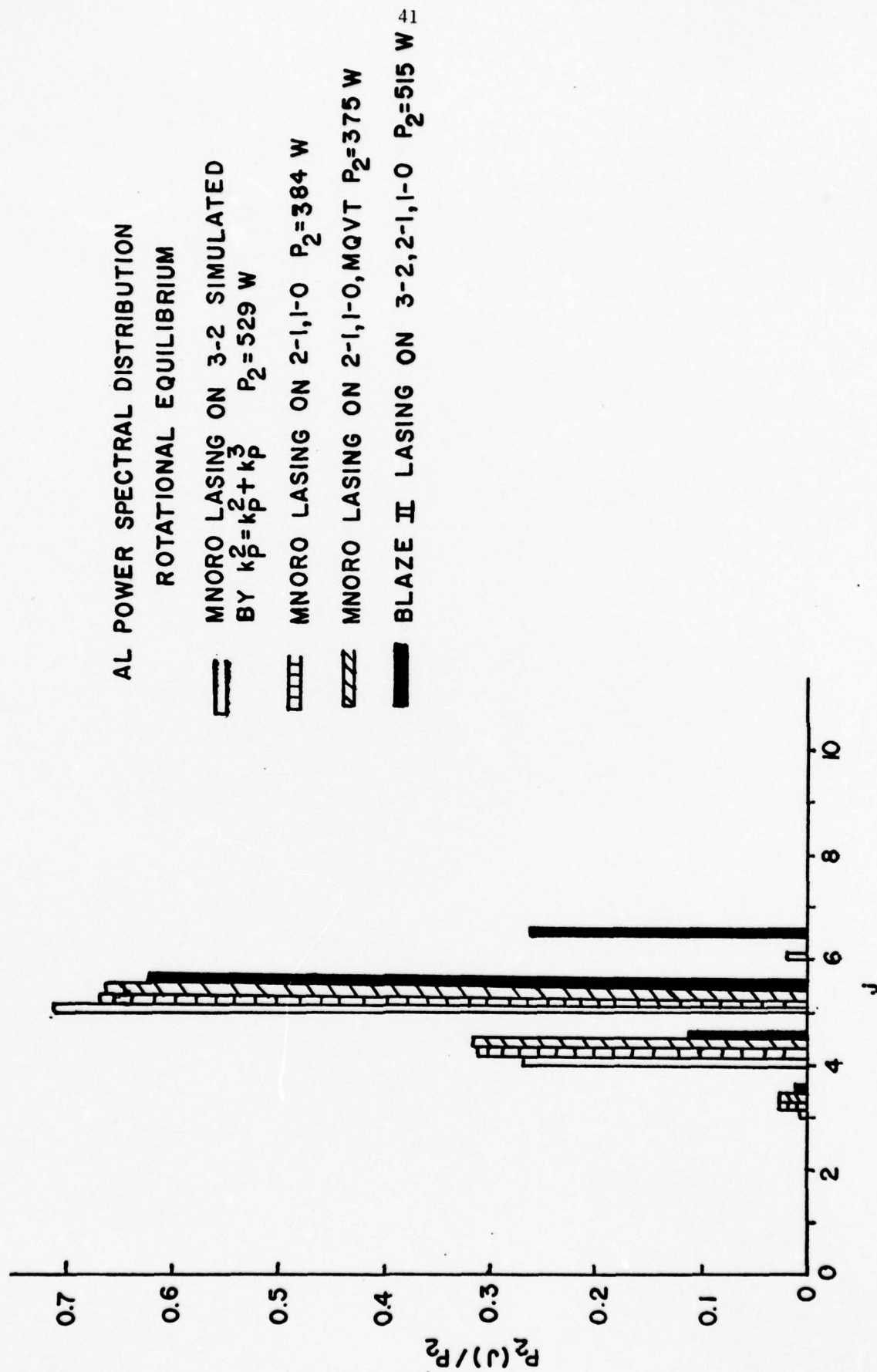
Figure 14. Comparison of the Blaze II and MNORO power spectral distributions for the Aerospace laser (AL).

42
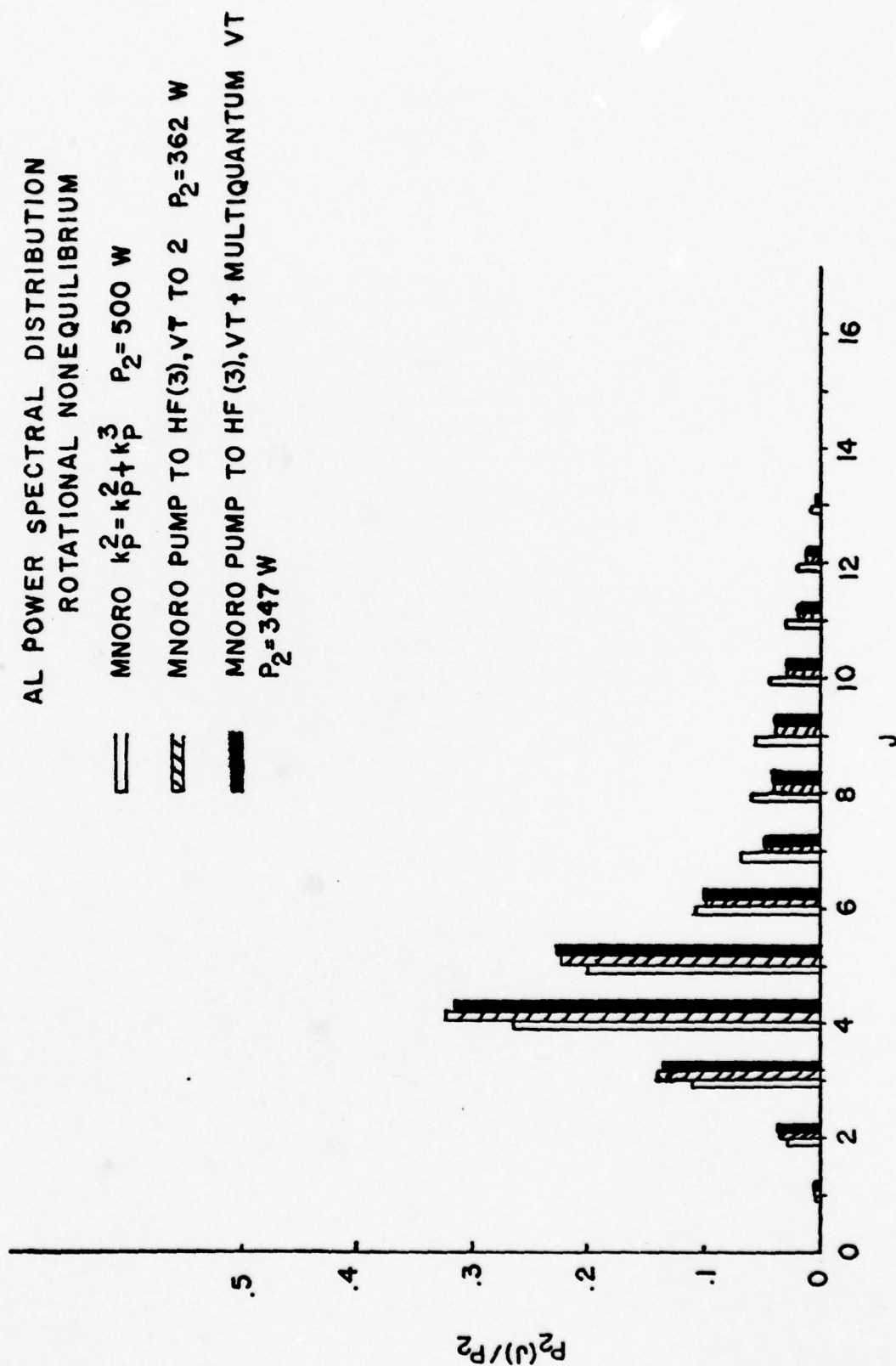
Figure 15. MNORO rotational nonequilibrium power spectral distributions for the Aerospace laser (AL).

43

MODEL	P_{10}	P_{21}	P_{32}
BLAZE II	485	515	162
MNORO ROTATIONAL EQUILIBRIUM			
Simulate 3-2 Lasing		529	
Lasing on 2-1, 1-0		384	
Lasing on 2-1, 1-0, MQVT		375	
MNORO ROTATIONAL NONEQUILIBRIUM			
Simulate 3-2 Lasing		500	
Lasing on 2-1, 1-0		362	
Lasing on 2-1, 1-0, MQVT		347	

Table II. Comparison of BLAZE II AND MNORO $2 \rightarrow 1$ Powers
for the Aerospace Laser.

Several other effects are evident in Table II. First, when mixing is present, the rotational nonequilibrium power is only about 6% less than the rotational equilibrium power rather than the 20% difference[1] obtained in a premixed case. Second, lasing on 3 → 2 has a significant effect on the 2 → 1 power. When 14% of the total power is in the 3 → 2 band, the 2 → 1 power increases 38% in both the equilibrium and the nonequilibrium cases. This suggests that it might be worthwhile to promote 3 → 2 lasing in order to enhance the 2 → 1 power. On the other hand, it points out the danger of adjusting parameters in a model to produce agreement with total power if the model predicts lasing on 3 → 2 when it is not observed experimentally. These results suggest that there may be a problem with the kinetic model. We will see this same effect in the CL XI case, but even more pronounced there, since Blaze II predicts lasing on the upper bands as well as 3 → 2, none of which is observed experimentally.

3.2 THE BELL AEROSPACE TEXTRON CL XI EXPERIMENT

Bell Aerospace Textron has performed a series of diagnostic experiments with the CL XI nozzle[14]. The CL XI (15,30) HF lasing lines experiment was chosen for initial baselining of the present model. In this experiment, the power spectral distribution and the intensity distribution on each line were measured. The intensity distributions were measured with cylindrical mirrors oriented with the axis of the cylinder parallel to the x axis (flow direction). Thus, a Fabry-Perot model of the cavity should provide a good representation of this experiment.

The primary flow contained F, F_2, He, N_2, CF_4 and DF and the secondary flow contained H_2 and He. The N_2, CF_4 and DF were treated as inert species which were represented by Argon in the present simplified model. To preserve numbers of particles, the total molar flow rate of these species was

replaced by the same molar flow rate of Argon. The experimental power spectral and intensity distributions are shown in Figs. 16 and 17. As in the previous case, the emphasis to date has been on comparing the present MNORO model run in the equilibrium mode with the Blaze II results for the CL XI (15,30) case.

Several Blaze II runs were made for this study. The first one allowed all bands up to $8 \rightarrow 7$ to lase. The second case allowed only $3 \rightarrow 2$, $2 \rightarrow 1$ and $1 \rightarrow 0$ to lase. The last case allowed only $2 \rightarrow 1$ and $1 \rightarrow 0$, the bands observed experimentally, to lase.

The Blaze II calculations took the effect of the nozzle trip flow on the mixing into account by increasing the binary diffusion coefficient. This multiplier was established by comparison of lasing zone length and total power with experimental data for the case when all bands up to $8 \rightarrow 7$ could lase if conditions would allow it[15]. The results of these three runs are shown in Table III. The effect of the change in the vibrational bands which were allowed to lase on the fluid dynamic and species profiles is shown in Figs. 18-20. From these figures, it is seen that the hot reaction bands have a negligible effect on these profiles. Not allowing lasing to occur on $3 \rightarrow 2$ results in a 10% increase in the peak pressure and temperature and a negligible effect on the other profiles except for the HF(3) profile. Thus, one set of fluid profiles was used throughout this study. As in the preceeding case, the polynomials give an excellent representation of the fluid dynamic variables.

Figure 21 shows the effect of the bands which are allowed to lase on the $2 \rightarrow 1$ power spectral distribution. The hot reaction bands have a negligible influence on the $2 \rightarrow 1$ power spectral distribution. However,
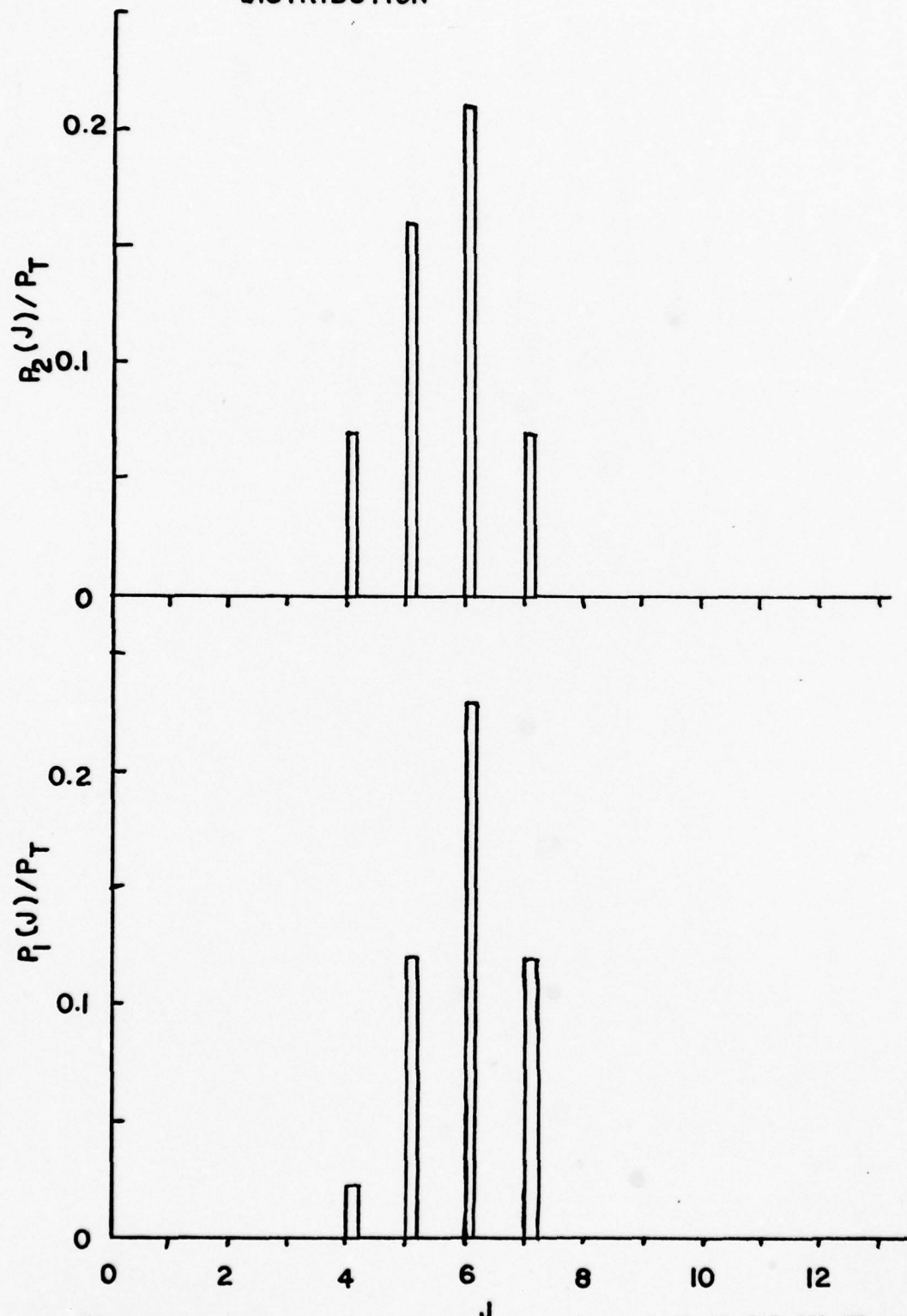
BELL AEROSPACE TEXTON

EXPERIMENTAL CL XI (15,30) HF POWER SPECTRAL

DISTRIBUTION

Figure 16. Bell Aerospace Textron experimental CL XI (15,30) HF power spectral distribution.

BELL AEROSPACE TEXTRON

CL XI (15,30) EXPERIMENTAL HF POWER SPECTRAL
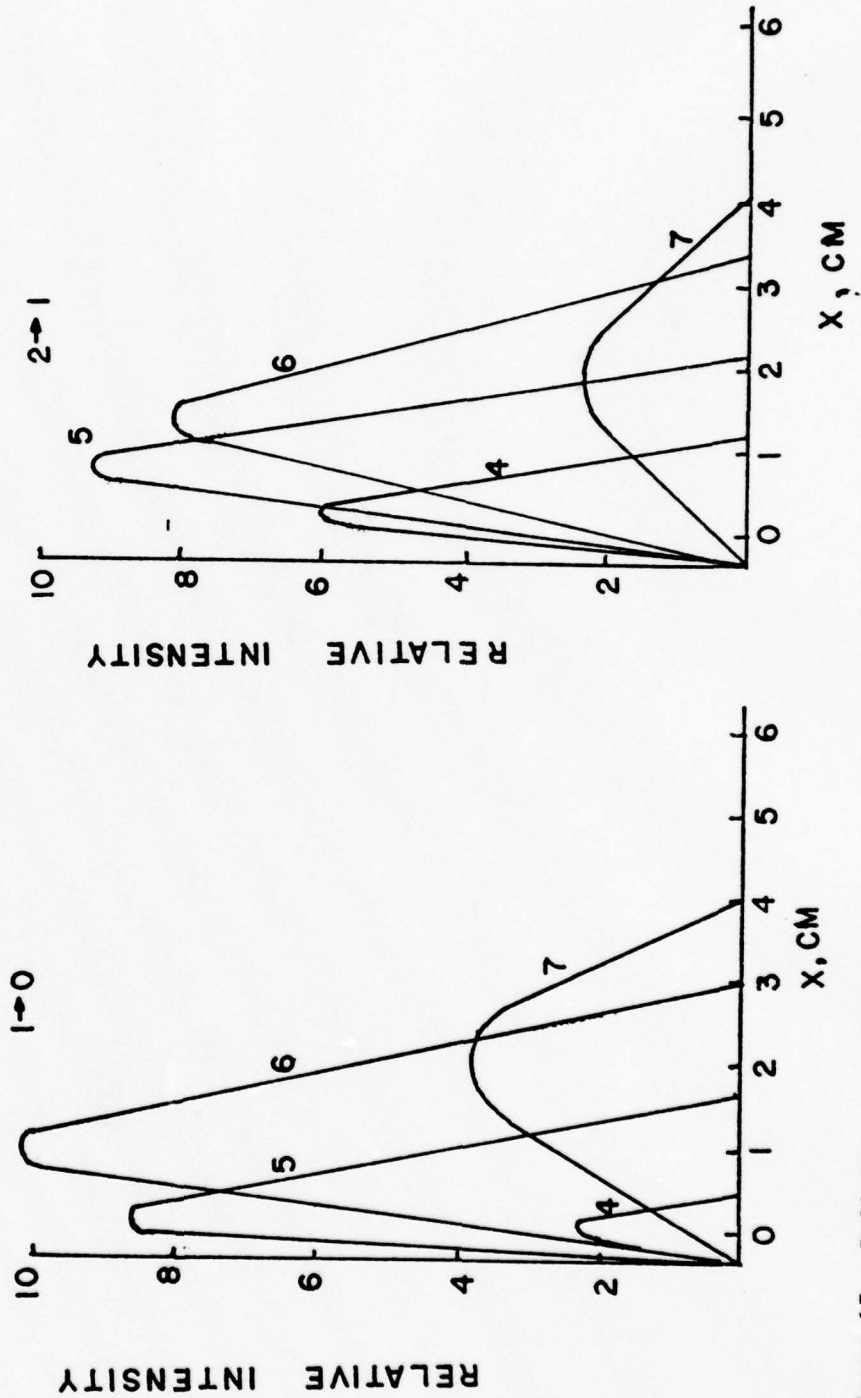
DISTRIBUTION

Figure 17. Bell Aerospace Textron experimental CL XI (15,30) HF intensity distributions.

Bands Lasing	Lasing Zone Length	Total Power	$\dfrac{P_{10}}{P_T}$ $\left[\dfrac{P_{10}}{P_{T\ \text{All}}}\text{Bands}\right]$	$\dfrac{P_{21}}{P_T}$ $\left[\dfrac{P_{21}}{P_{T\ \text{All}}}\text{Bands}\right]$	$\dfrac{P_{32}}{P_T}$ $\left[\dfrac{P_{32}}{P_{T\ \text{All}}}\text{Bands}\right]$	$\dfrac{P_{43}}{P_T}$	$\dfrac{P_{54}}{P_T}$	$\dfrac{P_{65}}{P_T}$	$\dfrac{P_{76}}{P_T}$
All bands	1	1	.417	.422	.113	.0019	.025	.0198	0
32, 21, 10	1	.956	.436 (.417)	.443 (.423)	.122 (.117)				
21, 10	.909	.740	.518 (.384)	.482 (.356)					

Table III. BLAZE II CL XI (15,30) Results When Various Bands are Allowed to Lase.
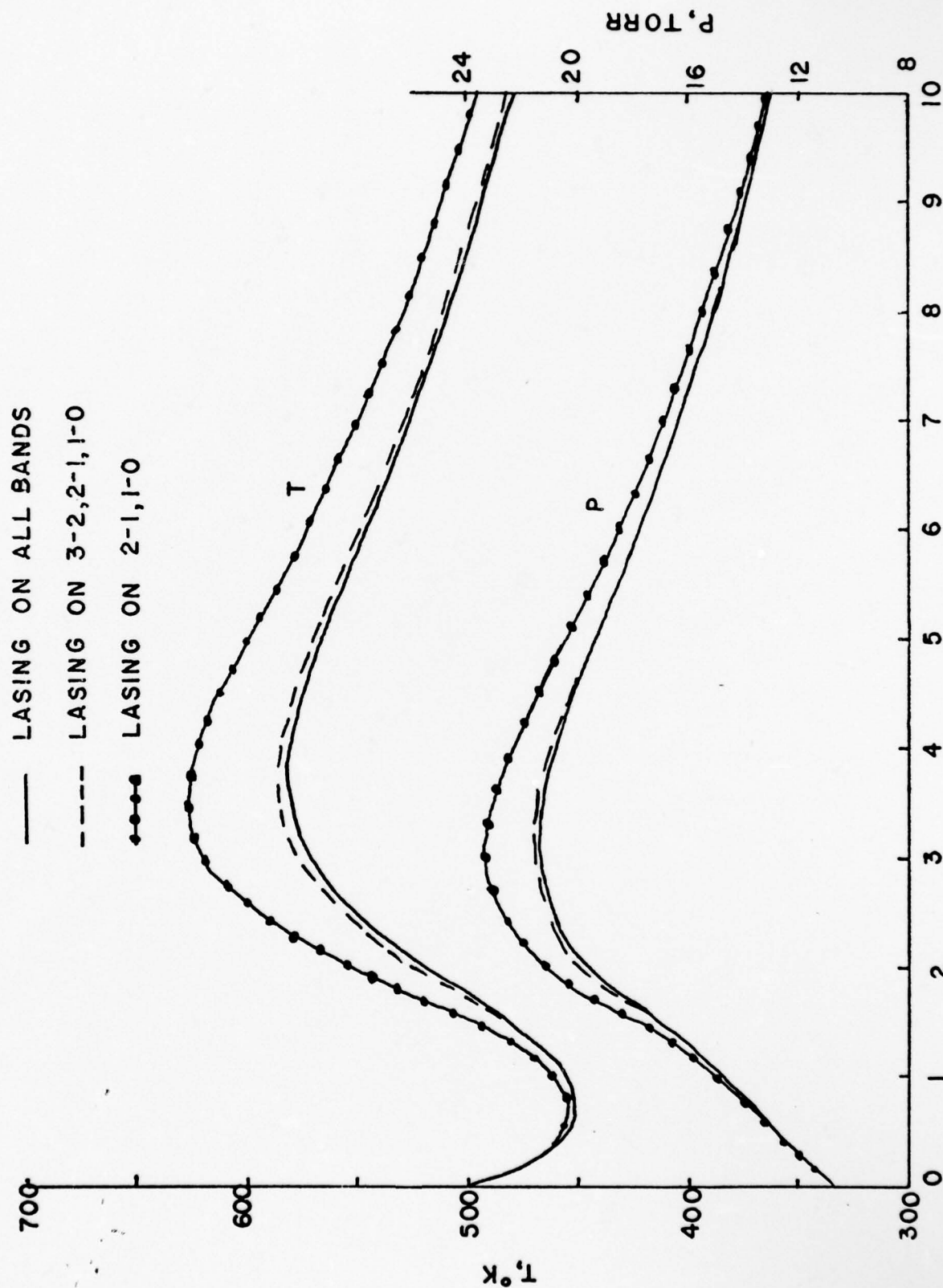
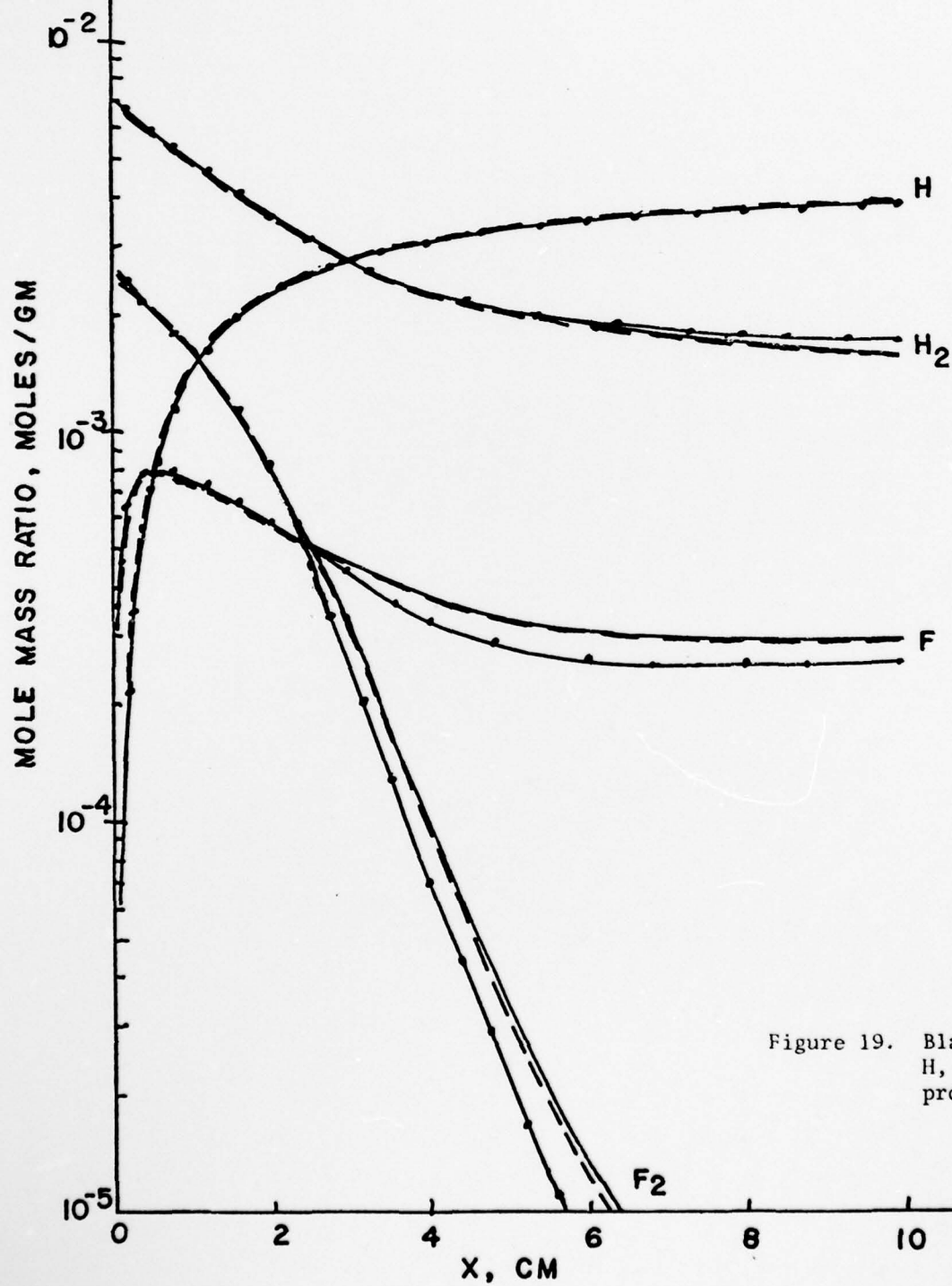Figure 18. Blaze II CL XI (15,30) temperature and pressure profiles.

Figure 19. Blaze II CL X1 (15,30)
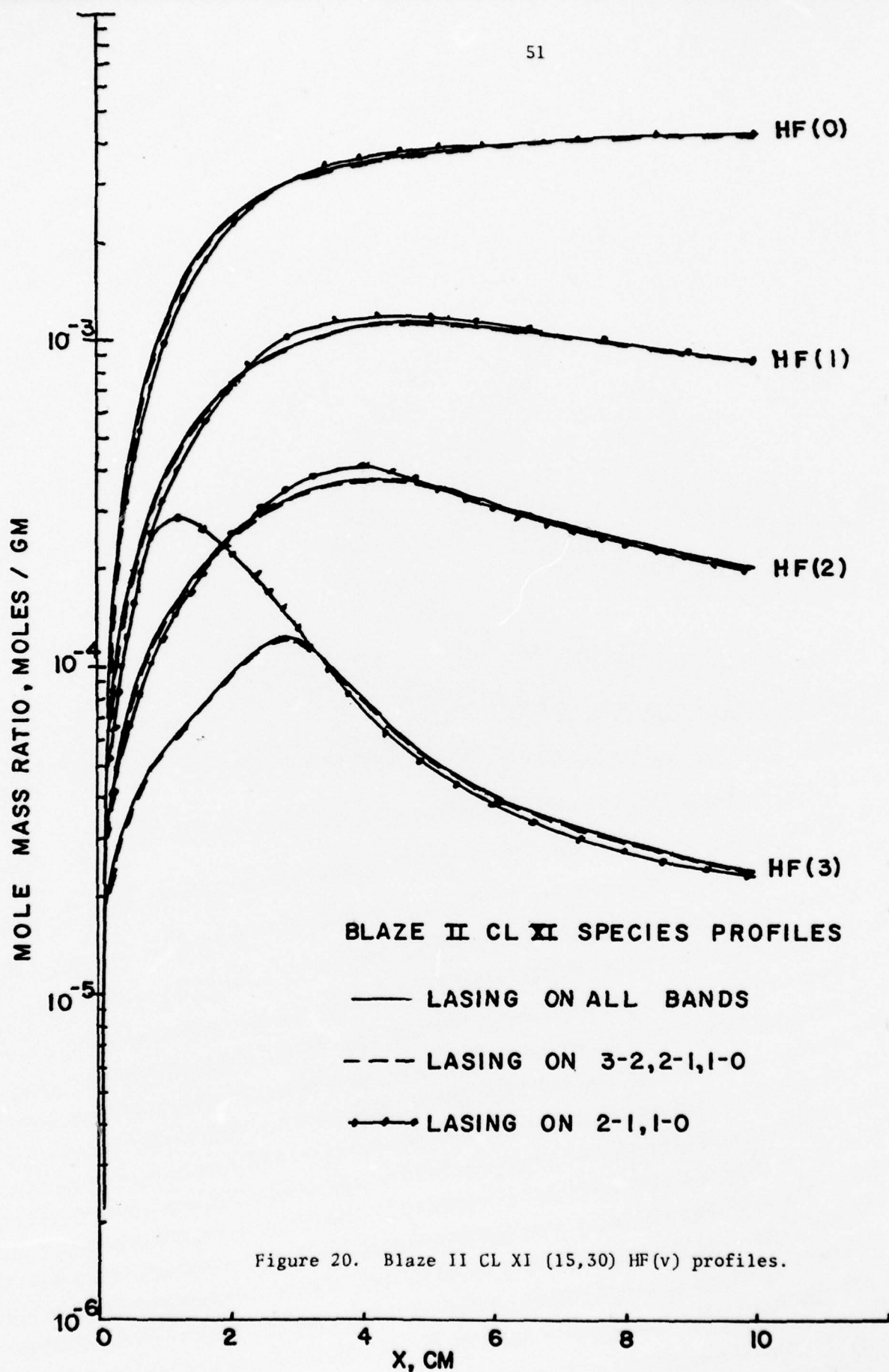H, F, H_2 and F_2
profiles.

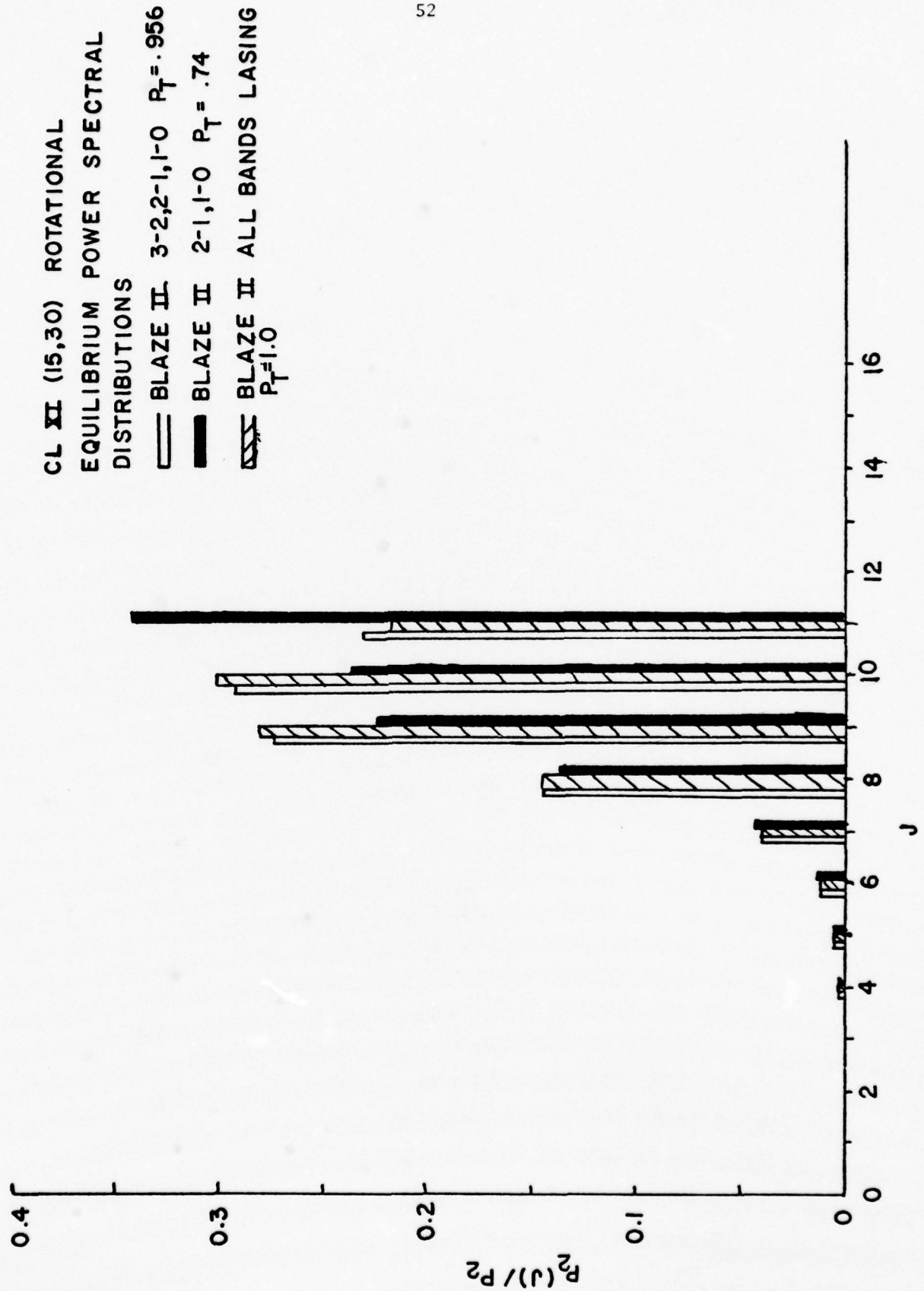Figure 20. Blaze II CL XI (15,30) HF(v) profiles.

Figure 21. Blaze II CL XI (15,30) power spectral distributions.

lasing on $3 \rightarrow 2$ has a significant effect not only on the total power in the $2 \rightarrow 1$ band, Table III, but also on the $2 \rightarrow 1$ power spectral distribution.

The MNORO results excluding the hot reaction are compared to the Blaze II species profiles in Figs. 22 and 23 for the cases of no lasing on $3 \rightarrow 2$ and lasing on $3 \rightarrow 2$ simulated by setting $kp^2 = kp^2 + kp^3$. The corresponding power spectral distributions and $2 \rightarrow 1$ powers are compared in Fig. 24. From these figures we see that even though the P_{21}'s agree within 10% and the power spectral distributions are quite similar, there are considerable differences in all the species profiles except for the H atom profile.

The corresponding results when the hot reaction is included by pumping only to HF(3) and when multiquantum VT deactivation by HF, F and H are included are shown in Figs. 25-27. Because of the relatively high temperature $(T_{MAX} = 585°K)$ and the F atom wall recombination which results in a significant amount of F_2, the hot pumping reaction must be included in the kinetic model to duplicate the Blaze II F, H and F_2 profiles, Fig. 25. As might be expected, the multiquantum deactivation has a negligible effect on the F, H, F_2 and H_2 species profiles. From Fig. 26, it is seen that both the hot reaction and multiquantum deactivation are required to obtain good agreement with the Blaze II HF(v) profiles. The agreement is not as good for HF(3) because the hot reaction is pumping completely to HF(3) rather than to the upper levels with collisional cascade to HF(3). When hot reaction pumping to HF(3) and HF(4), where $k_{PH}^4 = \sum_{v=4}^{6} k_{PH}^v$, is included, there is no change in the HF(v) species profiles for $v = 0, 1, 2$ and only a slight improvement in HF(3). To obtain better agreement with HF(3) would require including at least up to HF(5) because, based on the magnitude of the rate constants involved, there is a bottle neck at HF(4) which would result in decreased HF(3). Since the effect on the $2 \rightarrow 1$ power and power spectral distribution

CL XI SPECIES PROFILES

--- BLAZE II LASING ON 3-2,2-1,1-0

•–•–• BLAZE II LASING ON 2-1,1-0

✕ MNORO LASING ON 2-1,1-0

○ MNORO $k_P^2 = k_P^2 + k_P^3$ TO SIMULATE LASING ON 3-2
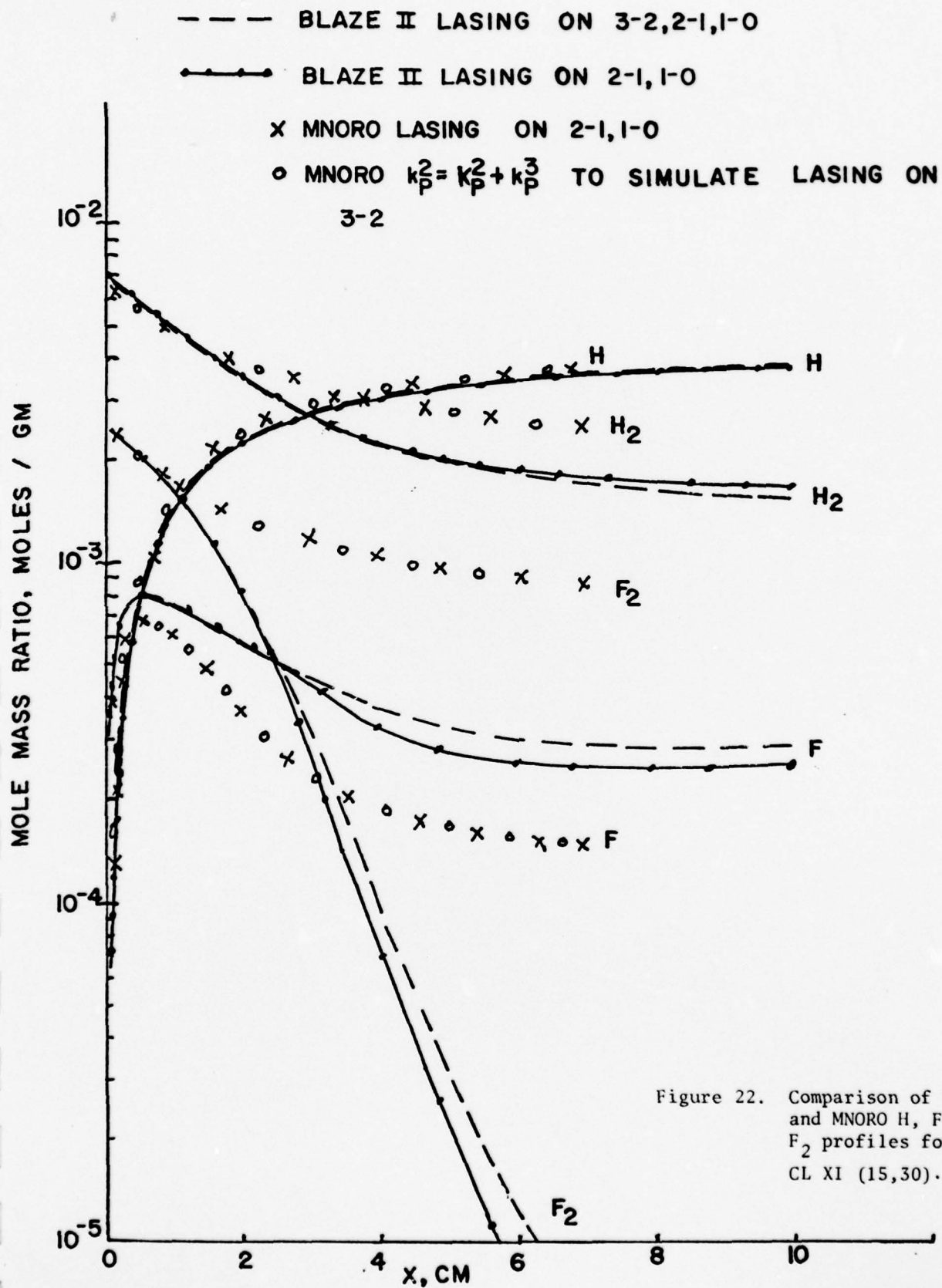
Figure 22. Comparison of Blaze II and MNORO H, F, H_2 and F_2 profiles for the CL XI (15,30).
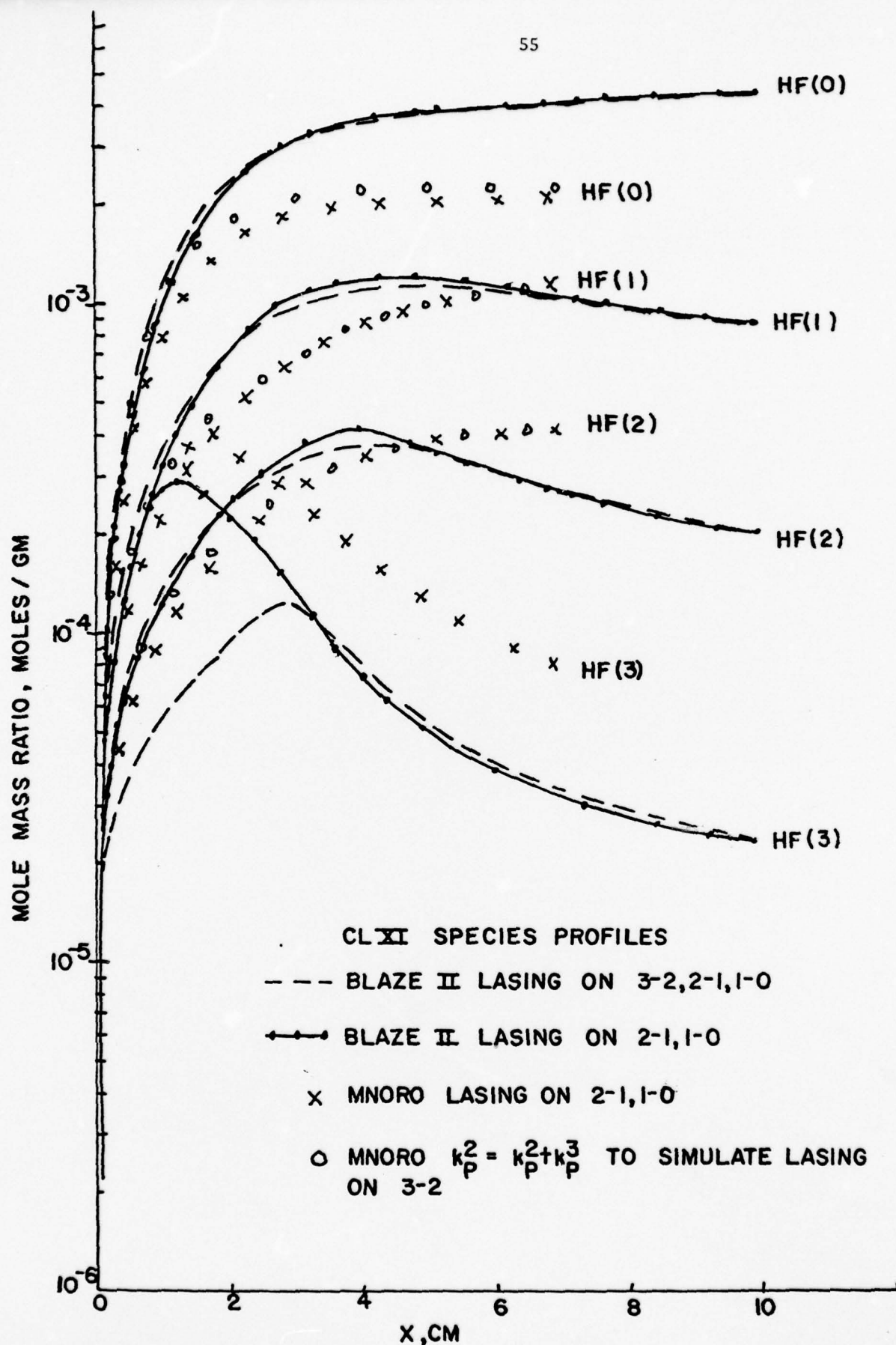
Figure 23. Comparison of Blaze II and MNORO HF(v) profiles for the CL X1 (15,30).

Figure 24. Comparison of Blaze II and MNORO power spectral distributions for CL Xl (15,30).

BLAZE II CL XI SPECIES PROFILES

•—•—• BLAZE II LASING 2-1, 1-0
× × × MNORO HOT REACTION AND MQVT
○ ○ ○ MNORO HOT REACTION, NO MQVT
△ △ △ MNORO NO HOT REACTION, NO MQVT
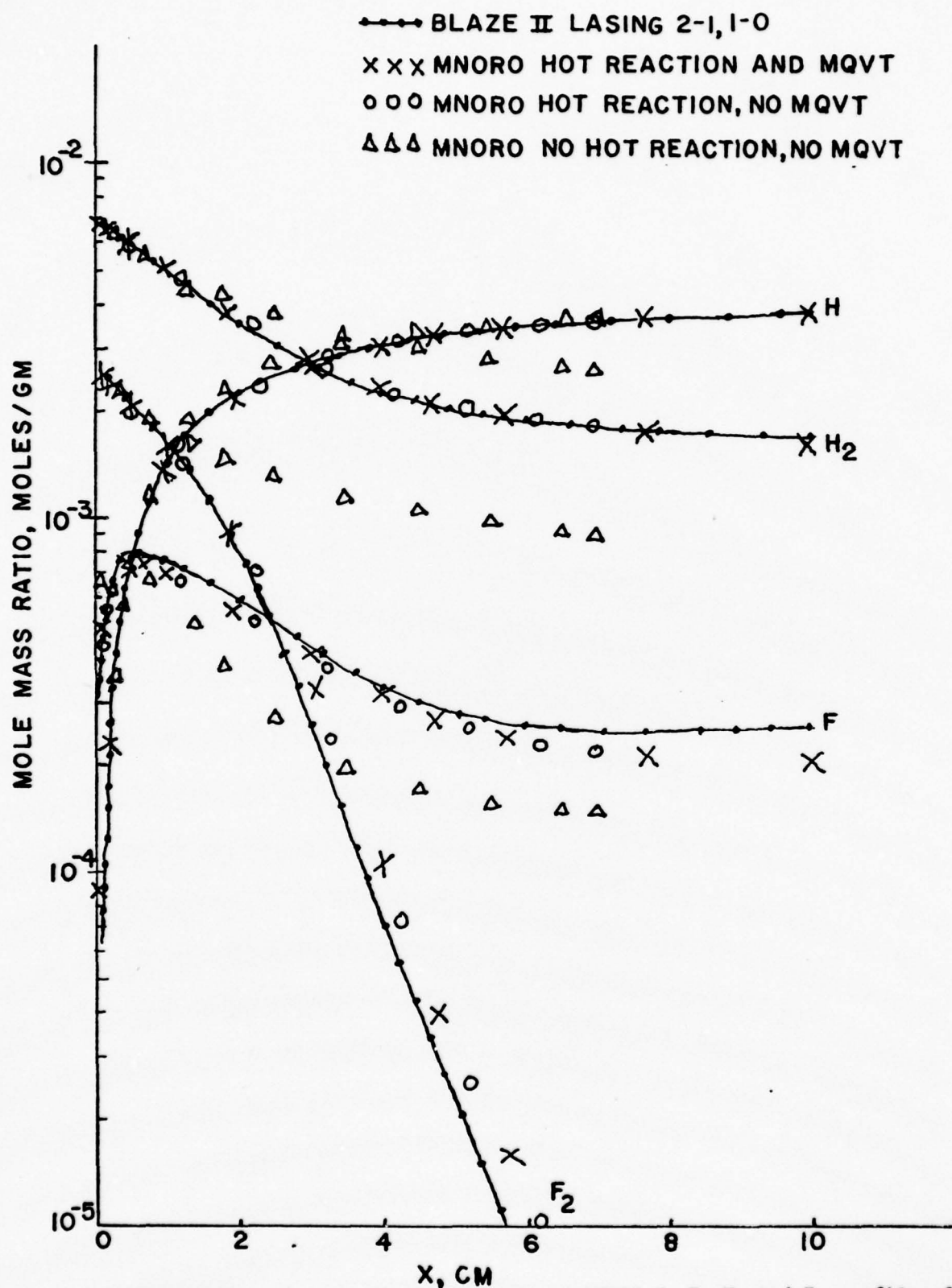
Figure 25. Comparison of Blaze II and MNORO H, F, H_2 and F_2 profiles for the
CL X1 (15,30) showing the effect of the hot reaction and multiquantum
VT deactivation (MQVT).
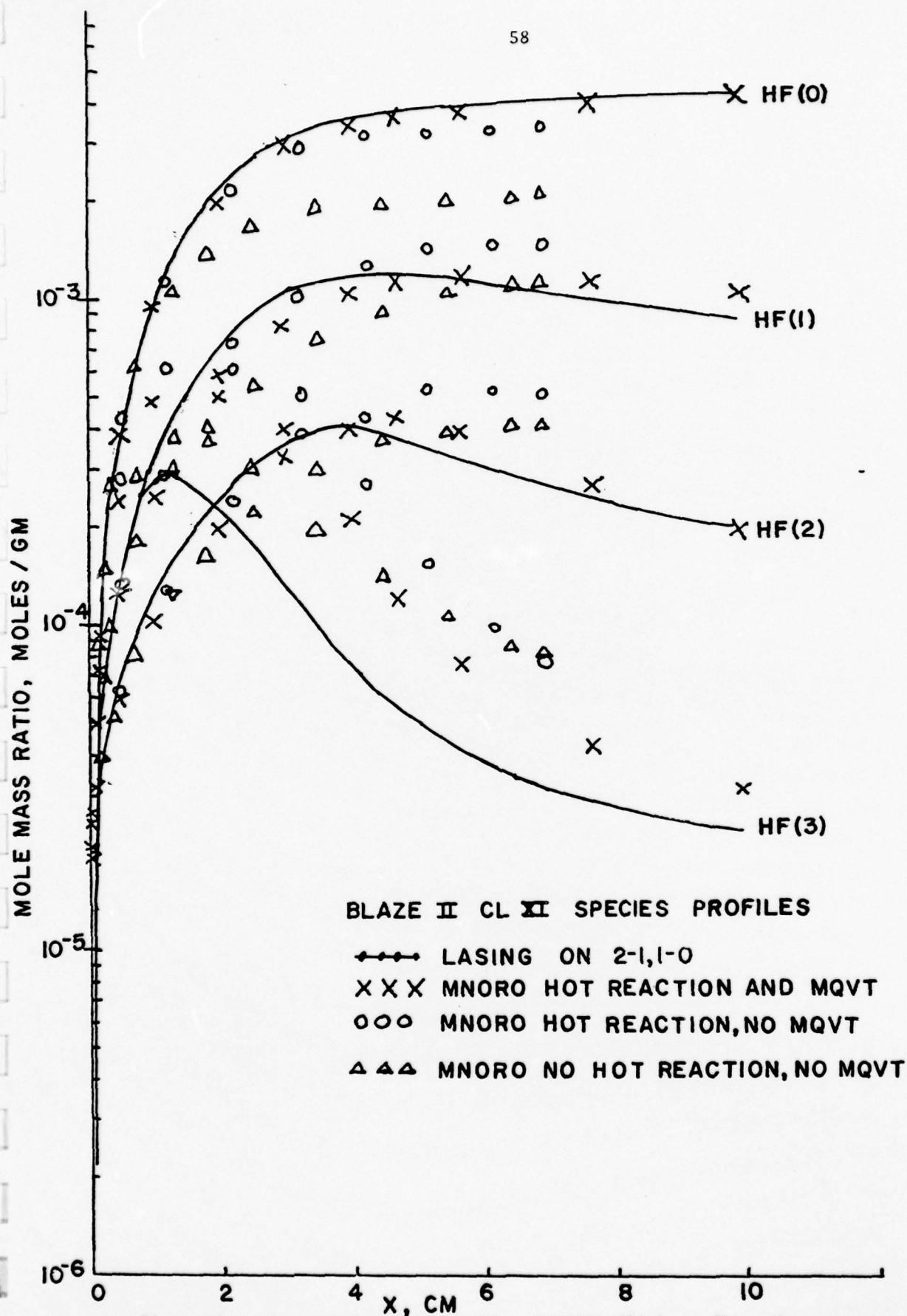
Figure 26. Comparison of Blaze II and MNORO HF(v) profiles for the CL X1 (15,30) showing the effect of the hot reaction and MQVT.

CL XI (15,30) ROTATIONAL
EQUILIBRIUM POWER SPECTRAL
DISTRIBUTIONS

▬ BLAZE II P_2=.84
▭ MNORO HOT REACTION AND MQVT P_2=.83
▭ MNORO HOT REACTION, NO MQVT P_2=1.07
▭ MNORO NO HOT REACTION, NO MQVT P_2=.75

0.4

0.3

0.2

0.1

0

$P_2(J) / P_2$

0   2   4   6   8   10   12   14

J

Figure 27. Comparison of the Blaze II and MNORO power spectral distributions for CL XI (15,30) showing the effect of the hot reaction and MQVT.

would be small, the additional complexity is not warranted. Thus, the final
model includes the effect of the hot reaction by allowing it to pump to
HF(3) only, i.e., $k_{PH}^3 = \sum_{v=3}^{6} k_{PH}^v$. The effect of the hot reaction and multi-
quantum deactivation on the rotational equilibrium power spectral distribu-
tion is shown in Fig. 27. Again it is seen that both of these reaction types
have a significant effect and hence must be included in the model. From runs
made with only the $2 \rightarrow 0$ multiquantum deactivation and with $2 \rightarrow 0$, $3 \rightarrow 1$ and
$3 \rightarrow 0$, the most important of these reactions is the $2 \rightarrow 0$ deactivation by a
factor of about two to one.

The rotational nonequilibrium species profiles when the hot reaction
pumps only to HF(3) and multiquantum deactivations are included are compared
to the Blaze II profiles in Fig. 28 and 29. As can be seen, the nonequili-
brium species profiles agree as well with the Blaze II species profiles as
the equilibrium ones do. However, it is seen from Fig. 30 that the nonequi-
librium power spectral distribution is considerably different than the
equilibrium power spectral distribution. The peak of the nonequilibrium PSD
at $J = 8$ is indicative of the relatively large T ($T_{max} = 585°K$); since the
experimental data peaks at $J = 6$, Blaze II may be overpredicting the tem-
perature.

Figures 31-36 give the rotational equilibrium and the rotational non-
equilibrium saturated gains and intensity distributions. The J-shifting is
evident in the gain and intensity distributions for the equilibrium case
whereas simultaneous lasing on many lines occurs in the nonequilibrium case.

From the Blaze II results, Table III, it is seen that the occurrence
of lasing on $3 \rightarrow 2$ results in a 21% increase in the power on $2 \rightarrow 1$; MNORO
indicates a 24% increase when lasing on $3 \rightarrow 2$ occurs. Since this is a sig-
nificant effect, as found in the previous case, it may be worthwhile
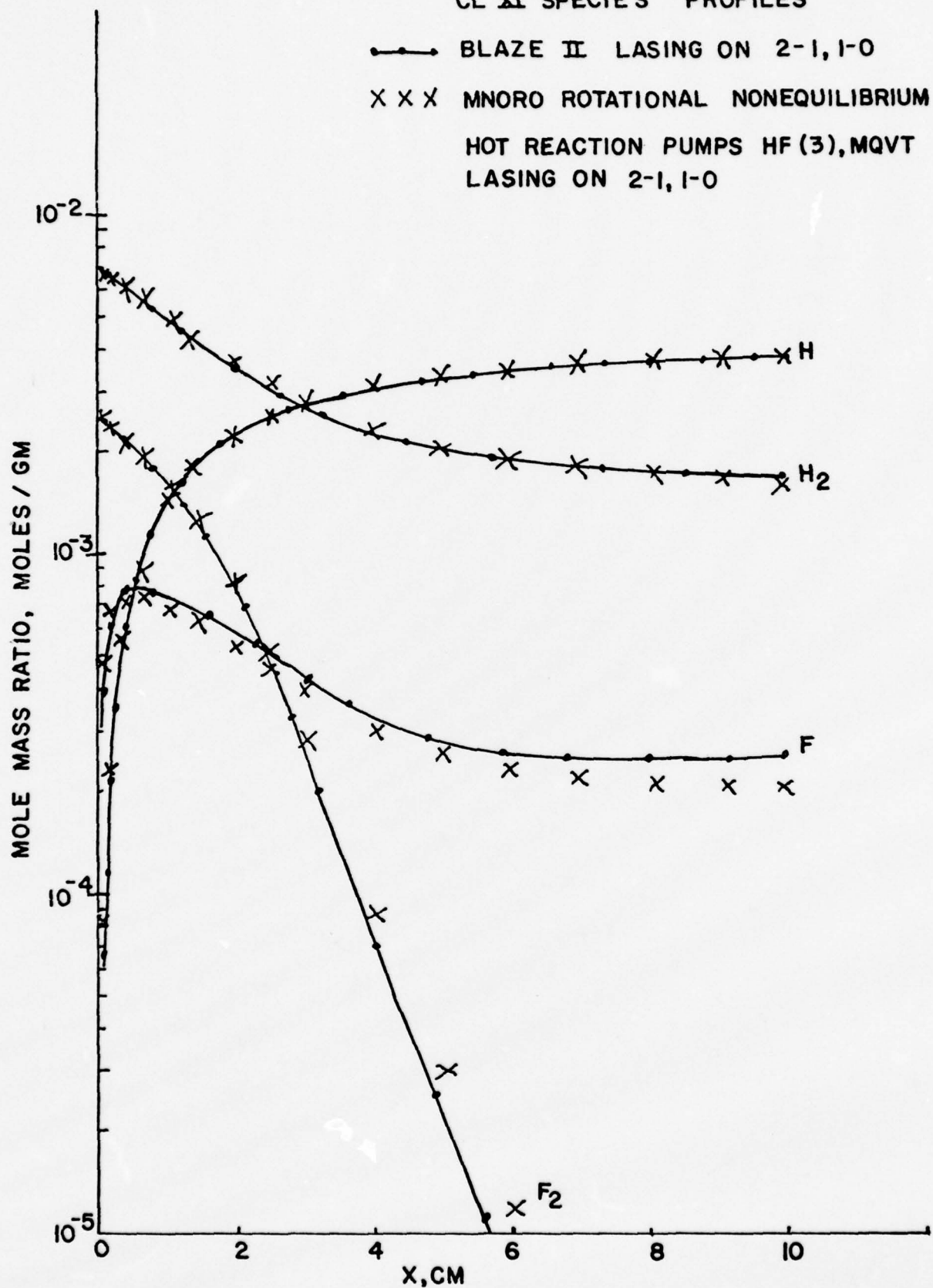
Figure 28. Comparison of Blaze II and rotational nonequilibrium MNORO H, F, H_2 and F_2 profiles for CL X1 (15,30).
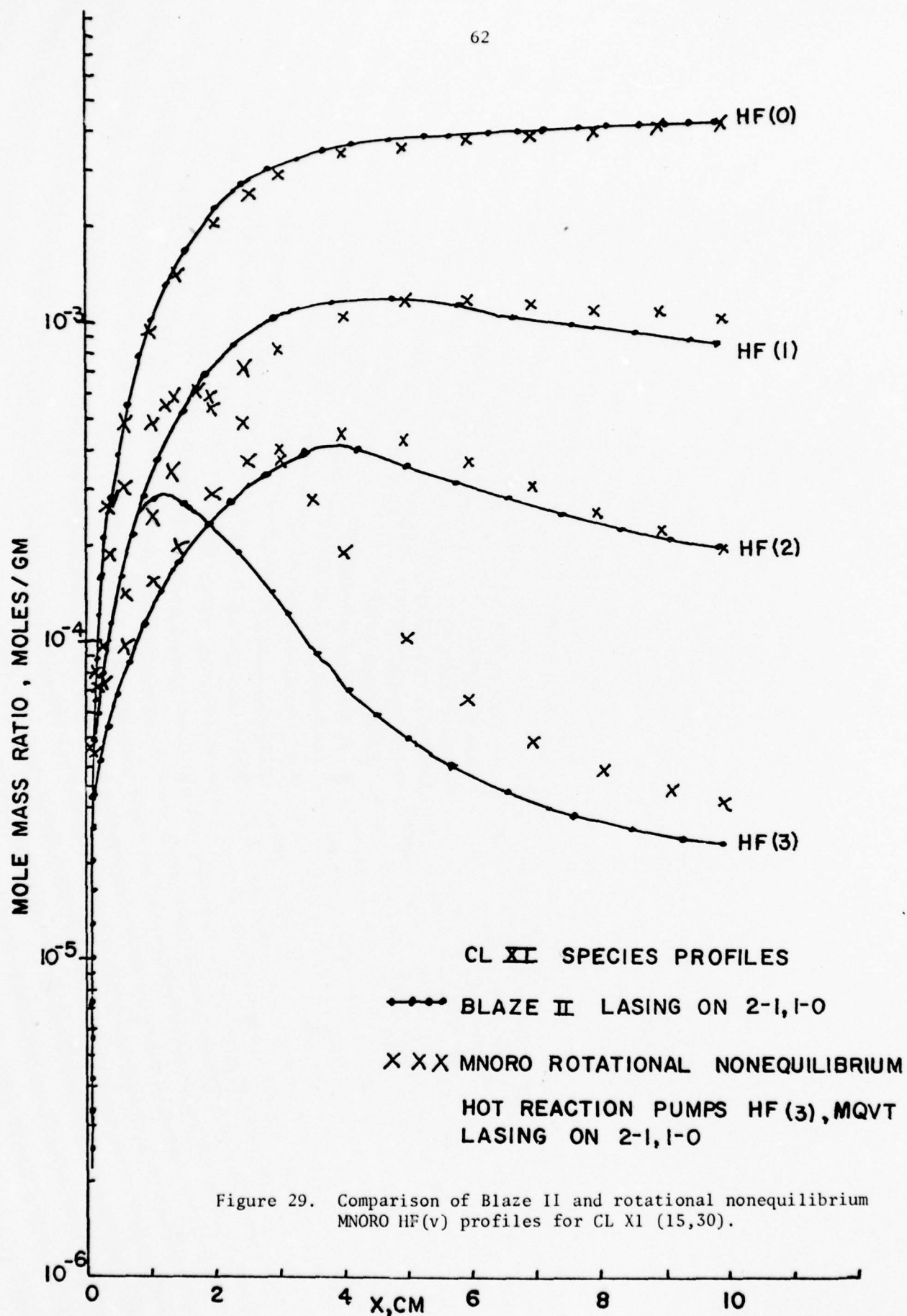
Figure 29. Comparison of Blaze II and rotational nonequilibrium MNORO HF(v) profiles for CL X1 (15,30).

CL XI POWER SPECTRAL DISTRIBUTION

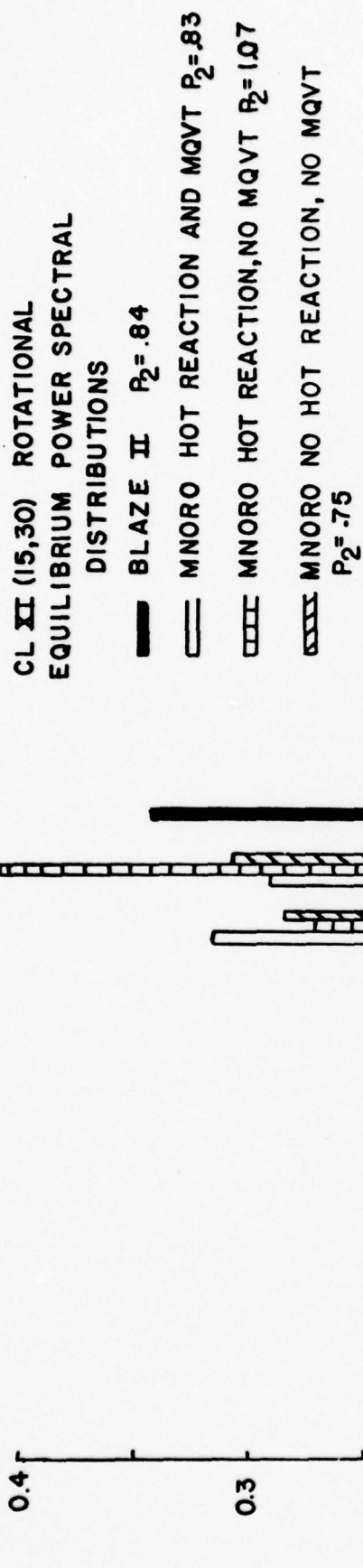MNORO RNE HOT REACTION PUMPS
HF (3), P_{21} = .79, MQVT

MNORO RE HOT REACTION PUMPS
HF (3), P_{21} = .83, MQVT

$P_2 (J)/P_2$

J

0.4   0.3   0.2   0.1   0

0   2   4   6   8   10   12   14   16
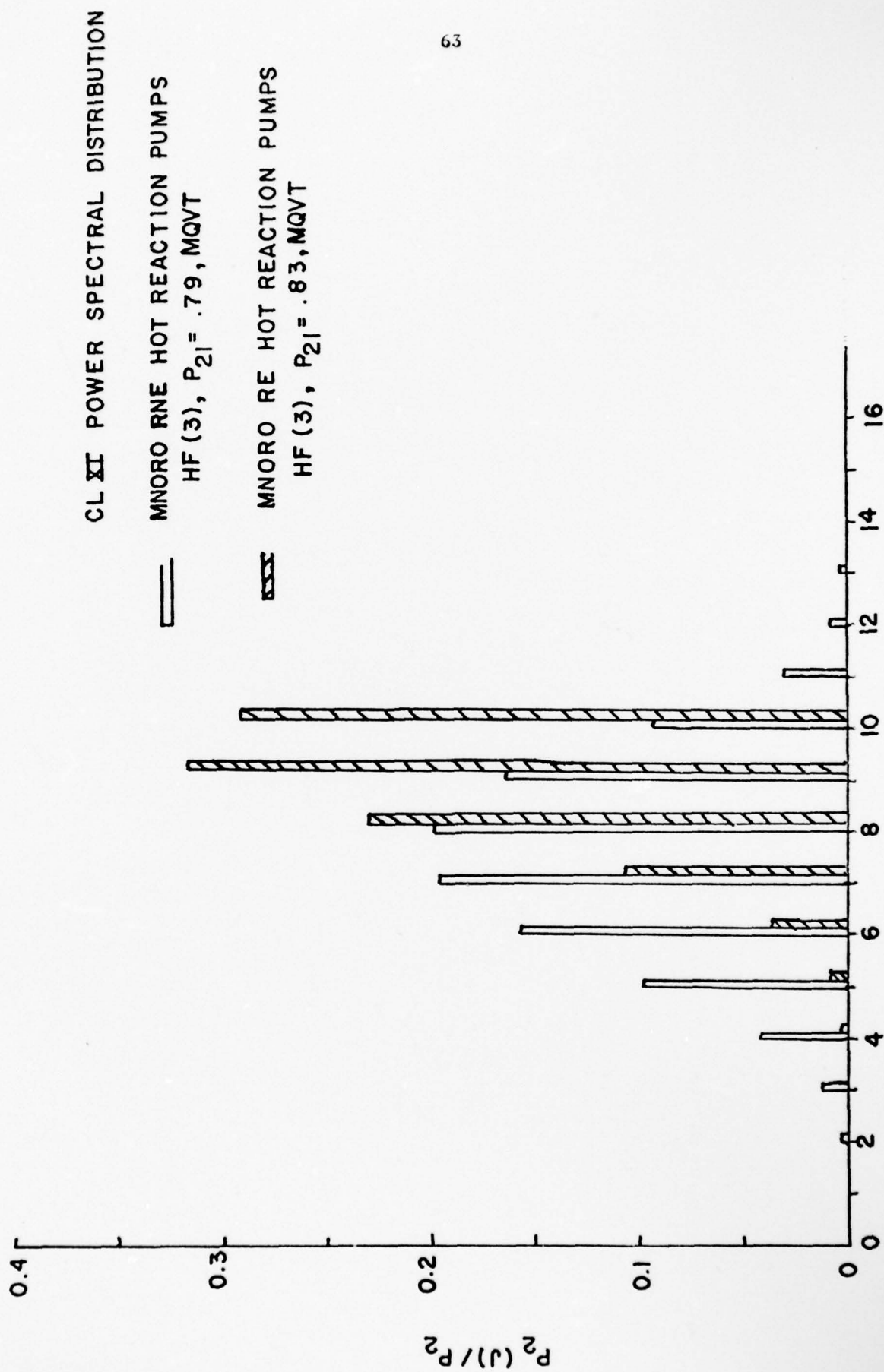
Figure 30.   Comparison of rotational equilibrium (RE) and rotational nonequilibrium (RNE)
MNORO power spectral distributions.

Figure 31. MNORO rotational equilibrium P branch gains for CL X1 (15,30).

2-I, P-BRANCH INTENSITIES

CL XI (I5,30) MNORO
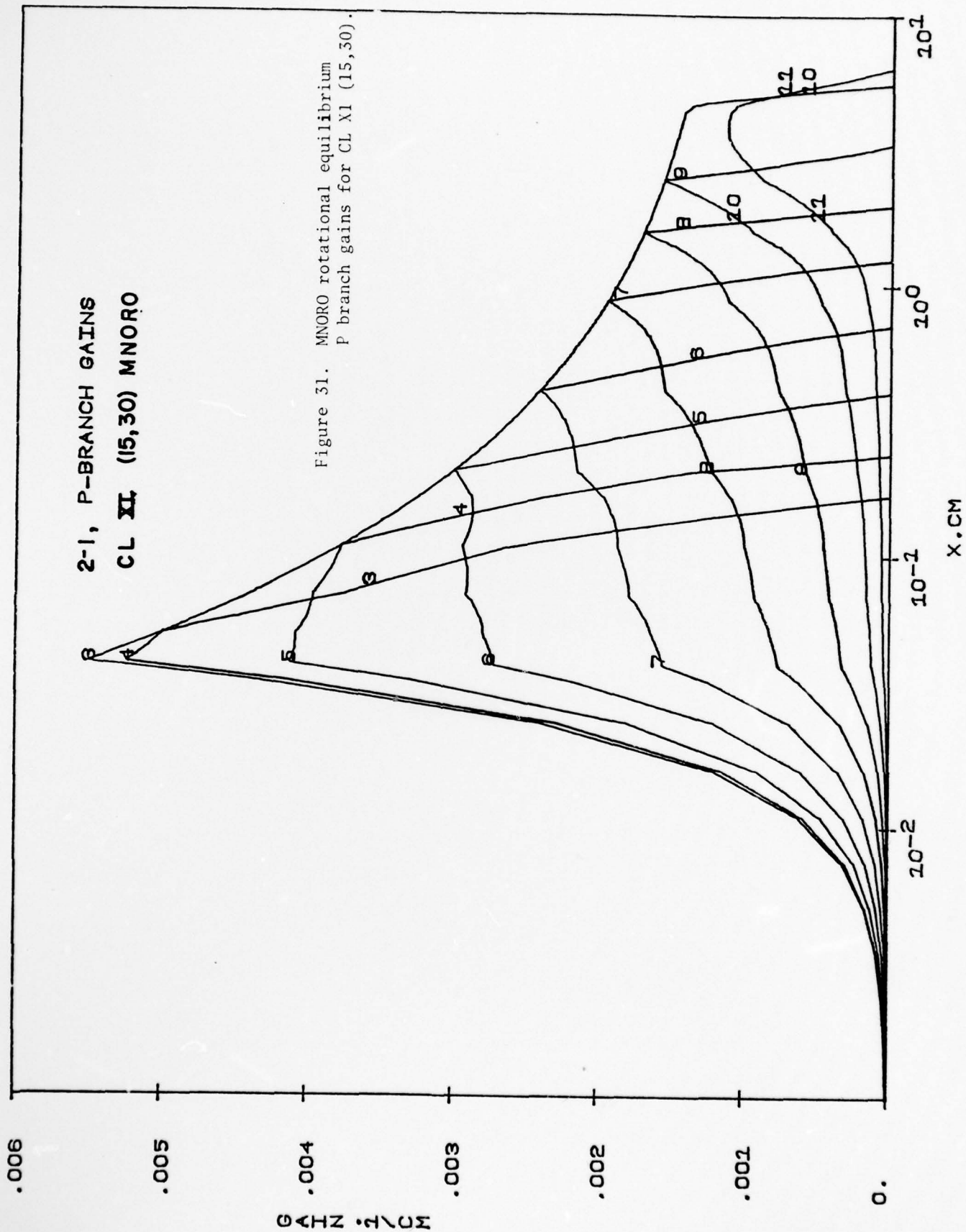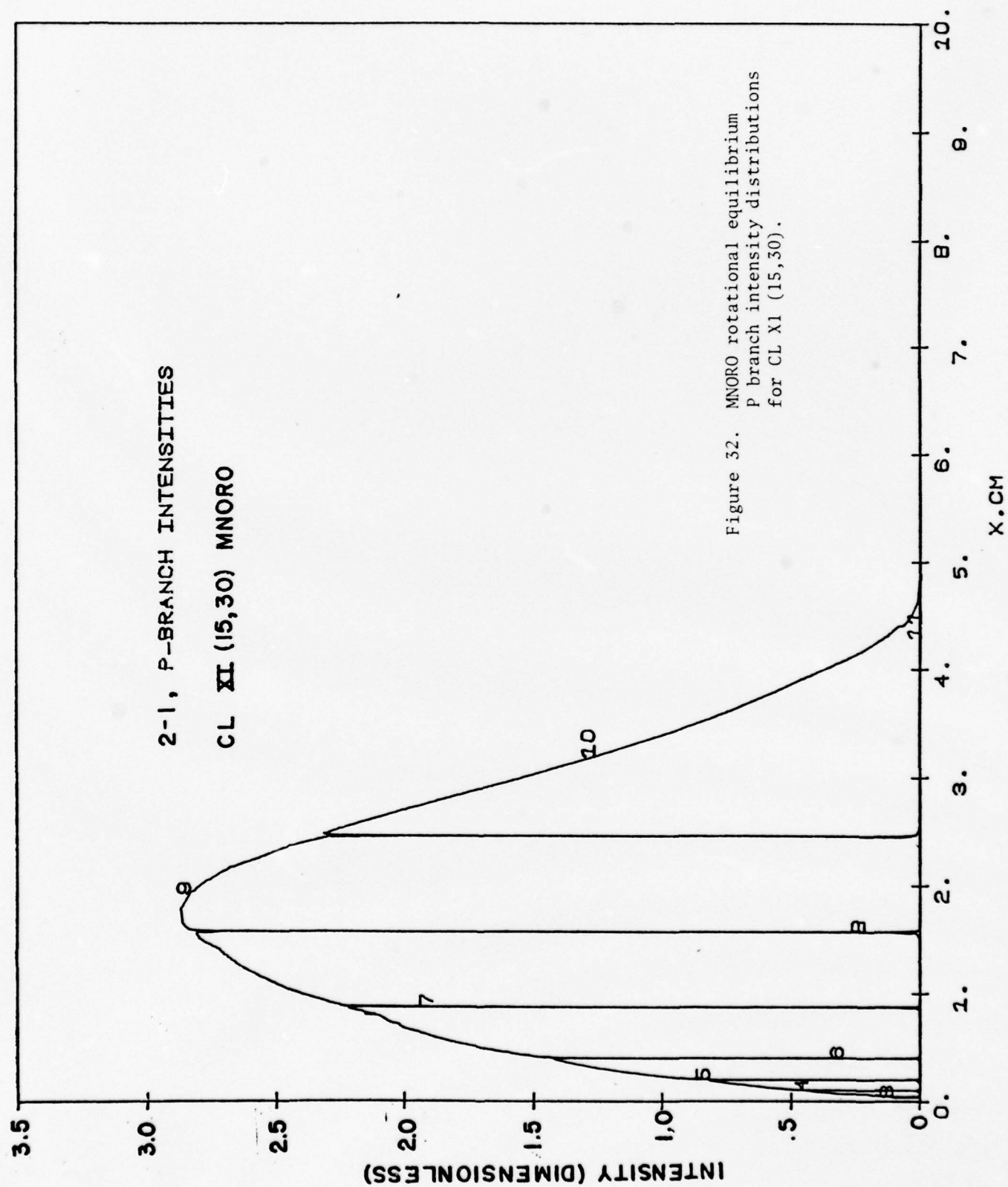
Figure 32. MNORO rotational equilibrium
P branch intensity distributions
for CL X1 (15,30).

Figure 33. MNORO rotational equilibrium total
P branch intensity distribution for
CL XI (15,30).
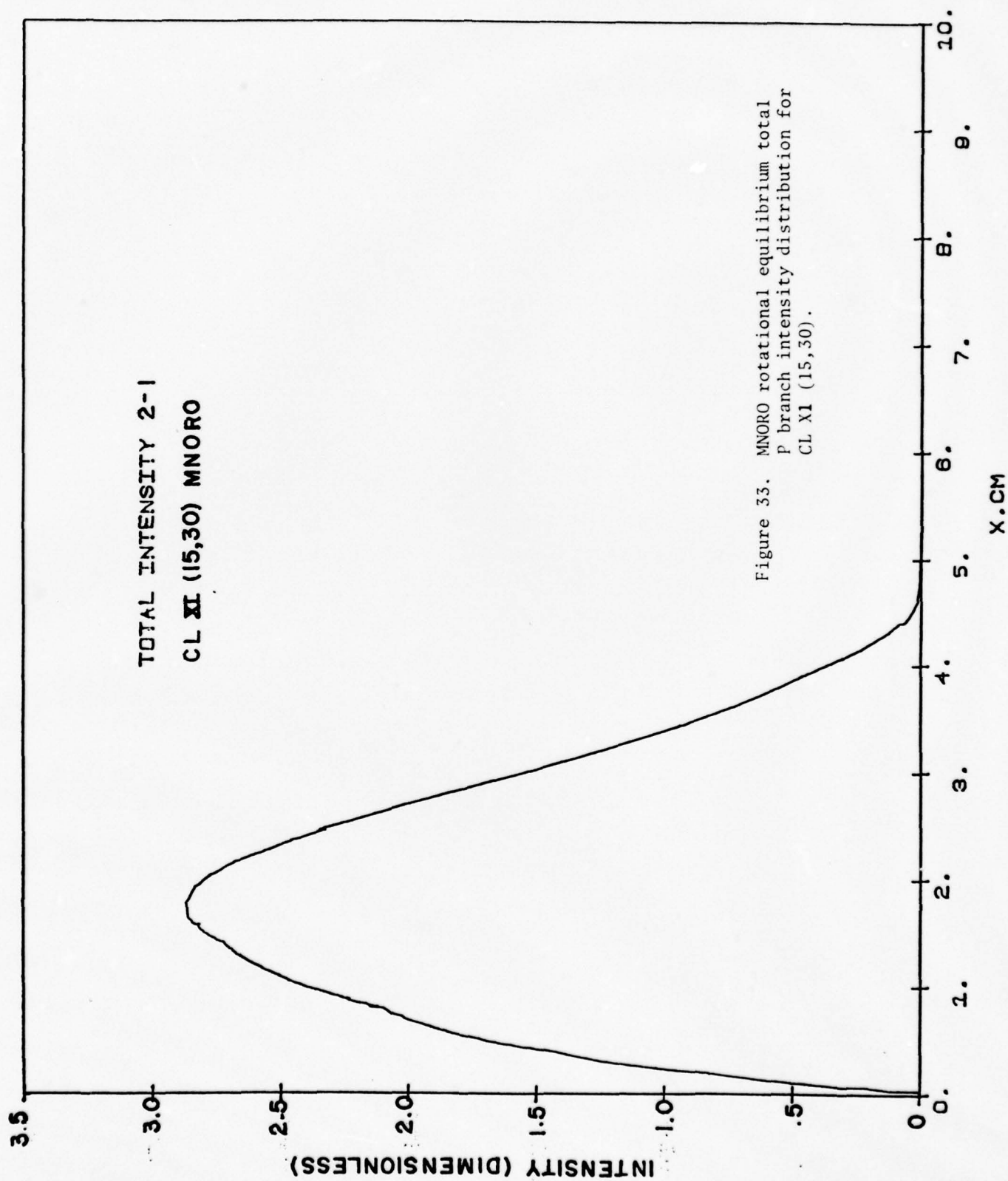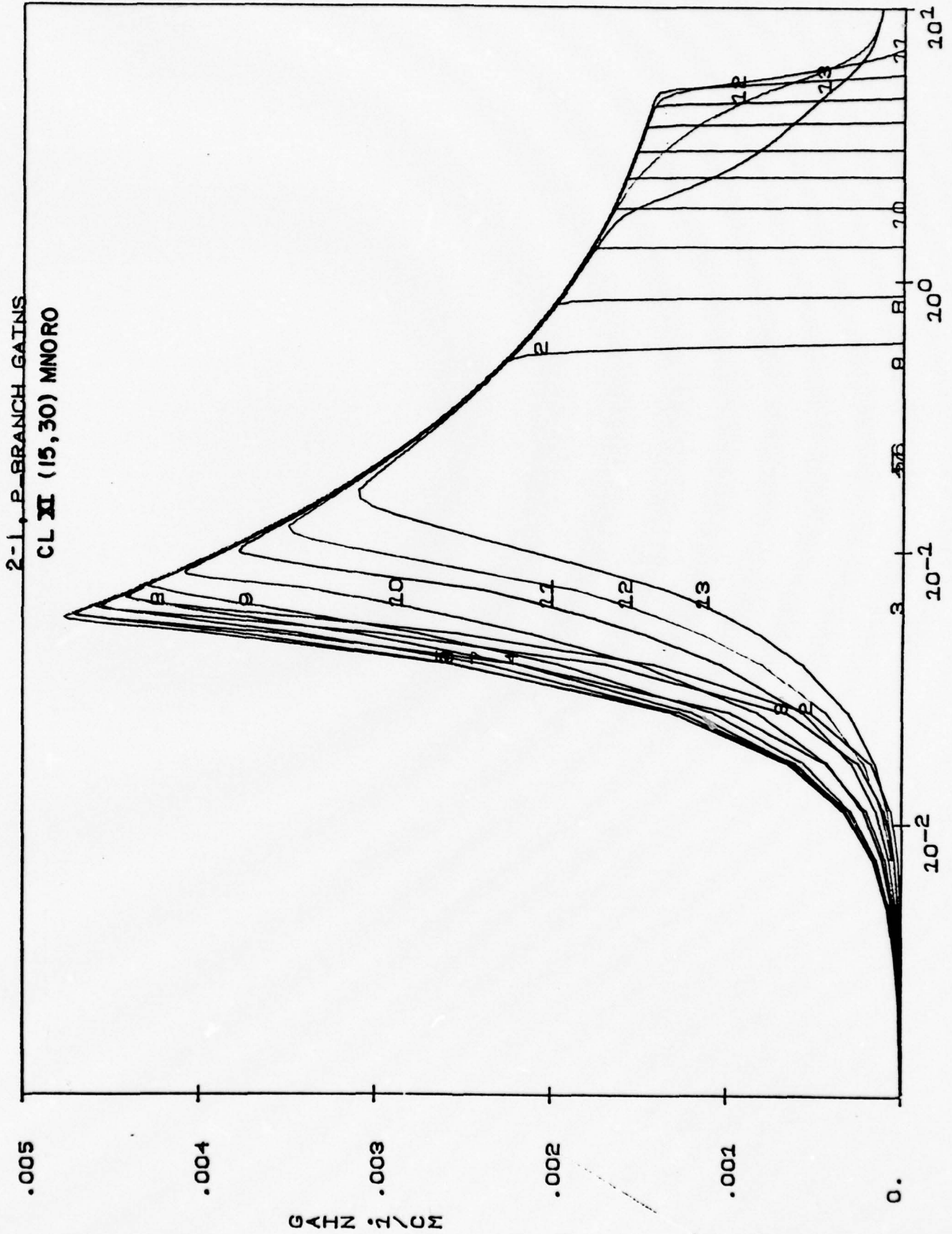
Figure 34. MNORO rotational nonequilibrium P branch gains for CL XI (15,30).
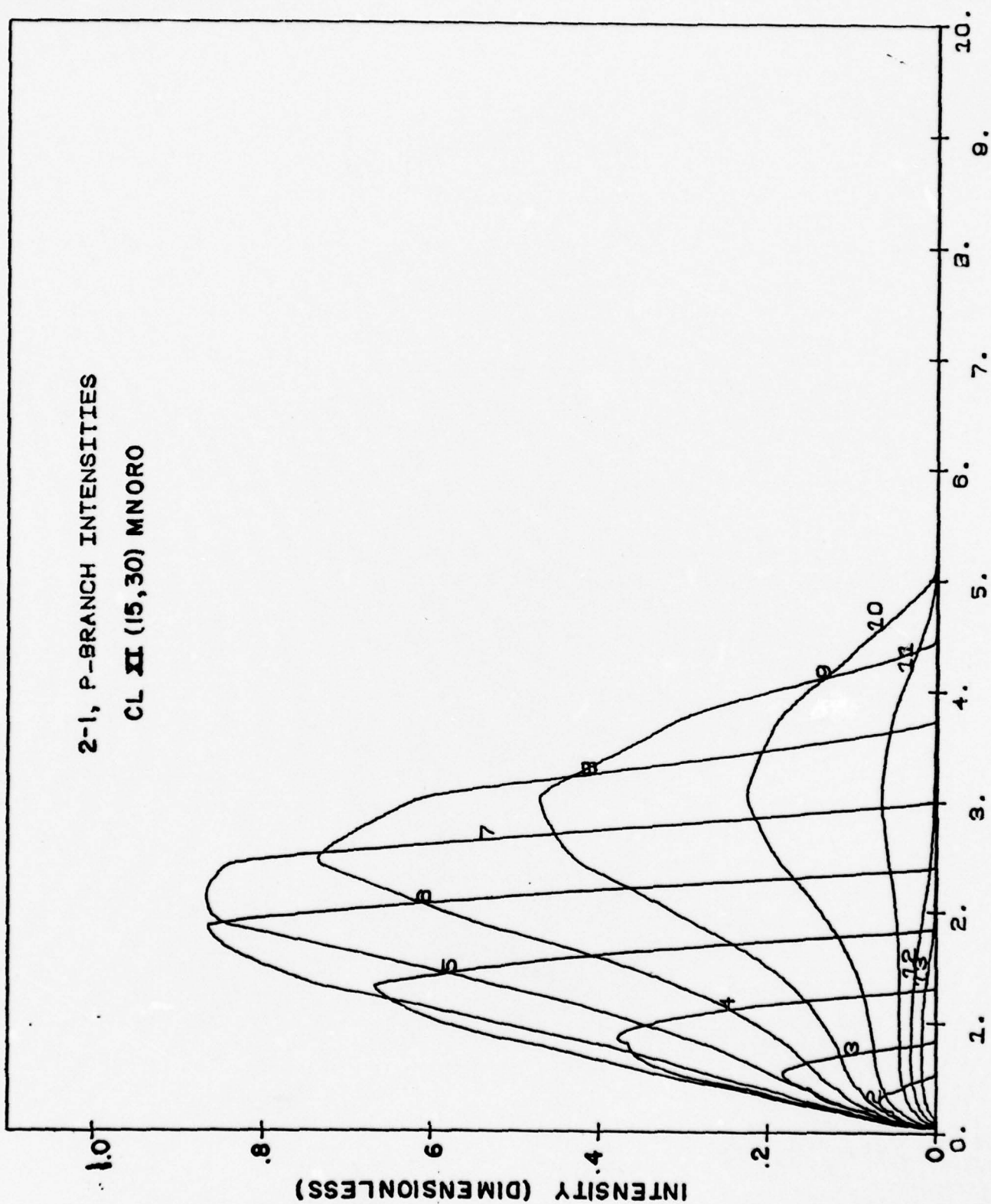
Figure 35. MNORO rotational nonequilibrium P branch intensity distributions for CL XI (15,30).
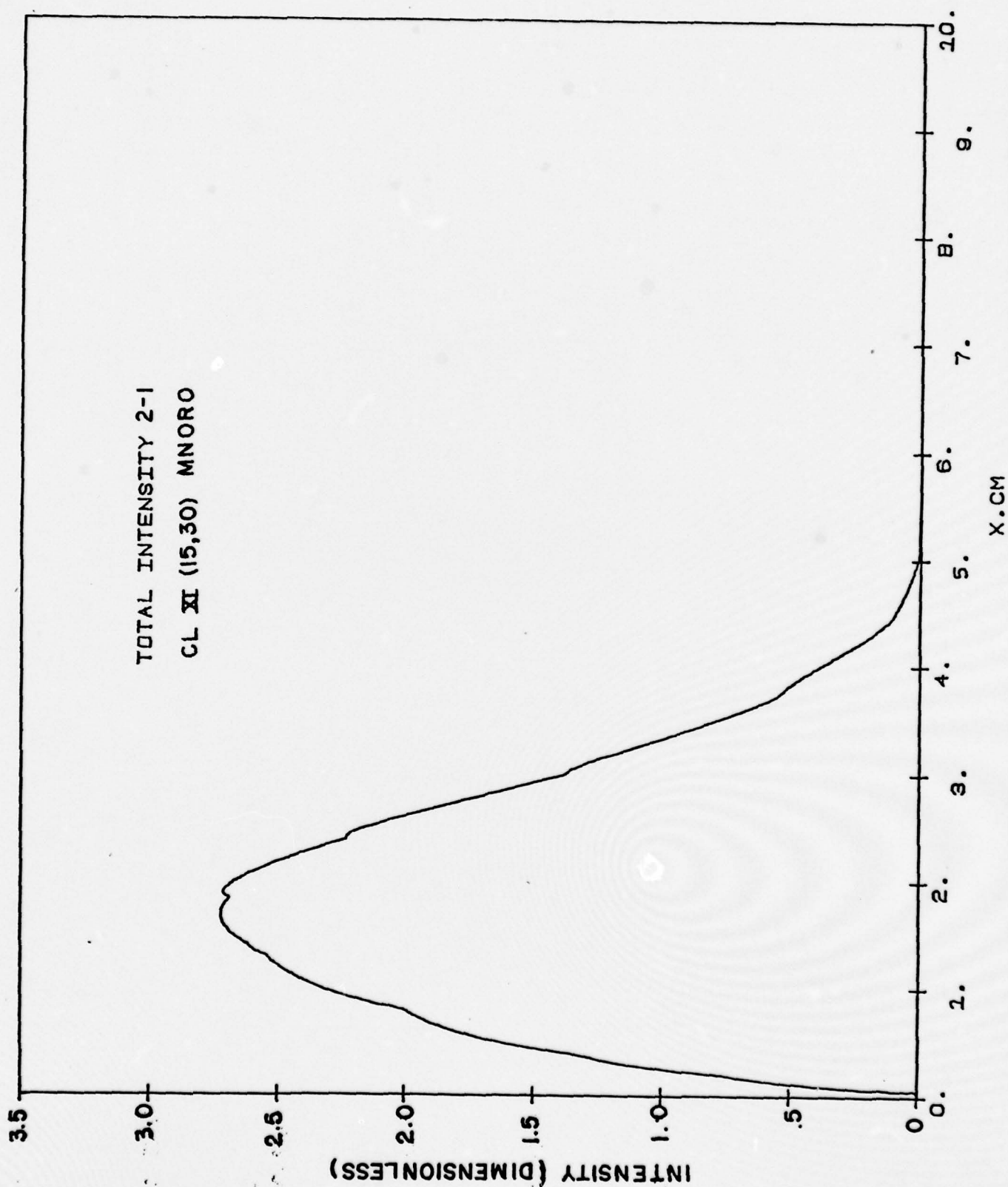
Figure 36. MNORO rotational nonequilibrium total intensity distribution for CL X1 (15,30).

promoting $3 \to 2$ lasing to obtain the increased performance on $2 \to 1$ and $1 \to 0$. As in the previous case, the equilibrium and the nonequilibrium powers only differ by about 4% rather than the 20% difference[1] observed in premixed cases.

From these comparisons, it is seen that the MNORO model includes the essential elements required to give good agreement with the very detailed Blaze II model. These elements are: lasing on $1 \to 0$ and $3 \to 2$ if it occurs, F-atom wall recombination and the hot reaction. The importance of the multi-quantum deactivation depends upon the temperature. For the Aerospace device, in which the temperature was quite low ($\sim 230°K$), multiquantum effects were less than 3%; however, for the CL XI device, in which the temperature was quite high ($\sim 585°K$), multiquantum deactivation results in about a 29% decrease in power and has a significant effect on the length of the lasing zone, Table IV.

This section will be concluded with a few remarks on run time. The rotational nonequilibrum model employs sparse matrix techniques in the evaluation and inversion of the Jacobian matrix used by the implicit integration scheme. The use of sparse matrix techniques reduces run time by factor of three. A typical case with the original rotational nonequilibrium model, Noro I, requires 30 sec (all times are on the CYBER 175). The MNORO model varied from 108 sec for the Aerospace case to 198 sec for the CL XI case. At this time, the reason for the factor of 2 increase from one case to the next is not clear. It may be associated with the fact that the Aerospace case is a slower mixing device and thus the physics occurs over longer distances permitting larger integration steps. This is suggested by the fact that the Aerospace case took 1601 steps wherease the CL XI case took 3123 steps to go 10 cm. It should be kept in mind, however, that the effect of the temperature profiles on run time is not clear; the Aerospace case had an

Model	P_{21}	$X_{Cut off}$
Blaze II	1.0	1.0
MNORO		
NO Hot Reaction NO MQVT	0.89	1.87
Hot Reaction NO MQVT	1.27	1.57
Hot Reaction MQVT	0.98	1.15
ROTATIONAL Nonequilibrium Hot Reaction MQVT	0.93	1.25

Table IV. The Effect of the Hot Reaction and Multiquantum VT Deactivation on the $2 \rightarrow 1$ Power and the Length of the Lasing Zone for CL XI (15, 30).

almost constant T whereas the CL XI profile is similar to an inverted N, and since the kinetic rates are exponential in T, this difference may be significant. The basic increase in run time from 30 sec for the original model to 108 sec for MNORO is a consequence of the increase in the number of χ_{chem} terms that must be evaluated. The original model had only one deactivating species whereas MNORO has four. The addition of dependent variables that are not lasing species affects run time only through the number of additional χ_{chem} terms to be evaluated. The run time depends quite strongly on the stiffness of the differential equations, which is determined by the χ_{rad} terms. When a transition lases, the number of places to which α agrees with $\alpha_{sat} = - (\frac{1}{2Le}) \ln r_o r_L$ is critical. This can be controlled by the quantity $\overline{K}$ (see Section 2.1). Generally, using $\overline{K} = 10 \, \sigma' T^4 / \pi$ results in α agreeing with α_{sat} to 5 or 6 places which requires the integration accuracy parameter $\varepsilon = 10^{-6}$. This combination of $\overline{K}$ and ε appears to minimize run time with no loss of accuracy.

Finally, it should be pointed out that the MNORO model cannot be run in the equilibrium mode by increasing the rotational relaxation rate constant by a factor of 10^5 when the integrator employs sparse matrix techniques. To operate MNORO in the quilibrium mode requires the complete Jacobian which generally results in a factor of 5 increase in run time.

From the preceeding results, it is seen that the MNORO model developed in this study is an efficient rotational nonequilibrium model which can be expected to provide quantitative predictions of the power and power spectral distribution of cw chemical lasers.

IV.   COUPLED PHYSICAL OPTICS AND KINETICS

The second phase of the study involved the coupling of the AFWL strip resonator physical optics code supplied by Captain Salvi, denoted by AFOPT, with the rotational nonequilibrium kinetics model. This code has been coupled to the original rotational nonequilibrium model[1], denoted NORO-1, and to the model developed during this program, denoted MNORO.

In coupling the kinetics to the physical optics, the gain medium is treated as a thin sheet located between the mirrors. The AFOPT code has the capability of allowing an arbitrary placement of the gain sheet by changing the sequence in which various subroutines are called. To check that the coupling to the kinetics was correct, several previous cases[5], which used the Bell Aerospace Textron strip resonator code, denoted BATOPT, were repeated with the AFOPT + NORO-I code. Since these previous calculations placed the gain sheet adjacent to the large mirror, this placement of the gain sheet was used here. The geometry of the unstable confocal resonator is shown in Fig. 37. The intensity sent to the kinetics must be the average of the left and right running waves,

$$I_{AV} = \{I_S[1+\exp(\alpha Lg)] + I_3[1+\exp(\alpha Lg)]\}/2 \qquad (4-1)$$

where I_S and I_3 are the intensities at positions S and 3 respectively. The solution is an iterative one. The calculation starts by passing a plane wave of roughly the expected intensity through the empty cavity. The resulting intensity distribution is sent to the kinetics. The species equations are solved with the given intensity distribution, and the gains on each line are calculated and sent to the optics. The stored wave from the preceeding optics calculation is then propagated through the cavity and incremented by the gain distribution from the kinetics. This process is repeated until the difference between successive iterates is less than some
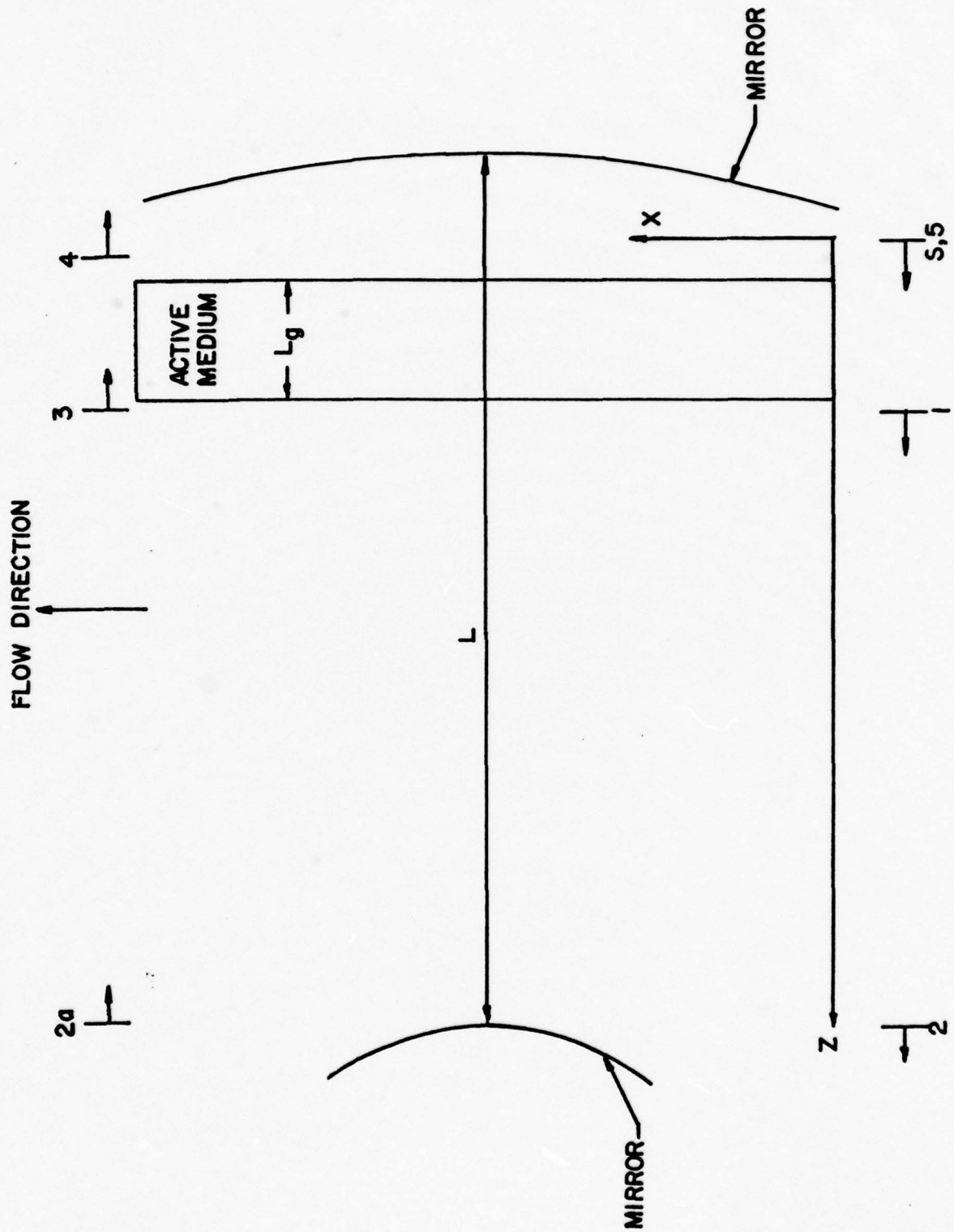
Figure 37. Confocal unstable resonator geometry and schematic of the wave propagation through the resonator.

prescribed amount. Generally, the error continues to decrease as the number of iterations increases.

To check the convergence of the iteration procedure, it has been found useful to compare the intensity distributions of successive iterates and to compare the power extracted from the medium as calculated in the kinetics and the optics parts of the code. The power calculated in the kinetics part, P_{chem}, is the total power extracted, both outcoupled and the diffractively lost power; thus, P_{chem} must be compared to $P_{LOSS\ TOTAL}$, the total power lost from the resonator in the optics part of the code. Referring to Fig. 37,

$$P_{LOSS\ TOTAL} = P_1 - P_3 + P_4 - P_5 \tag{4-2}$$

where P_i is the power at station i. In addition to the calculation of P_S, P_1, P_2, P_{2a}, P_3, P_4 and P_5, a printer plot of the intensity distribution at the outcoupling mirror, location 2, for each line and for the sum over all lines was added to AFOPT. This printer plot is quite useful for monitoring the changes between successive iterates.

The first case run with the AFOPT + NORO-I code was the 50% outcoupled, confocal unstable resonator for the single line $J = 8^5$. This case was selected because it converged in 15 iterations with no oscillations. The first three iterations were run several times with various combinations of the AFOPT control parameters. Since quite different intensity distributions were obtained depending upon the choice of the parameter gridrad, an empty resonator case was run to convergence to study the role of the guard band on the convergence and accuracy. The empty cavity case was used because it minimized CPU time.

The empty cavity solution for a confocal unstable resonator with 50% geometric outcoupling was obtained with the AFOPT and BATOPT codes. At

convergence, the two solutions agreed. However, particularly at early iterations, there were considerable differences between the two codes. These differences were perplexing since the two codes purported to follow the same physical process using identical initial conditions.

It was theorized that the observed discrepancies might be associated with the spatial frequency content of the field distribution. During the first few round trips through the cavity, the spatial frequency content or nonuniformity of the field distribution would be higher than in later transits. As convergence was approached, the field would become increasingly more uniform as the lossy high frequency components diffractively spread out of the resonator. Thus, the observed difference might be ascribed to a variation in the effectiveness of the high frequency diffractive propagators employed in the two codes. This would be a critical factor affecting the outcome of the overall study since the addition of gain, which only parially fills the resonator, stimulates and maintains the higher spatial frequency components. This rationale was the basis for the continued intensive investigation of the early iterate anomalies.

As background, the major similarities and differences between the two codes will be reviewed. Both codes begin with an arbitrary input distribution located at some point in the resonator and diffractively propagate it through the resonator until a stable irradiance and phase distribution are obtained. The version of the Bell Aerospace Textron 1D resonator code being used in this case always expresses the complex field on a plane perpendicular to the optical axis. When mirrors are encountered, the phase of the field on the plane is adjusted to approximate the effects of the curvature of the mirror. The amplitude of the field at a mirror is adjusted to correct for the mirror absorption over the clear aperture and the edges are truncated to account for the finite mirror limits. Finally,

the phase of the field is reversed to account for the change in direction caused by the beam's reflection. The diffractive propagation of the beam is performed using the Huygens-Fresnel scaler approximation.

The Huygens-Fresnel approximation to the Kirckhoff integral involves the convolution of a known kernel with the input field to yield the output field distribution. It should be noted that almost the entire body of existent diffraction theory can be traced back to this relationship. Fourier theory is used to perform the convolution since the Fourier transform of the output field can be expressed as the product of the Fourier transform of the input field multiplied by the Fourier transform of the kernel. Within the Huygens approximation, the transfer function of the Fourier transform of the kernel is known in analytic form. The Bell approach proceeds by numerically Fourier transforming the input field distribution and multiplying by the transfer function. The desired output field after propagation is then determined by an inverse Fourier transform of the resultant product.

The Fourier transform is obtained using a numerical technique known as the FFT. For a given input vector having N elements, the FFT will return N output elements which, under given circumstances, may be interpreted as being an approximation to the Fourier transform of the input vector. Great care must be exercised in using and interpreting the results of the FFT. The function to be transformed is sampled at uniformly spaced locations. These sample points together with a number of zeros form the input vector to the fast Fourier transform. The total number of input vector points together with the ratio of real to dummy arguments determines the returned maximum extent and spacing of the transformed function in frequency space. During these studies, the Bell code used an FFT input vector of 2^{13} of which only 900 points represented the actual optical field

to be transformed. The remaining points were loaded with zeros. This arrangement may be shown to theoretically allow for a maximum frequency space span of ±900 cycles per mirror diameter with resolution of approximately 0.1 cycles. It may also be shown that for the resonator under study, an ideal point sampling scheme would have utilized an even higher ratio of total FFT points to optical field points. At present it is sufficient to note that this is a key factor in determining the maximum effective spatial frequency range of the calculational method.

The Air Force optics code also begins with an arbitrary field distribution and propagates it around the resonator. In the collimated beam direction (i.e., from the large to the small mirror), the field is expressed on a plane perpendicular to the optical axis. At the small mirror, a change is made to (r, ϕ) coordinates with the radius chosen to match the curvature of the expanding geometric mode. By assuming that the angular and cartesian points are approximately coincident, the curvature of the mirror is absorbed into the coordinate change. Additional correction need only be made to account for the finite absorption and dimensions of the mirror together with the phase change due to reflection.

The conversion to this expanding coordinate scheme with its associated elimination of the multiplicative mirror curvature term is advantageous since the spatial frequency content of the optical field is reduced, thereby reducing both real and frequency space sampling requirements. One minor drawback to the coordinate change, however, occurs because of the desire to keep a constant number of sample points in both collimated and expanding space. For this reason it is necessary for the code to interpolate at the small mirror to provide a number of intermediate field samples to replace those points that were lost in forming the output portion of the beam in

collimated space. The interpolation is provided by fitting the complex field function with a spline and extracting the required intermediate data points.

An analysis of the general expanding vs fixed mesh techniques indicated that the observed output variations could not be explained merely on the basis of the differences in the coordinate system representations or the effects of the associated interpolation, assuming both codes are functioning properly. In order to remove differences caused by FFT sampling variations, an additional propagator was written and added to the Bell code. The test propagator solved the basic Fresnel-Kirckhoff integral using standard Fresnel integral subroutines with the convolution performed numerically. This basic approach was formulated in the conventional form for planer propagation which is suitable for operation within the framework of the Bell code. Care was taken that sufficient sample points were available for an accurate evaluation. The results agreed with the output obtained using the original Fourier transform propagator in the Bell code.

The numerical aspects of the particular case under study were examined. It was hypothesized that variations in the spatial frequency content would vary as the iterative process proceeded causing possible numerical problems at intermediate steps. This effect was treated both theoretically in terms of determining the required number of points and experimentally by varying both the number of points and the FFT guard band. Both of these approaches indicated that the observed effect was not associated with propagator numerics. A similar analysis indicated sufficient field sampling points such that the additional mirror curvature term in the Bell model was well resolved.

After eliminating these potential sources for the observed discrepancies, the AFOPT averaged kernel propagator was considered as the most likely culprit. In order to check this portion of the code, the AFOPT code was temporarily modified. The averaged kernel in the AFOPT code does not have a known analytic transfer function and therefore is numerically determined using an FFT. This numerical portion of the code was bypassed and replaced by an equation representing the analytic form of the unaveraged transfer function in both the collimated and expanding cylindrical coordinates. In addition to added efficiency, this approach prevented the generation of high frequency numerical garbage which would have occurred if attempts had been made to numerically compute the transfer function from the unaveraged kernel.

A comparison of the averaged and unaveraged transfer functions showed some slight variation in the significant low frequency portions of the spectrum. The high frequency components were of course damped by the averaging process but this is of no significance. The averaged transfer function showed a slight premature dip just above zero frequency but then returned and tracked well with the unaveraged version. Unfortunately, this perturbation was found to have a negligible effect on the calculated intermediate iterative results in the AFOPT code.

The final source of the variation considered was the AFOPT spline interpolation scheme. When interpolation takes place at the small mirror, additional points are loaded with interpolated values to compensate for those lost due to the continuously expanding coordinate system. It was conjectured that this finer resolution together with its smoothed interpolated data fit might tend to surpress high frequency components. This was tested by overriding the interpolation routine and filling intermediate grid points with neighboring values. By this technique the field resolution would be

effectively the same as that used in the Bell code. This again proved to be a null experiment in that essentially no change in the output was observed.

At the conclusion of the contract, the source of the discrepancy had not yet been isolated although a number of possible causes had been eliminated. If time had permitted, the next step would have involved a stepwise investigation of the actual initialization process used in the codes.

Since the BATOPT and AFOPT codes gave the same empty cavity result at convergence even though the intermediate results differ, several of our previous loaded cavity cases were run to convergence with the AFOPT + NORO-I code to determine the role of the gain medium. The single line $J = 8$ case for a confocal unstable resonator with 50% geometric outcoupling was run. The results are compared to our previous results for this case which were obtained using the Bell Aerospace Textron optics code, Figs. 38 - 42. As can be seen, the results from the two codes are in excellent agreement with each other. Since the saturated gain fills the resonator, a converged solution is reached in about 15 iterations. For a second check case, the single line $J = 4$ case for the same resonator was run. In this case, the saturated gain only fills half the resonator which results in an oscillation[5]. The convergence parameters versus iteration number are shown in Figs. 43 and 44. The AFOPT + NORO-I code gives a 6-7 iteration oscillation whereas the BATOPT + NORO-I gives a 3-4 iteration oscillation. A check of the location of the peak of the average intensity, Fig. 45 shows that while the intensity peak for the BATOPT + NORO-I is at about 0.1, the intensity peak for the AFOPT + NORO-I is about 0.15; for these locations of the intensity peaks, the 4 and 6 iteration oscillations are what should occur. These differences could be due to one of two factors, the size of the

BATOPT + NORO I
ROTATIONAL NONEQUILIBRIUM
50% OUTCOUPLED, CONFOCAL UNSTABLE
RESONATOR SINGLE LINE J=8

Figure 38. Convergence parameters versus iteration number for single line $P_2(8)$ for BATOPT + NORO I[5].

83

Figure 39. Convergence parameters versus iteration number for single line $P_2(8)$ for AFOPT + NORO I.

Figure 40. Comparison of saturated gains given by BATOPT + NORO I and AFOPT + NORO I for single line $P_2(8)$.

Figure 41. Comparison of intensities at the outcoupling mirror given by
BATOPT + NORO I and AFOPT + NORO I for single line $P_2(8)$.

ROTATIONAL NONEQUILIBRIUM
SINGLE LINE J=8
50% OUTCOUPLED, CONFOCAL
UNSTABLE RESONATOR

I_{AV} AT START OF ITERATION

20

AFOPT + NORO I

BATOPT + NORO I

AVERAGE INTENSITY SENT TO CHEMISTRY
(DIMENSIONLESS)

DIMENSIONLESS DISTANCE

Figure 42.   Comparison of the average intensities sent to the kinetics given
by BATOPT + NORO I and AFOPT + NORO I for single line $P_2(8)$.

BATOPT+NORO I
ROTATIONAL NONEQUILIBRIUM
50% OUTCOUPLED, CONFOCAL
UNSTABLE RESONATOR
SINGLE LINE J=4
912 PTS ON MIRROR
8196 PTS TOTAL

P_{LOSS} TOTAL / P_{CHEM}

OUTCOUPLED POWER
(DIMENSIONLESS)

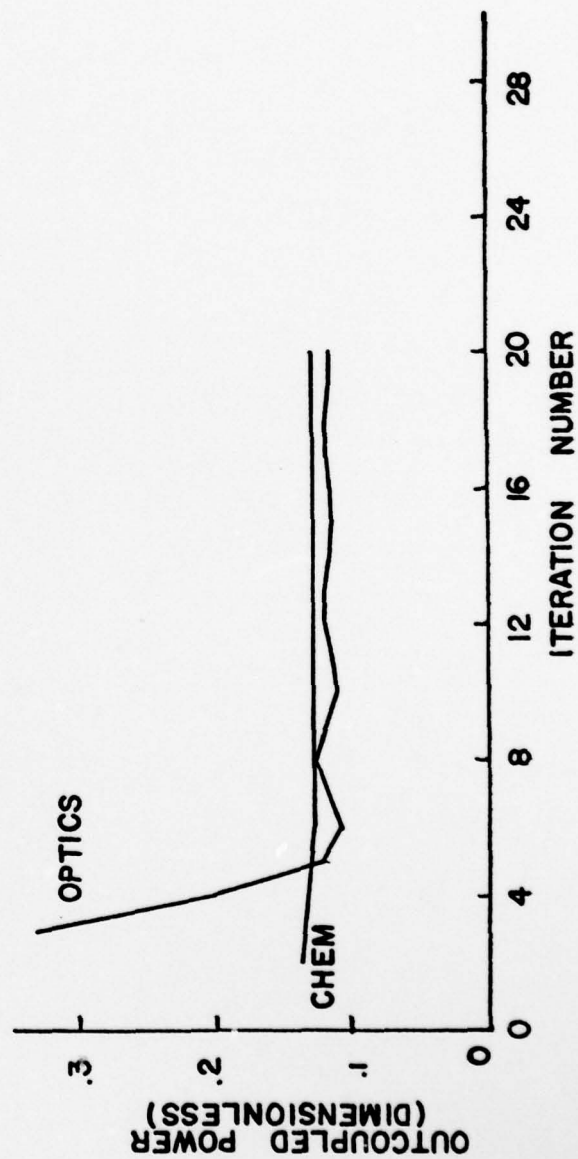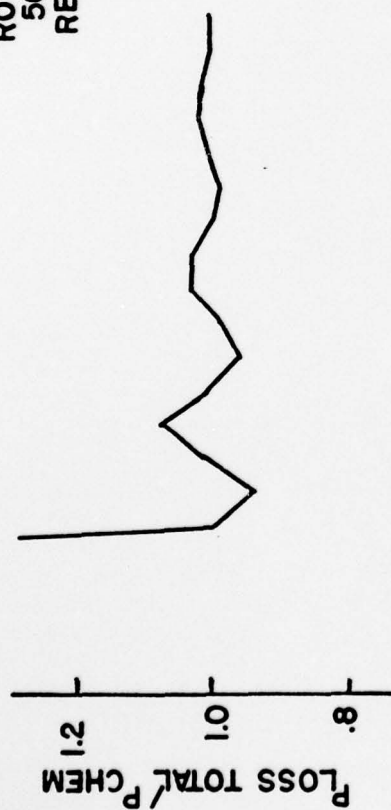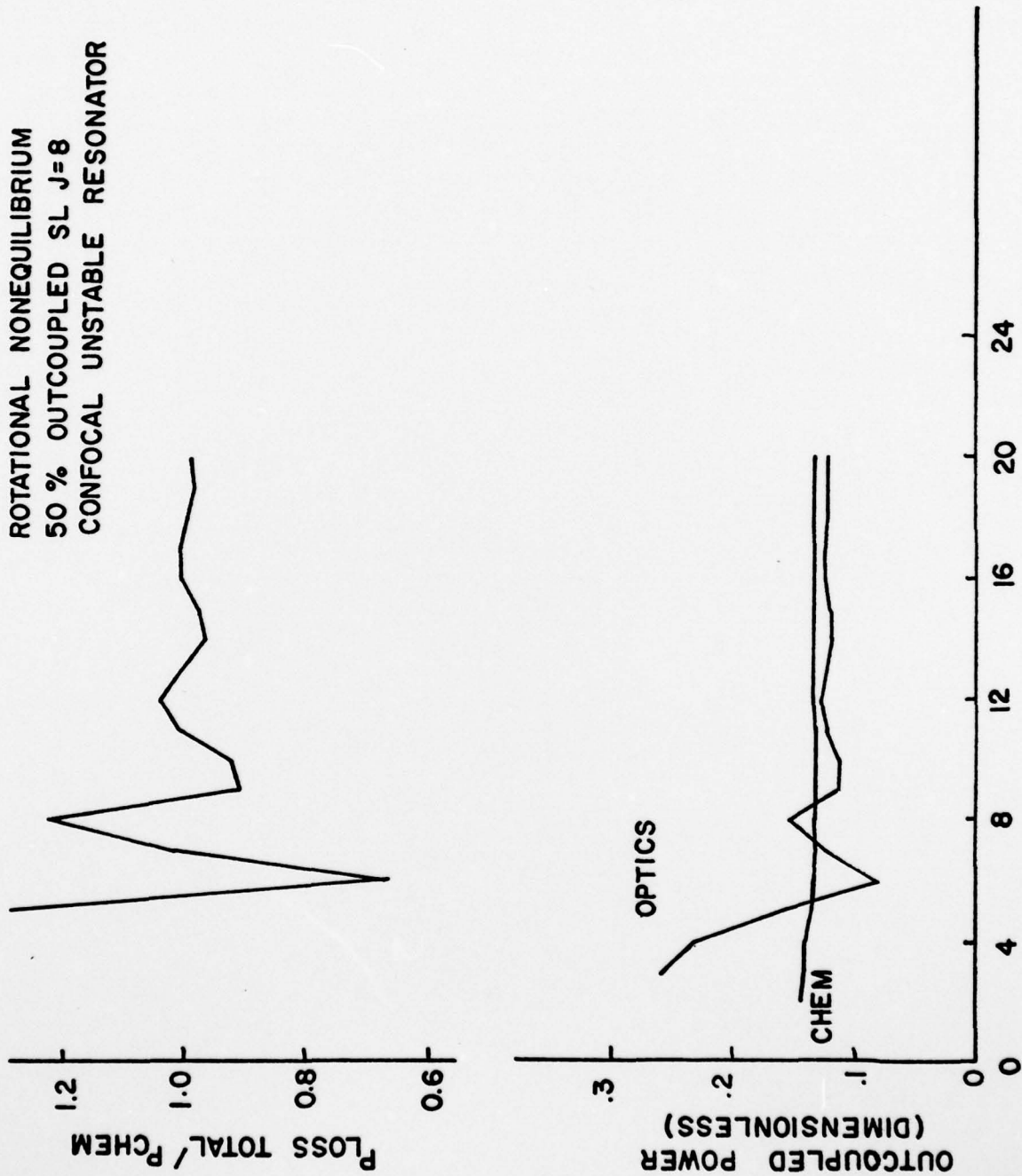OPTICS

CHEM

ITERATION NUMBER

Figure 43. Convergence parameters versus iteration number for single line $P_2(4)$ for BATOPT + NORO I[5].

AFOPT + NORO I
ROTATIONAL NONEQUILIBRIUM
50% OUTCOUPLED SLJ=4
CONFOCAL UNSTABLE RESONATOR
912 PTS ON MIRROR   1024 PTS TOTAL

P_{LOSS} TOTAL/ P_{CHEM}

OUTCOUPLED POWER
(DIMENSIONLESS)

ITERATION NUMBER

Figure 44. Convergence parameters versus iteration number for single line $P_2(4)$ for AFOPT + NORO I.
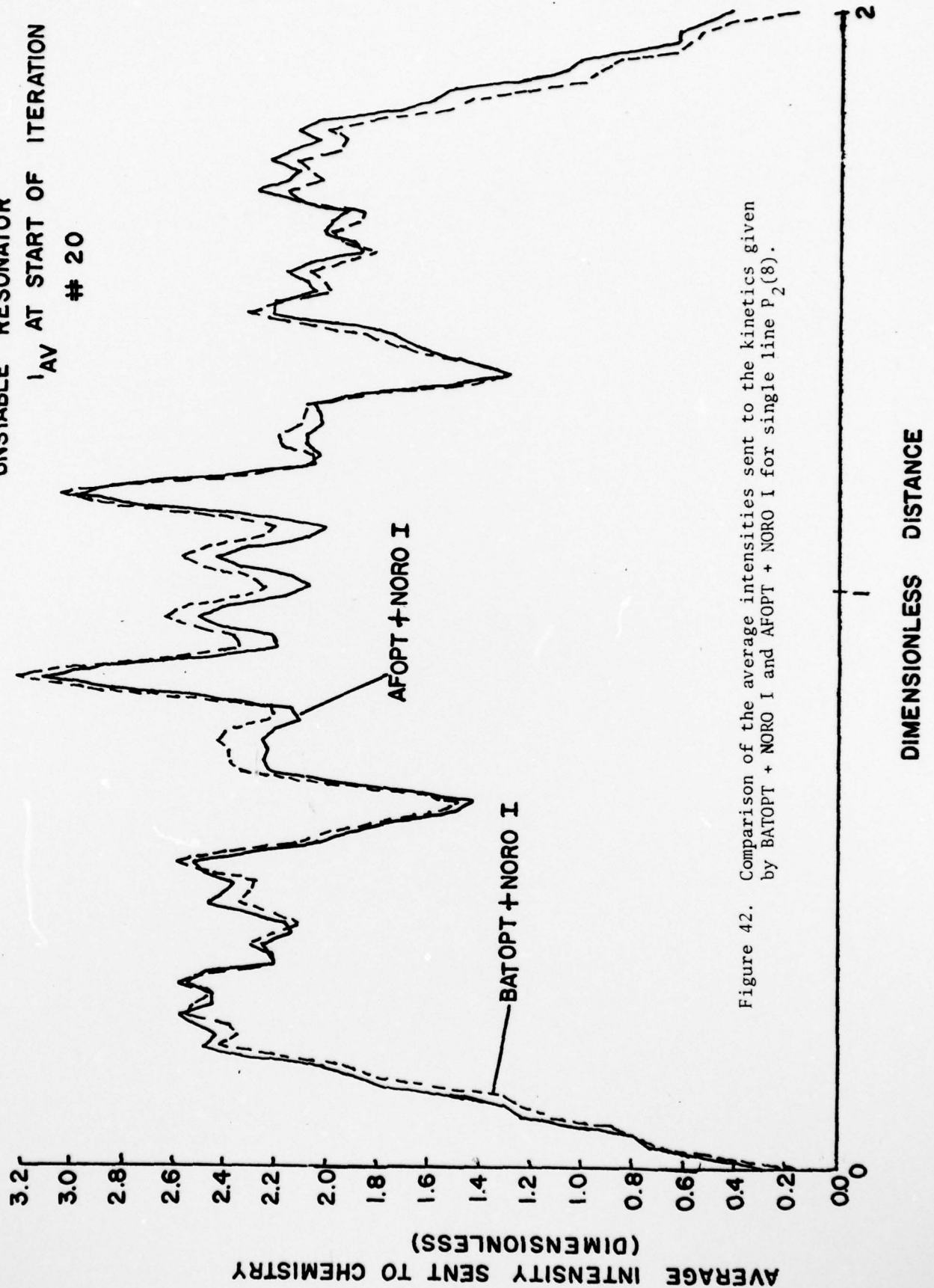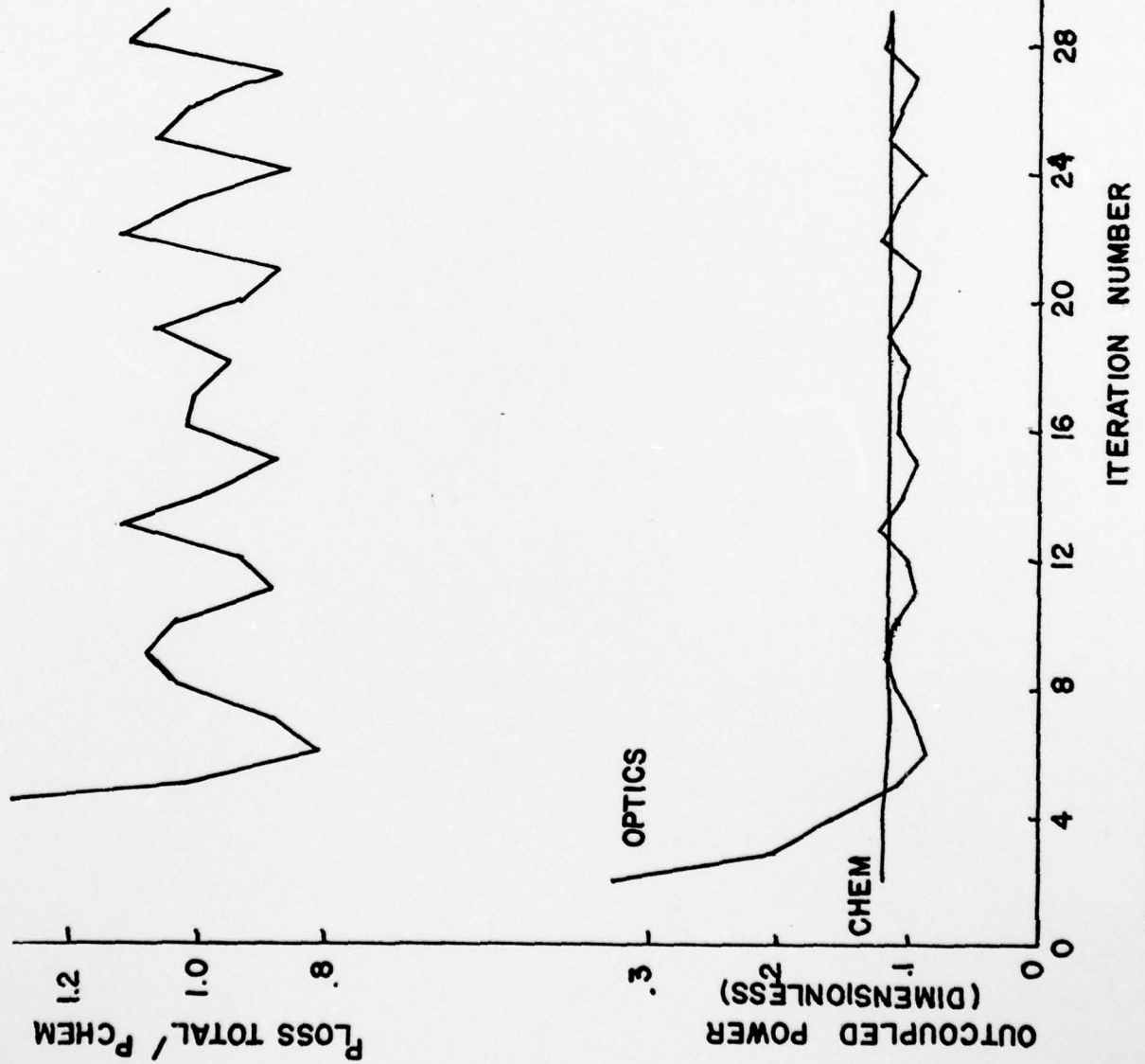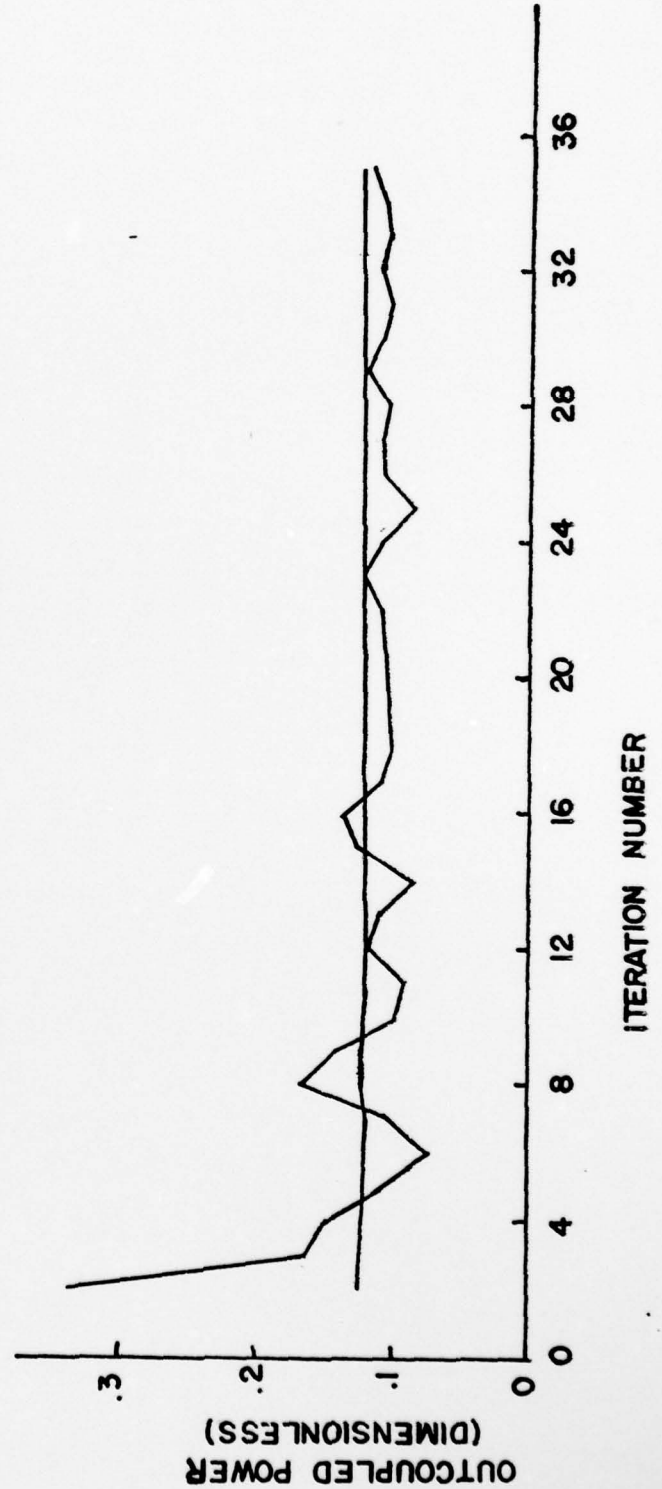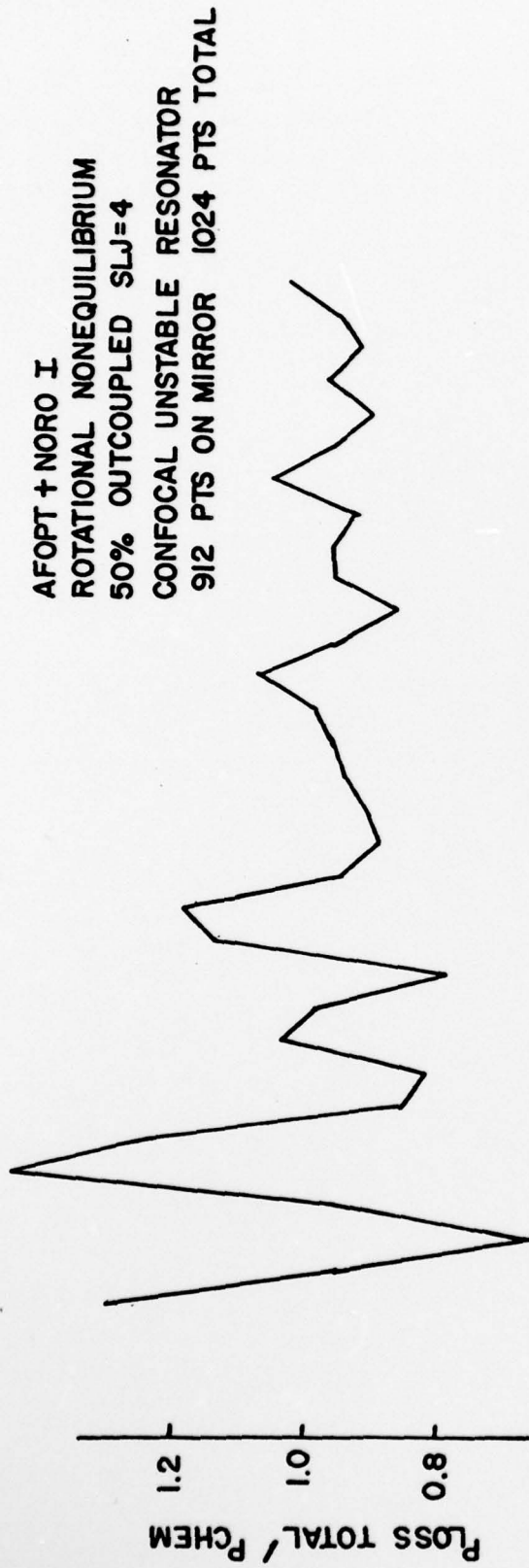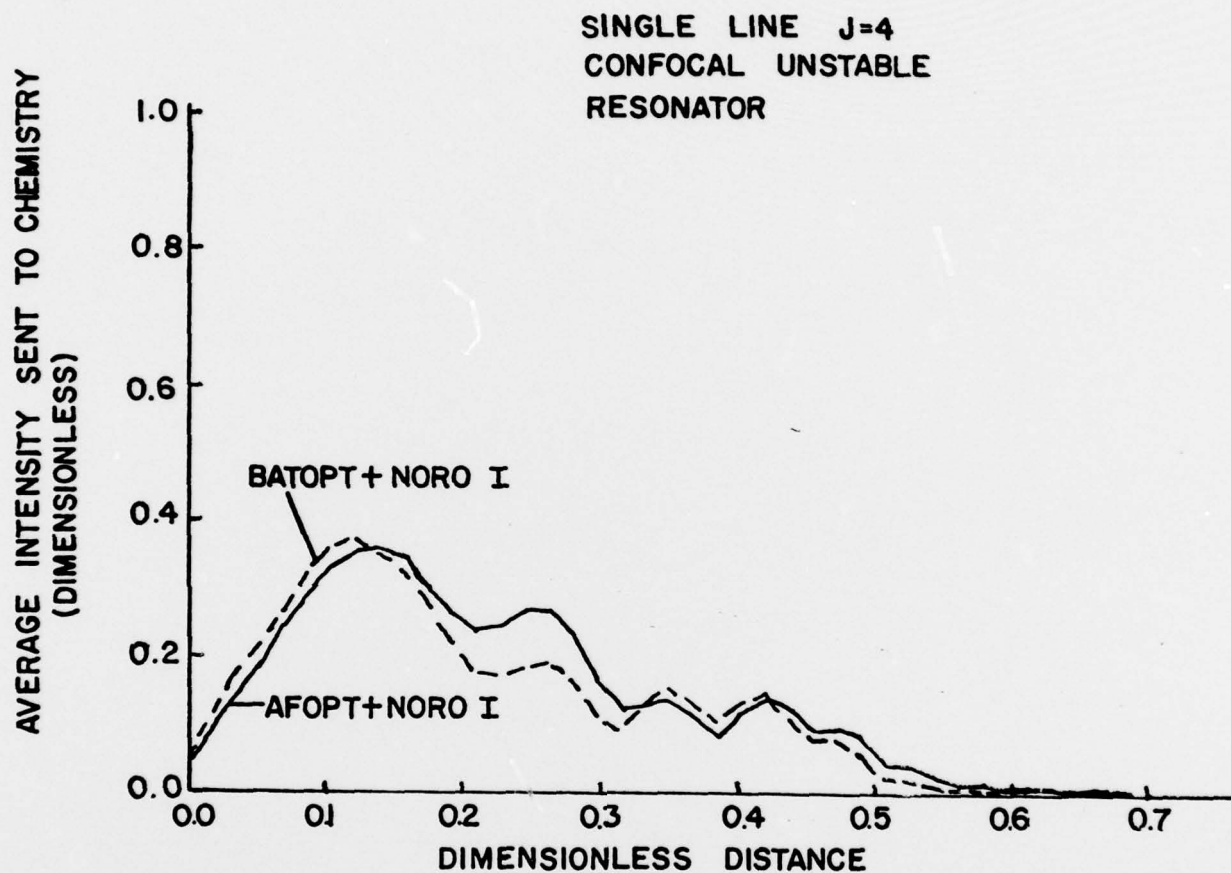
Figure 45. Comparison of the average intensity sent to the kinetics given by BATOPT + NORO I and AFOPT + NORO I for single line $P_2(4)$.

guard band used (8196 for BATOPT and 2048 for AFOPT) or to the different treatments of the kernels (average kernel in AFOPT and exact kernel in BATOPT), although based on the empty cavity checks of these factors, no changes were expected.

To check the effect of the guard band, the single line J = 4 case was run with 8196 points total with the same 912 points on the mirror. The same results were obtained as with 2048 points total with 912 on the mirror. Thus, the size of the guard band does not seem to be responsible for the slight difference between the AFOPT and BATOPT results for this case.

To check the effect of the averaged kernel, the single line J = 4 case was rerun using the modified AFOPT which employed the unaveraged kernel. The results, shown in Fig. 46, are identical to those obtained with the averaged kernel. Thus, at the conclusion of the grant, the source of the discrepency between the two optics codes for the case of the saturated gain filling half the resonator had not been isolated. As in the empty cavity case, the next step would have involved a stepwise investigation of the actual initialization process used in the codes. However, it should be pointed out that the qualitative results from the two optics codes agree in all cases studied.

To summarize, the BATOPT and AFOPT optics codes give identical results at convergence for both empty and loaded resonator cases. They differ at intermediate iterates before convergence and, in the case of a loaded resonator in which the saturated gain does not fill the resonator, they give slightly different locations of the intensity peak and thus, slightly different periods of the oscillation of the intensity. These results and the extensive tests conducted to determine the source of these differences demonstrated that the various theoretical approaches to the physical optics model give
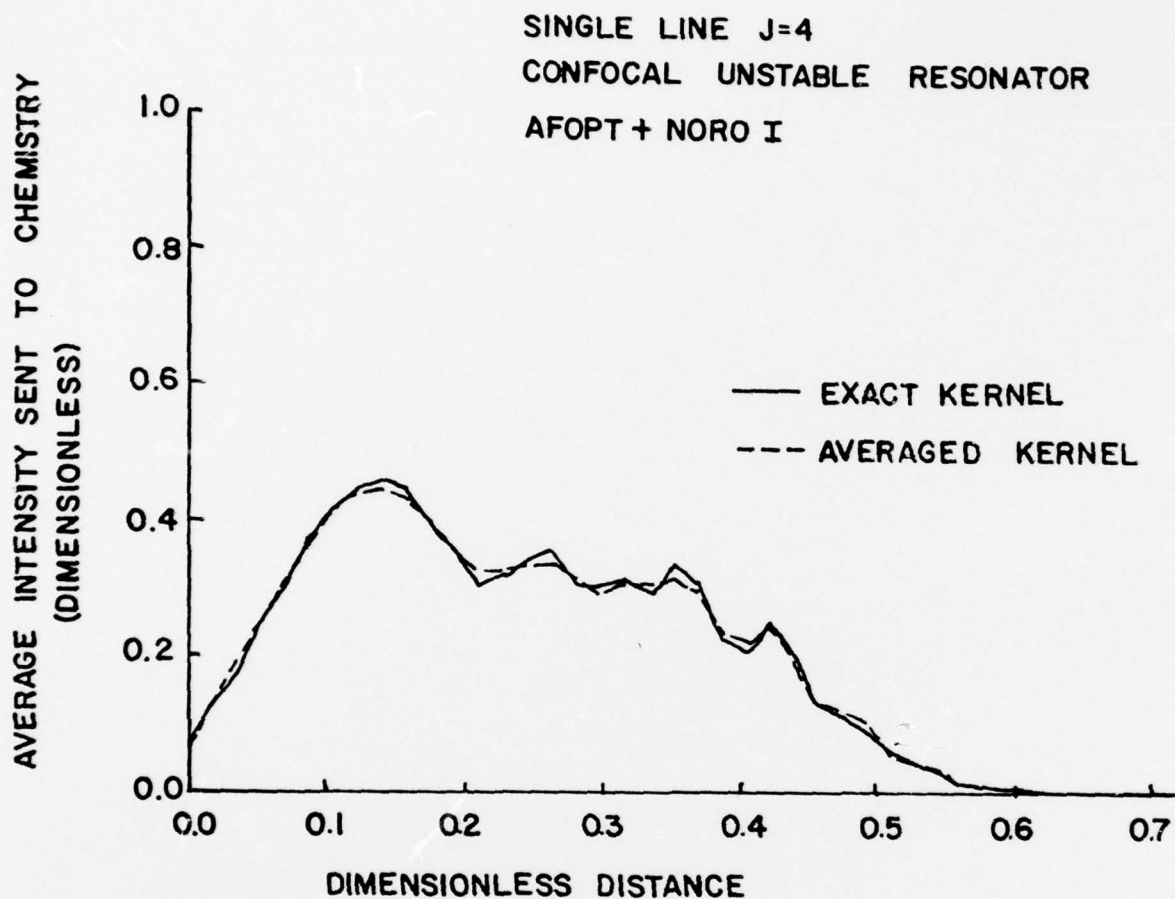
Figure 46. Comparison of the average intensity sent to the kinetics given by AFOPT + NORO I using the averaged kernel and the exact kernel in the propagation routine. Single line $P_2(4)$, 50% outcoupled, confocal unstable resonator, 1024 points total with 912 points on the mirror.
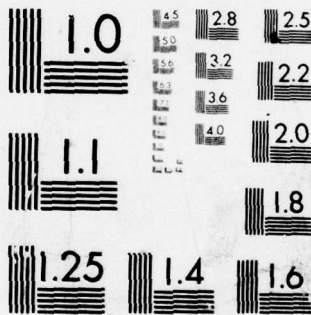
MICROCOPY RESOLUTION TEST CHART

NATIONAL BUREAU OF STANDARDS-1963-A

surprisingly good agreement. The studies with the spline interpolation routine appeared to indicate that a simple duplication of adjacent values provided essentially the same result as an elaborate curve fit routine. In addition, the simple analytic form of the exact transfer function appeared to agree with the more complex numerical approach used in the averaged kernel technique. These comparisons indicated that both optics codes could be modified to operate more efficiently.

The AFOPT code was coupled to the new kinetics model developed in this study. The resulting code, AFOPT + MNORO, has been checked out to determine that it operates correctly, but unfortunately, the grant terminated before the preceeding Fabry-Perot cases could be run with an unstable resonator.

V. CONCLUDING REMARKS

From the detailed comparison between the Blaze II and MNORO results, the objective of developing an efficient rotational nonequilibrium model of a cw chemical laser which is capable of giving quantitative predictions of the power spectral distribution has been achieved. This model has been coupled to the AFWL strip resonator code. Unfortunately, the grant ended before the coupled code could be exercised. In the process of this development, several problem areas have come to light.

In addition to the recognized difficulties with the HF rate package, the prediction of lasing on the upper vibrational bands and on $3 \rightarrow 2$ for cases in which the experimental data indicates no lasing above $2 \rightarrow 1$ suggests a fundamental problem with the HF rate package, either in the pumping rates to the higher vibrational levels or in the deactivation rates of those higher levels. Until this question is answered, the determination of mixing parameters by requiring total power and lasing zone length to agree with experimental data is suspect.

The effect of F atom wall recombination is to slow down the mixing. Does F atom wall recombination really occur or is this a way of correcting errors in the mixing model?

What all of these comments indicate is the need for a series of experiments to determine the role of the kinetics and the mixing. It is essential that these experiments be carried out for a geometry for which the fluid dynamic mixing can be accurately modeled, i.e., laminar two stream mixing. For this geometry, sufficiently detailed fluid dynamic measurements must be made to verify the mixing model; for the same geometry, power, power

spectral distribution, and intensity distribution on each line for a
Fabry-Perot cavity should be measured. Such a data base would permit a
resolution of the questions which have been raised.

The present model, in which the fluid dynamic variables are input
quantities, generalized to include three lasing levels would be quite useful
in checking the kinetics model against such data.

The detailed comparison of the BAT and AFWL strip resonator codes
has provided confidence in both optics models and has suggested ways the
efficiency of both codes can be increased. The coupled AFOPT + MNORO model
should be exercised to determine the combination of parameters such as num-
ber of points the cavity is divided into and the kinetics integrator error
parameter that minimizes run time without loss of accuracy.

REFERENCES

1. L. H. Sentman, J. Chem. Phys. 62, 3523 (1975).

2. J. J. T. Hough and R. L. Kerber, Appl. Opt. 14, 2960 (1975).

3. R. J. Hall, IEEE J. Quantum Electron. QE-12, 453 (1976).

4. J. G. Skifstad and C. M. Chao, Appl. Opt. 14, 1713 (1975).

5. L. H. Sentman, Appl. Opt. 17, 2244 (1978).

6. L. H. Sentman, M. Subbiah, and S. W. Zelazny, "Blase II: A Chemical
    Laser Simulation Computer Program", T.R. H-CR-77-8, Bell Aerospace
    Textron, Buffalo, NY, February 1977 (prepared for U. S. Army Missile
    Research and Development Command, Redstone Arsenal).

7. J. Thoenes et al., "Analysis of Chemical Lasers", Lockheed Technical
    Report RK-CR-74-13, Vols. 1-5, June 1974, Lockheed Missiles and Space
    Company, Inc., Huntsville, AL.

8. J. D. Ramshaw and J. K. Dukowicz, "APACHE: A Generalized-Mesh Eulerian
    Computer Code for Multicomponent Chemically Reactive Fluid Flow",
    LA-7427, Los Alamos Scientific Laboratory, January 1979.

9. D. J. Spencer, H. Mirels and D. A. Durran, "Performance of CW HF
    Chemical Laser with N_2 or He Diluent", TR-0172(2777)-1, The Aerospace
    Corp., Los Angeles, CA, March 15, 1972.

10. J. C. Polanyi and K. B. Woodall, J. Chem. Phys. 57, 1574 (1972).

11. J. C. Polanyi and K. B. Woodall, J. Chem. Phys. 56, 1563 (1972).

12. J. J. Hinchen, Appl. Phys. Lett. 27, 672 (1975).

13. L. H. Sentman, J. Chem. Phys. 67, 966 (1977).

14. G. Tregay and R. J. Driscoll, private communication, October 1978.

15. W. Rushmore, private communication, January 1979.

UNIVERSITY OF ILLINOIS

RECENT AERONAUTICAL AND ASTRONAUTICAL
ENGINEERING DEPARTMENT TECHNICAL REPORTS

Technical Report Number	Title	Author	Journal Publication
AAE 62-1	An Introduction to Viscoelastic Analysis	H. H. Hilton	Engineering Design for Plastics, Reinhold Publ. Corp., N.Y., 199-276 (1964).
AAE 62-2	A Method of Characteristics Analysis of Detonation Stability	R. A. Strehlow	
AAE 63-1	On Non-Stationary White Noise	Y. K. Lin	J. Acoust. Soc. Amer. 36:82-84 (1964).
AAE 63-2	Formulation and Evaluation of Approximate Analogies for Transient Temperature Dependent Linear Viscoelastic Media	H. H. Hilton and J. R. Clements	Proc. Conf. on Thermal Loading and Creep, Inst. Mech. Eng., London, 6.17-6.24(1964).
AAE 63-3	Free Vibrations of Continuous Skin-Stringer Panels with Non-Uniform Stringer Spacing and Panel Thickness	Y. K. Lin, T. J. McDaniel, B. K. Donaldson, C. F. Vail and W. J. Dwyer	AFML-TR-64-347, Wright-Patterson AFB (1965).
AAE 64-1	Random Vibrations of a Myklestad Beam	Y. K. Lin	AIAA J., 2:1448-1451 (1964).
AAE 64-2	On Detonation Initiation	R. A. Strehlow	AIAA J., 2:783-784 (1964).
AAE 64-3	A Theoretical Investigation of a Restric-tive Model for Detonation Initiation	R. B. Gilbert	AIAA J., 4:1777-1783 (1966).

RECENT AERONAUTICAL AND ASTRONAUTICAL ENGINEERING DEPARTMENT TECHNICAL REPORTS (continued)

Technical Report Number	Title	Author	Journal Publication
AAE 64-4	Transfer Matrix Representation of Flexible Airplanes in Gust Response Study	Y. K. Lin	J. of Aircraft, 2:116-121 (1965).
AAE 64-5	Dynamic Characteristics of Continuous Skin-Stringer Panels	Y. K. Lin	Acoustical Fatigue in Aerospace Structures, Syracuse Univ. Press, 163-184 (1965).
AAE 64-6	Experimental Study of the Growth of Transverse Waves in Detonations	R. Liaugminas	See AAE 66-3
AAE 64-7	Nonstationary Excitation and Response in Linear Systems Treated as Sequences of Random Pulses	Y. K. Lin	Journal of the Acoustical Society of America, 38: 453-460 (1965).
AAE 65-1	Transverse Waves in Detonations	R. A. Strehlow and F. Dan Fernandes	Combustion and Flame, 9:109-119 (1965).
AAE 65-2	A Summary of Linear Viscoelastic Stress Analysis	H. H. Hilton	Solid Rocket Structural Integrity Abstracts, 2: 1-56 (1965).
AAE 65-3	Approximate Correlation Function and Spectral Density of the Random Vibration of an Oscillator with Non-Linear Damping	Y. K. Lin	AFMK-TR-66-62, Wright Patterson AFB (1966).
AAE 65-4	Investigation of the Flow Properties Downstream of a Shock Wave Propagating into a Convergent Duct	R. E. Cusey	See AAE 65-6

RECENT AERONAUTICAL AND ASTRONAUTICAL ENGINEERING DEPARTMENT TECHNICAL REPORTS (continued)

Technical Report Number	Title	Author	Journal Publication
AAE 65-5	A Method for the Determination of the Matrix of Impulse Response Functions with Special Reference to Applications in Random Vibration Problems	Y. K. Lin	AFFDL-TR-66-80, Wright Patterson AFB, 743-751 (1966).
AAE 65-6	Convergent Channel Shock Tube for Detonation Initiation Studies	A. J. Crooker	"Detonation and Initiation Behind an Accelerating Shock Wave" by R. A. Strehlow, A. J. Crooker, R. E. Cusey, Comb and Flame, 11:339-351 (1967).
AAE 66-1	A Comparison of Experimental and Theoretical Transverse Wave Spacings in Detonation	R. H. Watson	See AAE 66-3
AAE 66-2	A Simple Model for the Mechanism of Detonation	J. R. Eyman	See AAE 66-3
AAE 66-3	Transverse Wave Structure in Detonations	R. A. Strehlow, R. Liaugminas, R. H. Watson and J. R. Eyman	11th Symposium (International) on Combustion, Mono Book Corp. Baltimore, Md., (1967).
AAE 66-4	A Real Gas Analysis Using an Acoustic Model for the Transverse Wave Spacing in Detonations	R. E. Maurer	AIAA Journal, 7: 323-328, (1969).
AAE 67-1	Shock Tube Studies in Exothermic Systems	R. A. Strehlow	Phys. Fluids, 12: 96-100, (1969).

RECENT AERONAUTICAL AND ASTRONAUTICAL ENGINEERING DEPARTMENT TECHNICAL REPORTS (continued)

Technical Report Number	Title	Author	Journal Publication
AAE 67-2	Shock Tube Chemistry	R. A. Strehlow	Progress in High Temperature Physics and Chemistry, Pergamon Press, N.Y., 2: 127-176 (1968).
AAE 67-3	Structural Failure Criteria for Solid Propellants Under Multiaxial Stresses	A. R. Zak	J. Spacecraft, 5: 265-269 (1968)
AAE 67-4	Structural Analysis of Realistic Solid Propellant Materials	A. R. Zak	J. Spacecraft, 5: 270-275 (1968).
AAE 67-5	Characteristics of Transverse Waves in Detonations of H_2, C_2H_2, C_2H_4 and CH_4 - Oxygen Mixtures	C. D. Engel	AIAA Journal, 7: 492-496 (1969).
AAE 68-1	A Review of Shock Tube Chemistry	R. A. Strehlow	Progress in High Temperature Physics and Chemistry, Pergamon Press, N.Y., 2: 1-146 (1969).
AAE 68-2	On the Interpretation of Molecular Beam Data	A. Klavins	A. Klavins and L. H. Sentman Rev. Sci. Instr., 41: 1560-1567 (1970).
AAE 68-3	Detonative Mach Stems	R. A. Strehlow H. O. Barthel	
AAE 68-4	On the Strength of Transverse Waves and Geometrical Detonation Cell Model for Gas Phase Detonations	J. R. Biller	R. A. Strehlow and J. R. Biller Comb. and Flame, 13: 577-582, (1970).
AAE 68-5	The MISTRESS User Manual	H. H. Hilton	
AAE 69-1	The Chemical Shock Tube - Implications of Flow Non-Idealities	R. A. Strehlow R. L. Belford	

RECENT AERONAUTICAL AND ASTRONAUTICAL ENGINEERING DEPARTMENT TECHNICAL REPORTS (continued)

Technical Report Number	Title	Author	Journal Publication
AAE 69-2	Phenomenological Investigation of Low Mode Marginal Planar Detonations	A. J. Crooker	Acta Astronautica, 1:303-315(1974).
AAE 69-3	Multi-Dimensional Detonation Wave Structure	R. A. Strehlow	Astronautica Acta, 15:345-358(1970).
AAE 69-4	An Experimental and Analytical Investigation of a Two-Dimensionally Stiffened Panel	A. R. Zak C. E. French	AFML-TR-68-390, Wright-Patterson AFB,(1969).
AAE 69-5	On the Kinetic Equations for a Dilute, Short Range Gas	T. J. Forster L. H. Sentman	with A.D. Grimm, Proc. Ninth International Symposium on Rarefied Gas Dynamics, A3.1-3.8 (1974).
AAE 69-6	The Sawtooth Column of the Supersonic Electric Arc in Sulfur Hexafluoride	C. E. Bond	AIAA J., 9: 510-512 (1971).
AAE 69-7	Theoretical and Experimental Analysis of Stiffened Panels Under Dynamic Conditions	A. R. Zak R. N. Yurkovich J. H. Schmidt	J. of Aircraft, 3: 149-155 (1971).
AAE 70-1	On the Interaction Between Chemical Kinetics and Gas-Dynamics in the Flow Behind a Cylindrical Detonation Front	S. Rajan	
AAE 70-2	Preliminary Studies on the Engineering Applications of Finite Difference Solutions of the Navier-Stokes Equations	W. F. Van Tassell	
AAE 70-3	Some Aspects of the Surface Boundary Condition in Kinetic Theory	A. Klavins	Proc. of International Symposium on Rarefied Gas Dynamics, Pisa, Italy (1970).

RECENT AERONAUTICAL AND ASTRONAUTICAL ENGINEERING DEPARTMENT TECHNICAL REPORTS (continued)

Technical Report Number	Title	Author	Journal Publication
AAE 70-4	A Study of the Transient Behavior of Fuel Droplets during Combustion: Theoretical Considerations for Aerodynamic Stripping	H. Krier	
AAE 70-5	On the Solid Body Model for an Accelerating Electric Arc	F. Klett	
AAE 71-1 UILU-ENG 71 0501	Detonative Mach Stems	R. A. Strehlow H. O. Barthel	
AAE 71-2 UILU-ENG 71 0502	An Investigation of Transient Phenomena in Detonations	R. J. Stiles	with R. A. Strehlow, A. A. Adamczyk, Astronautica Acta, 17: 509-527 (1972)
AAE 71-3 UILU-ENG 71 0503	On the Role of Tangential Velocity Changes in the Scattering of a Molecular Beam from A Solid Surface	C. C. Chrisman L. H. Sentman	Chemical Physics Letters, 26:407-413(19
AAE 72-1 UILU-ENG 72 0501	Unconfined Vapor Cloud Explosions - An Overview	R. A. Strehlow	Fourteenth Symposium on Combustion, 1189-1200 (1973).
AAE 72-2 UILU-ENG 72 0502	Application of Illiac IV Computer to Numerical Solutions of Structural Problems	H. H. Hilton A. R. Zak J. J. Kessler P. C. Rockenbach	
AAE 72-3 UILU-ENG 72 0503	On the Measurement of Energy Release Rates In Vapor Cloud Explosions	R. A. Strehlow L. D. Savage G. M. Vance	Combustion Science and Technology, 6: 307-312 (1972).

RECENT AERONAUTICAL AND ASTRONAUTICAL ENGINEERING DEPARTMENT TECHNICAL REPORTS (continued)

Technical Report Number	Title	Author	Journal Publication
AAE 72-4 UILU-ENG 72 0504	A Performance Comparison of Several Numerical Minimization Algorithms	J. E. Prussing	
AAE 73-1 UILU-ENG 73 0501	Stresses and Damping in the Matrix of a Composite Material	A. R. Zak	
AAE 73-2 UILU-ENG 73 0502	Early Burning Anomalies in the XM 645 Flechette Cartridge	H. Krier D. R. Hall	BRL Rept. No. 104 (1973).
AAE 73-3 UILU-ENG 73 0503	Equivalent Explosive Yield of the Explosion in the Alton Southern Gateway Yard, East St. Louis, Ill., January 22, 1972	R. A. Strehlow	
AAE 73-4 UILU-ENG 73 0504	Failure Studies of Gaseous Detonations	R. J. Salm	Acta Astronautica (in press).
AAE 73-5 UILU-ENG 73 0505	An Investigation of Hydrogen-Oxygen-Argon Detonations	J. R. Biller	
AAE 73-6 UILU-ENG 73 0506	Interior Ballistic Predictions Using Data From Closed and Variable-Volume Simulators	H. Krier S. A. Shimpi M. J. Adams	Proc. 11th JANNAF Combustion Meeting, CPIA Publ. 261:17-30(1974).
AAE 73-7 UILU-ENG 73 0507	Theory of Rotationally Symmetric Laminar Premixed Flames	G. M. Vance H. Krier	Comb. and Flame J., 22: 365-375 (1974).
AAE 73-8 UILU-ENG 73 0508	Burning of Fuel Droplets at Elevated Pressures	J. H. Rush H. Krier	Comb. and Flame J., 22: 377-382 (1974).
AAE 73-9 UILU-ENG 73 0509	An Impact Ignition Model for Solid Propellants	H. Krier H. H. Hilton O. Olorunsola D. L. Reuss	BRL Rept. No. 1707 (1974).

RECENT AERONAUTICAL AND ASTRONAUTICAL ENGINEERING DEPARTMENT TECHNICAL REPORTS (continued)

Technical Report Number	Title	Author	Journal Publication
AAE 73-10 UILU-ENG 73 0510	Optimal Multiple-Impulse Direct Ascent Fixed-Time Rendezvous	J. E. Prussing L. R. Gross	AIAA J., 12, 885-889 (1974).
AAE 73-11 UILU-ENG 73 0511	The Structure and Stability of Detonation Waves	R. A. Strehlow	
AAE 74-1 UILU-ENG 74 0501	Model of Flame Spreading and Combustion Through Packed Beds of Propellant Grains	H. Krier W. F. Van Tassell S. Rajan J. T. Ver Shaw	BRL Report No. 147 (1974). Int. J. Heat-Mass Transfer, 1377-86 (1975).
AAE 74-2 UILU-ENG 74 0502	On the Nature of Non-Ideal Blast Waves	R. A. Strehlow A. A. Adamczyk	WSS/CI Paper No. 74-12, Pullman, Wash. (1974).
AAE 74-3 UILU-ENG 74 0503	Viscous Incompressible Flow in Spiral Channels	W. F. VanTassell	
AAE 74-4 UILU-ENG 74 0504	Frequency Response Functions of a Disordered Periodic Beam	J. N. Yang Y. K. Lin	J. Sound and Vibration 38: 317-340 (1975).
AAE 74-5 UILU-ENG 74 0505	Predicting Uniform Gun Interior Ballistics: Part I. An Analysis of Closed Bomb Testing	H. Krier S. A. Shimpi	Comb. and Flame J. 25: 229-240 (1975).
AAE 74-6 UILU-ENG 74 0506	Predicting Uniform Gun Interior Ballistics: Part II. The Interior Ballistic Code	H. Krier M. J. Adams	Proc. 11th JANNAF Comb. Meeting, CPIA Publ. 261: 17-30 (1974).
AAE 74-7 UILU-ENG 74 0507	Predicting Uniform Gun Interior Ballistics: Part III. The Concept and Design of the Dynagun Ballistic Simulator	H. Krier J. W. Black	Proc. 11th JANNAF Comb. Meeting, CPIA Publ. 261: 31-43(1974).
AAE 74-8 UILU-ENG 74 0508	Process of Fluidization During Porous Solid Propellant Combustion	H. Krier J. T. Ver Shaw	AIAA Paper 75-242 (1975).
AAE 74-9 UILU-ENG 74 0509	An Analysis of Flame Propagation Through Coal Dust-Air Mixtures	J. L. Krazinski H. Krier	AIAA Paper 74-1111 (1974).

RECENT AERONAUTICAL AND ASTRONAUTICAL ENGINEERING DEPARTMENT TECHNICAL REPORTS (continued)

Technical Report Number	Title	Author	Journal Publication
AAE 74-10 UILU-ENG 74 0510	An Interior Ballistics Prediction of the M549 Rocket Assisted Projectile	H. Krier S. Shimpi E. Meister	
AAE 75-1 UILU-ENG 75 0501	Dynamically Induced Thermal Stresses in Composite Material, Structural Panels	A. Zak W. Drysdale	
AAE 75-2 UILU-ENG 75 0502	Numerical Analysis of Laminated, Orthotropic Composite Structures	A. R. Zak	
AAE 75-3 UILU-ENG 75 0503	The Characterization and Evaluation of Accidental Explosions	R. A. Strehlow W. E. Baker	NASA CR 134779 (June 1975). Also Progr. Energy & Comb. Sc. (in press).
AAE 75-4 UILU-ENG 75 0504	Program Manual for the Eppler Airfoil Inversion Program	W. G. Thomson	
AAE 75-5 UILU-ENG 75 0505	Design of High Lift Airfoils with a Stratford Distribution by the Eppler Method	W. G. Thomson	
AAE 75-6 UILU-ENG 75 0506	Prediction of Flame Spreading and Pressure Wave Propagation in Propellant Beds	H. Krier	AIAA J. 14: 301-309 (1976)
AAE 75-7 UILU-ENG 75 0507	Vigorous Ignition of Granulated Beds by Blast Impact	H. Krier S. Gokhale	Int. J. Heat-Mass Transfer 19: 915-923 (1976)
AAE 75-8 UILU-ENG 75 0508	Solid Propellant Burning Evaluation with the Dynagun Ballistic Simulator	H. Krier T. G. Nietzke M. J. Adams J. W. Black E. E. Meister	J. Ballistics 1: 103-149 (1976)
AAE 75-9 UILU-ENG 75 0509	Structural Reliability & Minimum Weight Analysis for Combined Random Loads & Strengths	H. H. Hilton	AIAA J. (in press)

RECENT AERONAUTICAL AND ASTRONAUTICAL ENGINEERING DEPARTMENT TECHNICAL REPORTS (Continued)

Technical Report Number	Title	Author	Journal Publication
AAE 75-10 UILU-ENG 75 0510	Linear Viscoelastic Analysis with Random Material Properties	H. H. Hilton J. Hsu J. S. Kirby	
AAE 76-1 UILU-ENG 76 0501	Two Degree of Freedom Flutter of Linear Viscoelastic Wings in Two Dimensional Flow	C. F. Vail H. H. Hilton	In press AIAA J.
AAE 76-2 UILU-ENG 76 0502	An Error Analysis of Computerized Aircraft Synthesis	V. V. Volodin H. H. Hilton	In press J. of Aircraft
AAE 76-3 UILU-ENG 76 0503	Reactive Two-Phase Flow Models Applied to the Prediction of Detonation Transition in Granulated Propellant	H. Krier M. Dimitstein S. S. Gokhale	AIAA J. 16: 177-183 (1978)
AAE 76-4 UILU-ENG 76 0504	Transient Temperature Response of Charring Composite Slabs	J. E. Prussing H. Krier	Int'l J. Heat Mass Transfer. 21: 519-522 (1978)
AAE 76-5 UILU-ENG 76 0505	Nonlinear Response of Laminated Composite Material Cylindrical Shells	A. R. Zak J. N. Craddock	
AAE 76-6 UILU-ENG 76 0506	An Investigation of Blast Waves Generated from Non-Ideal Energy Sources	A. A. Adamczyk	
AAE 77-1 UILU-ENG 77 0501	Nonlinear Dynamic Analysis of Flat Laminated Plates by the Finite Element Method	A. R. Zak	
AAE 77-2 UILU-ENG 77 0502	An Investigation of Blast Waves Generated by Constant Velocity Flames	R. T. Luckritz	
AAE 77-3 UILU-ENG 77 0503	On the Blast Waves Produced by Constant Velocity Combustion Waves	R. A. Strehlow R. D. Luckritz	
AAE 77-4 UILU-ENG 77 0504	Direct Initiation of Detonation by Non-Ideal Blast Waves	R. J. Cesarone	
AAE 77-5 UILU-ENG 77 0505	The Blast Wave Generated by Constant Velocity Flames	S. A. Shimpi R. A. Strehlow	

RECENT AERONAUTICAL AND ASTRONAUTICAL ENGINEERING DEPARTMENT TECHNICAL REPORTS (Continued)

Technical Report Number	Title	Author	Journal Publication
AAE 77-6 UILU-ENG 77 0506	Exploratory Studies of Flame and Explosion Quenching	R. A. Strehlow L. C. Sorenson L. D. Savage H. Krier	
AAE 77-7 UILU-ENG 77 0507	The Trajectory of a Liquid Droplet Injected Into the Wake of an Aircraft in Ground Effect	M. B. Bragg	
AAE 77-8 UILU-ENG 77 0508	Comparison of Viscoelastic and Structural Damping in Flutter	H. H. Hilton	
AAE 77-9 UILU-ENG 77 0509	The Blast Wave Generated by Constant Velocity Flames	R. A. Strehlow R. T. Luckritz A. A. Adamczyk S. Shimpi	
AAE 77-10 UILU-ENG 77 0510	Wind Energy: History, Economics, and the Vertical Wind Turbine	T. R. Richards	
AAE 77-11 UILU-ENG 77 0511	Final Report: Low Speed Airfoil Study	A. I. Ormsbee	
AAE 77-12 UILU-ENG 77 0512	Final Report: Propeller Study, Part I, Introduction and Overview	A. I. Ormsbee	
AAE 77-13 UILU-ENG 77 0513	Final Report: Propeller Study, Part II, The Design of Propellers for Minimum Noise	C. J. Woan	
AAE 77-14 UILU-ENG 77 0514	Final Report: Propeller Study, Part III, Experimental Determination of Thrust & Torque on the YO-3A Aircraft	S. A. Siddiqi K. R. Sivier A. I. Ormsbee	
AAE 77-15 UILU-ENG 77 0515	Direct Initiation of Detonation	R. A. Strehlow H. O. Barthel	

RECENT AERONAUTICAL AND ASTRONAUTICAL ENGINEERING DEPARTMENT TECHNICAL REPORTS (Continued)

Technical Report Number	Title	Author	Journal Publication
AAE 77-16 UILU-ENG 77 0516	The Effects of Energy Distribution Rates and Density Distribution on Blast Wave Structure	R. A. Strehlow L. H. Sentman	
AAE 77-17 UILU ENG 77 0517	Modeling of Convective Mode Combustion Through Granulated Propellant to Predict Transition to Detonation	H. Krier J. A. Kezerle	17th Combustion Symposium: In Pres:
AAE 78-1 UILU ENG 78 0501	Unsteady Internal Boundary Layer Flows with Application to Gun Barrel Heat Transfer and Erosion	M. J. Adams H. Krier	
AAE 78-2 UILU ENG 78 0502	Extracting Burning Rates for Multiperforated Propellant from Closed Bomb Testing	H. Krier	
AAE 78-3 UILU ENG 78 0503	Lean Limit Flammability Study of Methane-Air Mixtures in a Square Flammability Tube	J. Jarosinski R. A. Strehlow	
AAE 78-4 UILU ENG 78 0504	Interim Technical Report AFOSR 77-3336: "An Investigation of the Ignition Delay Times For Propylene Oxide-Oxygen-Nitrogen Mixtures"	E. E. Meister	
AAE 78-5 UILU ENG 78 0505	Final Report: A Distribution Model for the Aerial Application of Granular Agricultural Particles	S. T. Fernandes A. I. Ormsbee	
AAE 78-6 UILU ENG 78 0506	The Thermal Structure of a Methane-Air Flame Propagating in a Square Flammability Tube	J. Jarosinski R. A. Strehlow	
AAE 78-7 UILU ENG 78 0507	The Effects of Energy Distribution Rates and Density Distribution on Blast Wave Structure	R. A. Strehlow L. H. Sentman	
AAE 78-8 UILU ENG 78 0508	The Effect of a Zero G Environment on Flammability Limits as Determined Using a Standard Flammability Tube Apparatus	R. A. Strehlow D. L. Reuss	

RECENT AERONAUTICAL AND ASTRONAUTICAL ENGINEERING DEPARTMENT TECHNICAL REPORTS (Continued)

Technical Report Number	Title	Author	Journal Publication
AAE 79-1 UILU-ENG 79 0501	An Approximate Finite Element Method of Stress Analysis of Non-Axisymmetric Bodies with Elastic-Plastic Material	J. N. Craddock A. R. Zak	
AAE 79-2 UILU-ENG 79 0502	Stability of Bridge Motion in Turbulent Winds	Y. K. Lin S. T. Ariaratnam	
AAE 79-3 UILU ENG 79 0503	Rotor Blade Dynamics in Hovering Flights	C.Y.R. Hong	
AAE 79-4 UILU ENG 79 0504	Finite Element Analysis of A Dynamically Loaded Flat Laminated Plate	D. W. Pillasch A. R. Zak	
AAE 79-5 UILU ENG 79 0505	An Efficient Rotational Nonequilibrium Model of a CW Chemical Laser	L. H. Sentman	
AAE 79-6 UILU ENG 79 0506	Column Response to Vertical-Horizontal Earthquakes	Y. K. Lin T. Y. Shih	